

ABSTRACT

Title of Dissertation: TUNING THE IONIC AND ELECTRONIC PROPERTIES OF METAL PHOSPHATES BY ATOMIC LAYER DEPOSITION

Daniela Rosa Fontecha Solano, Doctor of Philosophy, 2025

Dissertation Directed By: Professor Gary W. Rubloff, Department of Materials Science and Engineering

Atomic layer deposition (ALD) can be used in nano-scaling of solid-state batteries (SSBs) for microelectronics applications due to its compositional tunability and atomic scale control of thin films enabled by the sequential nature of this technique. The Li-ion conductivity of the electrolyte is a key factor in the performance of Li-ion battery systems. In bulk Li-ion SSBs, solid state electrolytes have been developed with ionic conductivities approaching that of liquid electrolytes (10^{-2} S/cm) by utilizing fast-ion conducting crystalline phases. However, ALD Li-ion conductors have been limited to the range of 10^{-7} - 10^{-6} S/cm with the primary strategy being to develop amorphous Li-ion conductors (e.g., amorphous phosphates and silicates doped by glass formers). This work utilizes ALD processing techniques to develop previously unexplored chemistries and crystalline structures in metal phosphate-based Li-ion conductors inspired by the fast-ion conducting NASICON phase Li-Al-Ti-P-O family of materials – a complex system that

can contain 5+ elements. This work leans on the layer-by-layer quality of ALD to tune the composition of the system by alternating between layers of Li_2O , TiO_2 , Al_2O_3 and PO_x in different sequences to control the composition of the mixed metal phosphates with varying degrees of compositional and structural complexity.

The amorphous route to fast-ion conduction is explored by development of ALD processes for the solid-state electrolytes: Al-doped Li_3PO_4 (LAP), lithium titanium phosphate (LTP), and Al-doped LTP (LATP). In LAP (5.3×10^{-7} S/cm) and LATP (1.8×10^{-6} S/cm) the Al-doping strategy was found to have an effect of increasing ionic conductivity by acting as a glass former in small doping amounts. In the LAP system, higher concentrations of Al % lead to glass-modifying behavior with large Al_2O_3 domains that interrupt the LAP network and are detrimental to Li-ion conduction. Additionally, this doping strategy is limited in its ability to improve the conductivity in already well-connected amorphous material like LTP (1.5×10^{-6} S/cm), meaning that it is most effective in systems like Li_3PO_4 that lack strong cross-linking agents.

Thermal annealing was used to study the effects on composition and initial phosphate domain separation on the crystallization route towards the NASICON crystalline structure. In the thermal LTP process, an electron conducting impurity (TiO_2) was discovered that provided an external electron conduction path necessary for lithiation of the NASICON structure and enabled the study of the NASICON thin film as an electrode material as well. A semicrystalline nanocomposite of NASICON LTP and TiO_2 anatase was found to have an ionic conductivity of 9.3×10^{-7} S/cm and electronic conductivity of 2.3×10^{-7} S/cm. This nanocomposite electrode demonstrated to have a reversible capacity of 328 mAh/g at 1 C and 71 % retention at 20 C owed to a) the fast kinetics of the NASICON phase, and b) the intimate interfacial contact provided by the amorphous LTP matrix between crystalline grains. The fast kinetics of this system offer routes

for further exploration of this material with applications beyond batteries in microelectronics (i.e., supercapacitors).

The TiO₂ impurity was removed from the LTP process by forming trimethyl phosphate (TMP) radicals with an argon plasma step to allow the TMP to fully saturate the surface and disallow excess TiO₂ formation. This led to a phosphate network with higher degree of crosslinking and no electronic conduction – thus making it a suitable amorphous electrolyte material. However, thermal annealing studies showed that the changes to the phosphate network altered the crystallization pathway – forming γ -Li₃PO₄ and TiP₂O₇ rather than NASICON LTP. Understanding the nature of these changes to the phosphate network requires additional characterization techniques of these amorphous phosphates that probe the local bonding environment and molecular structure with respect to the changed process conditions.

This work explores a new ALD mixed metal phosphate chemistry and how composition-property and structure-property relationships are affected at different scales depending on ALD process conditions and post-processing. A highlight of this work is the demonstration of the control of the TiO₂ impurity in the ALD process that allows control over the LATP materials properties as either an electrode or electrolyte – providing an opportunity to study this system as a single material battery or supercapacitor. This dissertation marks the beginning of an exploration of a much larger system of Li_{1-x}M_xM'_{2-x}(PO₄)₃ where introduction of dopants (M = Al⁺³, Cr⁺³, Ga⁺³, Sc⁺³, Y⁺³, In⁺³, etc.) or alternate metal phosphates (M' = Ti⁺⁴, Ge⁺⁴, Sn⁺⁴, Hf⁺⁴, or Zr⁺⁴, etc.) can be modified in the layer-by-layer approach to alter the materials and electrochemical properties of both thin film electrodes and electrolytes within these chemistries.

TUNING THE IONIC AND ELECTRONIC PROPERTIES OF METAL
PHOSPHATES BY ATOMIC LAYER DEPOSITION

by

Daniela Rosa Fontecha Solano

Dissertation submitted to the Faculty of the Graduate School of the
University of Maryland, College Park, in partial fulfillment
of the requirements for the degree of
Doctor of Philosophy
2025

Advisory Committee:

Professor Gary Rubloff, Chair
Dr. Keith Gregorczyk, Co-Chair
Professor Sang Bok Lee
Professor Paul Albertus
Professor Carlos Rios Ocampo
Professor Alexander Kozen

© Copyright by
Daniela Rosa Fontecha Solano
2025

Dedication

To my mother and my brother

Acknowledgements

I would like to sincerely thank Prof. Gary Rubloff for taking me into this very welcoming and collaborative research group. His insightful questions always hit the right spot to allow me to reflect, both on professional and scientific matters, which has allowed me to grow as a scientist and person.

I would like to thank my mentors in the Rubloff group for showing me how to be a good leader by the many examples throughout the years. Thanks to Dr. Keith Gregorczyk for co-advising me in the latter half of my PhD, for helping me improve my writing, and for introducing me to some of the different aspects of a career in science. Thanks to Dr. Alex Kozen for his advising early in my PhD and for his continuous encouragement even after leaving the group. Thanks to Dr. Davy Stewart for being a great example of a patient and effective mentor and educator.

Thanks to Dr. Blake Nuwayhid, Dr. Victoria Ferrari, and Dr. Kunal Ahuja for training me, answering my questions, and creating a great collaborative environment in the student office as senior students when I joined the group.

Thanks to the current students in the Rubloff and Lee group who I share an office with (John Hoerauf, Leo Tapia-Aracayo, Steven Douglas, Osma Gomez, and Stefan Theodoru) for being great lab mates and fun to work with.

A special thanks to Osma Gomez for figuring out how to safely synthesize LiOtBu and giving us a reliable supply of lithium precursor. Considering all of my work relies on this precursor, my life would have been made a lot harder without her expertise as a chemist.

Thanks to Dr. Nam Kim for helping me with all of my FabLab needs and for his insights on electrochemistry.

Thanks to the Rubloff group members and the Lee group (Prof. Sangbok Lee, Dr. Yang Wang, Dr. Nam Kim, Steven Douglas, Osma Gomez) for feedback on my presentations and research throughout the years.

Thank you to my collaborators: Alex Hall and Prof. John Cumings for their expertise in TEM and for being excellent to work with and learn from.

Thanks to the IREAP and AVW staff: Nolan Ballew, Dr. Don Schmadel, and Dr. Bryan Quinn, for their help on various occasions when I've asked for advice or assistance in resolving equipment issues and machining things for my projects.

Many thanks to my mom for finding ways to support my passions and instilling in me the confidence to pursue them. A big thanks to my brother for inspiring me to become a scientist since before I knew what that really meant.

I am thankful for my funding sources for support throughout my PhD. This work was supported by Murata Integrated Passive Solutions, the U.S. Department of Energy, and the U.S.-Israel Energy Center Program, which is managed by the U.S.-Israel Binational Industrial Research and Development (BIRD) Foundation. Under the Office of Science, Office of Basic Energy Sciences, Grant DE-SC0021070, DOE supported the synthesis of Li-containing titanium phosphates with composition varied through a dopant-supercycle process. Murata supported the evaluation and testing of ALD solid electrolyte materials for application in 3D solid state capacitor structures. I was supported in large part by the National Science Foundation Graduate Research Fellowship Program under Grant No. DGE 1840340. Any opinions, findings, and conclusions or recommendations expressed in this material are those of the author(s) and do not necessarily reflect the views of the National Science Foundation.

Table of Contents

| | |
|----------------------------------------------------------------------------------------|------|
| Dedication..... | ii |
| Acknowledgements..... | iii |
| Table of Contents..... | vi |
| List of Tables..... | viii |
| List of Figures..... | ix |
| List of Schemes..... | xi |
| List of Abbreviations..... | xii |
| Chapter 1: Introduction..... | 1 |
| 1.1. Motivation..... | 1 |
| 1.2. Dissertation Overview..... | 3 |
| 1.3. Review of Metal Phosphate Glass Networks..... | 3 |
| 1.4. Review of NASICON Bulk Materials System..... | 7 |
| 1.4.1. NASICON Solid State Electrolytes..... | 7 |
| 1.4.2. NASICON Electrodes..... | 8 |
| 1.5. Atomic Layer Deposition as a Tool for Ion-Conducting Thin Films..... | 9 |
| 1.5.1. Review of Metal Phosphate ALD Processes..... | 11 |
| 1.5.2. Further Development of Metal Phosphate ALD Processes is Necessary..... | 18 |
| Chapter 2: Experimental Methods..... | 20 |
| 2.1. Atomic Layer Deposition Process Development..... | 20 |
| 2.1.1. ALD Parameters/Conditions..... | 20 |
| 2.1.2. Spectroscopic Ellipsometry..... | 22 |
| 2.1.3. X-Ray Photoelectron Spectroscopy (XPS)..... | 23 |
| 2.2. Structural Characterization..... | 23 |
| 2.2.1. Annealing Procedures..... | 23 |
| 2.2.2. Raman Spectroscopy..... | 24 |
| 2.2.3. X-Ray Diffraction..... | 24 |
| 2.2.4. Microscopy..... | 24 |
| 2.3. Impedance and Electrochemical Measurements..... | 25 |
| 2.3.1. Electrochemical Impedance Spectroscopy & DC Relaxation..... | 25 |
| 2.3.2. Electrochemical Measurements..... | 25 |
| Chapter 3: Effect of Metal Phosphate ALD Network on Thin Film Electrical Properties... | 26 |
| 3.1. Chapter Summary..... | 26 |
| 3.2. Al ³⁺ as a Glass Former in the Lithium Phosphate System..... | 27 |
| 3.2.1. ALD Process Development of Al-doped Lithium Phosphate..... | 27 |
| 3.2.2. Ion Conduction in Al-doped Lithium Phosphate..... | 31 |
| 3.2.3. Discussion on Aluminum as a Dopant and Modifier in Lithium Phosphate Network 35 | |
| 3.3. Glass-formers: Li and Al in the Ti-P-O System ALD Processes..... | 36 |
| 3.3.1. Tunable TiO ₂ Content in Titanium Phosphate ALD Process..... | 36 |
| 3.3.2. Lithium Titanium Phosphate (LTP) ALD Process Development..... | 38 |
| 3.3.3. Lithium Aluminum Titanium Phosphate (LATP) ALD Process..... | 44 |
| 3.4. Effects of Network-Type and Local Structure on Thin Film Properties..... | 46 |
| 3.5. Conclusions and Future Work – Glassy ALD Metal Phosphates..... | 50 |

| | |
|---------------------------------------------------------------------------------------------------------|----|
| Chapter 4: Phase Engineering Strategies and Challenges of the Li-Ti-P-O Thin Film Materials System..... | 52 |
| 4.1. Chapter Summary | 52 |
| 4.2. Phase Engineering Towards an LTP/TiO ₂ Nanocomposite Electrode Material | 52 |
| 4.3. Challenges and Future Considerations with Phase Engineering Towards a NASICON ALD Electrolyte..... | 64 |
| 4.3.1. Crystallization Behavior of Plasma Enhanced LTP Electrolyte | 65 |
| 4.3.2. Considerations and Future Work for Crystalline NASICON and ALD Thin Film Electrolytes | 67 |
| Chapter 5: Electrochemical Behavior of LTP/TiO ₂ Nanocomposite Electrode | 69 |
| 5.1. Chapter Summary | 69 |
| 5.2. Deconvolutions of Electrical Behavior in LTP Semicrystalline Nanocomposite Thin Film | 69 |
| 5.3. LTP Nanocomposite as a High-Rate Electrode Material..... | 73 |
| Chapter 6: Conclusions and Future Work..... | 81 |
| 6.1. The Amorphous Route to Fast-Ion Conductors | 81 |
| 6.2. The Crystalline Route to Fast Ion-Conductors | 81 |
| 6.3. Solid State Devices for Advanced Iontronics Applications..... | 82 |
| 6.4. Publication and Communication Outcomes During Doctoral Degree..... | 83 |
| 6.4.1. Publications..... | 83 |
| 6.4.2. Conference Proceedings..... | 84 |
| Bibliography | 85 |

List of Tables

Table 1.1: A list of common precursors for incorporation of elements relevant to the Li-Al-Ti-P-O materials system.

Table 1.2: A list of key ALD-developed metal phosphates.

Table 1.3: A list of titanium phosphate ALD processes.

Table 2.1: Experimental parameters of ALD precursors used in this dissertation.

Table 2.2: Process sequences to achieve the relevant process chemistries discussed in this dissertation.

Table 3.1: Ionic conductivity values of lithium phosphate and lithium aluminum phosphate ALD films.

Table 3.2: Compositional breakdown of thermal LATP films of different supercycling ratios.

Table 4.1: Raman peak assignments of the annealed thermal LTP (n = 7, 2, 1) films

List of Figures

Figure 1.1: An illustration of phosphate coordination and 2D metal phosphate glass chemical structure.

Figure 1.2: Explanation of a generic metal oxide ALD process and an example of supercycling to make metal phosphates with ALD.

Figure 3.1: Reaction sequence of ALD process for LAP and the growth per cycle temperature dependence.

Figure 3.2: XPS of LAP ALD films.

Figure 3.3: XRD of lithium phosphate and LAP ALD films.

Figure 3.4: EIS of lithium phosphate and LAP ALD films.

Figure 3.5: O 1s XPS high resolution spectra of thermal and PEALD titanium phosphate thin films.

Figure 3.6: XPS of LTP thin films.

Figure 3.7: Compositional breakdown of thermal LTP thin films.

Figure 3.8: XPS of thermal LTP, PEALD LTP, and thermal LATP.

Figure 3.9: EIS of thermal LTP.

Figure 3.10: EIS of PEALD LTP.

Figure 3.11: EIS of thermal LATP.

Figure 4.1: Raman and XRD of annealed at 850 °C quenched and radiatively cooled.

Figure 4.2: Rietveld refinement of thermal LTP ($n = 2$) annealed at 850 °C for 3 hours.

Figure 4.3: Raman and XPS map of annealed thermal LTP films in different compositions.

Figure 4.4: Raman spectra of thermal LTP films annealed showing effects of composition on thermal budget.

Figure 4.5: Raman and XRD of thermal LTP ($n = 2$) annealed at 650 °C for 8.5 minutes.

Figure 4.6: SEM images of thermal LTP annealed at 850 °C and 650 °C

Figure 4.7: Scherrer analysis of annealed thermal LTP.

Figure 4.8: TEM images and schematic of thermal LTP nanocomposite.

Figure 4.9: Raman of annealed PEALD LTP.

Figure 5.1: EIS of annealed thermal LTP.

Figure 5.2: DC relaxation of annealed thermal LTP.

Figure 5.3: Arrhenius plots of the different ionic and electronic components in the annealed thermal LTP nanocomposite.

Figure 5.4: Cyclic voltammetry of annealed thermal LTP from 1.6 - 3.5 V.

Figure 5.5: Cyclic voltammetry of annealed thermal LTP from 0.5 - 3.5 V and Raman before and after cycling.

Figure 5.6: Gravimetric voltammetry of annealed thermal LTP from 1.6 - 3.5 V.

Figure 5.7: Rate tests and gravimetric voltammetry of annealed thermal LTP in different voltage windows.

List of Schemes

Scheme 3.1: Simplified reaction schematics of thermal and plasma-enhanced ALD for titanium phosphate processes.

Scheme 3.2: ALD reaction sequence for thermal LTP with supercycling illustration.

Scheme 3.3: ALD reaction sequence for PEALD LTP thin film.

Scheme 3.4: ALD reaction sequence for thermal LATP thin film.

List of Abbreviations

ALD – atomic layer deposition

LIB – lithium-ion battery

IoT – internet of things

BOs – bridging oxygens

NBOs – non-bridging oxygens

LTP – lithium titanium phosphate

LATP – lithium aluminum titanium phosphate

LFTP – lithium iron titanium phosphate

TMP – trimethyl phosphate

TEP - triethyl phosphate

TTMSP - tris(trimethylsilyl) phosphate

DEPA - diethyl phosphoroamidate

TDMAP - tris(dimethylamino)phosphate

LiOtBu – lithium tert-butoxide

LiHDMS - lithium bis(trimethylsilyl)amide

TiCl₄ – titanium (IV) chloride

TTIP - titanium (IV) isopropoxide

TDMAT - tetrakis(dimethylamido)titanium(IV)

TMA – trimethyl aluminum

LAP - Al-doped lithium phosphate

LiPON – lithium phosphorous oxynitride

N_t – triply coordinated nitrogen

N_d – doubly coordinated nitrogen

PEALD – plasma-enhanced atomic layer deposition

UHV – ultra high vacuum

TiPO – titanium phosphate

SEM – scanning electron microscopy

XPS – X-ray photoelectron microscopy

XRD – X-ray diffraction

RTA – rapid thermal annealer

FIB - focused ion beam

TEM – transmission electron microscopy

EIS – electrochemical impedance spectroscopy

PID - proportional integral derivative

GPC – growth per cycle

CPE - constant phase element

MIM – metal-insulator-metal

Chapter 1: Introduction

1.1. Motivation

Atomic layer deposition (ALD), first developed in the 70's for electroluminescent displays¹, has been an enabler of many industries (e.g., microelectronics,¹ commercial lithium-ion batteries,² fuel cells,³ photovoltaics,⁴ etc.) due to its angstrom-scale precision and conformality in thin film deposition. The development of conformal processes for dielectrics and metals has advanced key technologies in the semiconductor industry through advanced patterning of transistors and interconnects⁵ that pushed the limits of Moore's Law in the early 2000's.⁶ In the 90's, ALD of ion-conducting materials made headway in the commercialization of lithium-ion battery (LIB) chemistries with the invention of powder-coating ALD processes.^{7,8} This enabled high-performing commercial LIBs in which ion-conducting thin films (10's of nm) act as protection layers of cathodes and anodes to improve cycle stability by preventing parasitic reactions between high energy density electrodes and liquid electrolytes.⁹

There is an interesting opportunity in utilizing ion-conducting ALD films to develop materials and nano-scale devices that couple ionic and electronic behavior (coined as 'iontronics') to complement and advance features in microelectronics.¹⁰ ALD is uniquely positioned to utilize 3D-structured scaffolds for solid-state ionic devices compatible with CMOS-processing due to its ability to deposit highly conformal films with a diverse selection of materials. For ion storage and transport in iontronics, as feature sizes in planar devices become smaller with thinner films, energy density is lost due to loss of active material (and resulting loss in ion storage capacity). The approach to maintain energy density in this case is to create a high aspect ratio scaffold to increase the surface area and therefore the total amount of material in the same footprint area.^{11,12} Beyond

energy storage, iontronics extend to edge computing regimes accessible with ion-tunable transistors (in which memory and compute are co-located) among other internet of things (IoT) applications.¹³⁻¹⁵ Development of fast ion-conducting ALD films with tunable electronic conductivity is essential to pushing the boundaries of energy, power, and information density in microelectronics.¹⁶⁻¹⁸

In state-of-the-art ALD electrolytes the ionic conductivity is limited to the order of 10^{-7} to 10^{-6} S/cm, whereas other synthesis methods have achieved conductivities five orders of magnitude higher at 10^{-2} S/cm by leveraging different chemistries and crystalline phases. The ionic conductivity of thin films fabricated by ALD has been limited by materials development and crystallinity control challenges, as suitable materials must be fabricated with both the appropriate composition, crystal structure, and microstructure to meet kinetic demands of these applications. Although amorphous ALD metal phosphates have been well studied, there is a gap in the materials exploration space with regards to fast-ion-conducting crystalline and semicrystalline metal phosphates.

In the bulk, crystalline phosphate-based solid-state electrolytes (SSEs) like NASICON-type LATP in the bulk are air-stable and have conductivities ranging from 10^{-5} to 10^{-3} S/cm. LATP is composed of elements easily accessible by existing ALD processes, making it an ideal candidate to develop as an ALD thin film. This work aims to explore an entirely new branch of ALD ternary and quaternary metal phosphates within the Li-Al-Ti-P-O materials system. Such a large parameter space allows (and introduces its own challenges) for the selection of different processing conditions and for tuning of key properties such as ionic or electronic conductivities within a single materials system to push the boundary of on-chip applications.

1.2. Dissertation Overview

The purpose of this work is to use a deposition technique like ALD, which offers chemical control at the nanometer scale, to develop and understand the properties of the Li-Al-Ti-P-O glass-ceramic thin film materials system. There are many degrees of freedom, not only in the manipulation of stoichiometry of this 4-5 component system, but also in the phase purity control required to achieve the NASICON structure. These topics will be discussed in three phases:

- 1) the exploration of ALD metal phosphate glasses and the effects of a changing phosphate network based on processing parameters and glass-formers in the system (Chapter 3),
- 2) a study on how phase purity control of the NASICON system can be achieved by controlling both composition and annealing conditions (Chapter 4), and
- 3) understanding the electrical and electrochemical properties of select films within this materials system (Chapter 5).

1.3. Review of Metal Phosphate Glass Networks

The scope of this work is to understand the role that both composition and structure play in the ionic and electronic properties of the complex mixed metal phosphate Li-Ti-Al-P-O system, which can be studied as a glass or glass-ceramic. Even when only considering the glass system (amorphous state), a change in composition can influence the overall structure of the glass phosphate network. This section details how phosphate glasses are generally structured, how their structures can be modified with inclusion of metal oxides, and how these changes affect the ionic and electronic properties of a metal phosphate glass.

The basic unit of phosphate glass is P_2O_5 , composed of corner-sharing PO_4 tetrahedra with up to three bridging oxygens (BOs) per tetrahedron as shown in **Figure 1.1a**. Phosphate glass

networks can form rings, chains and sheets depending on the degree of connectivity with BOs. Metal oxides are often used as glass network modifiers. They enter the phosphate glass as cations, occupying interstitial sites, by breaking up BOs and contributing oxygens into the non-bridging oxygens (NBOs) structure.¹⁹ Depending on the cation valency and amount of cation in the structure, the phosphate tetrahedra will have between 0-3 BOs (**Figure 1.1a**). Alkali metal oxides contribute one NBO to the local structure such that charge balance is maintained. Transition metal oxides can have higher valencies, which requires more oxygens (some BOs and some NBOs) to maintain charge balance. **Figure 1.1b-c** shows a planar representation of a metal phosphate network to demonstrate how alkali cations and transition metal cations alter the local structure, best described by the number of BOs and NBOs in the material. These glass systems have a large free space due to the open network structure facilitated by corner sharing between MO_6 and PO_4 polyhedra that allow them to accommodate lithium ions into their structure. Recent work has demonstrated phosphate glasses (i.e., $\text{V}_2\text{O}_5 \bullet \text{P}_2\text{O}_5$, $\text{SnO}_2 \bullet \text{P}_2\text{O}_5$, $\text{TiO}_2 \bullet \text{P}_2\text{O}_5$, $\text{Fe}_2\text{O}_3 \bullet \text{P}_2\text{O}_5$, etc.)²⁰⁻²³ as highly reversible LIB anode materials with high capacities (>1000 mAh/g) and long-cycle stabilities (>1000 cycles).^{19,24}

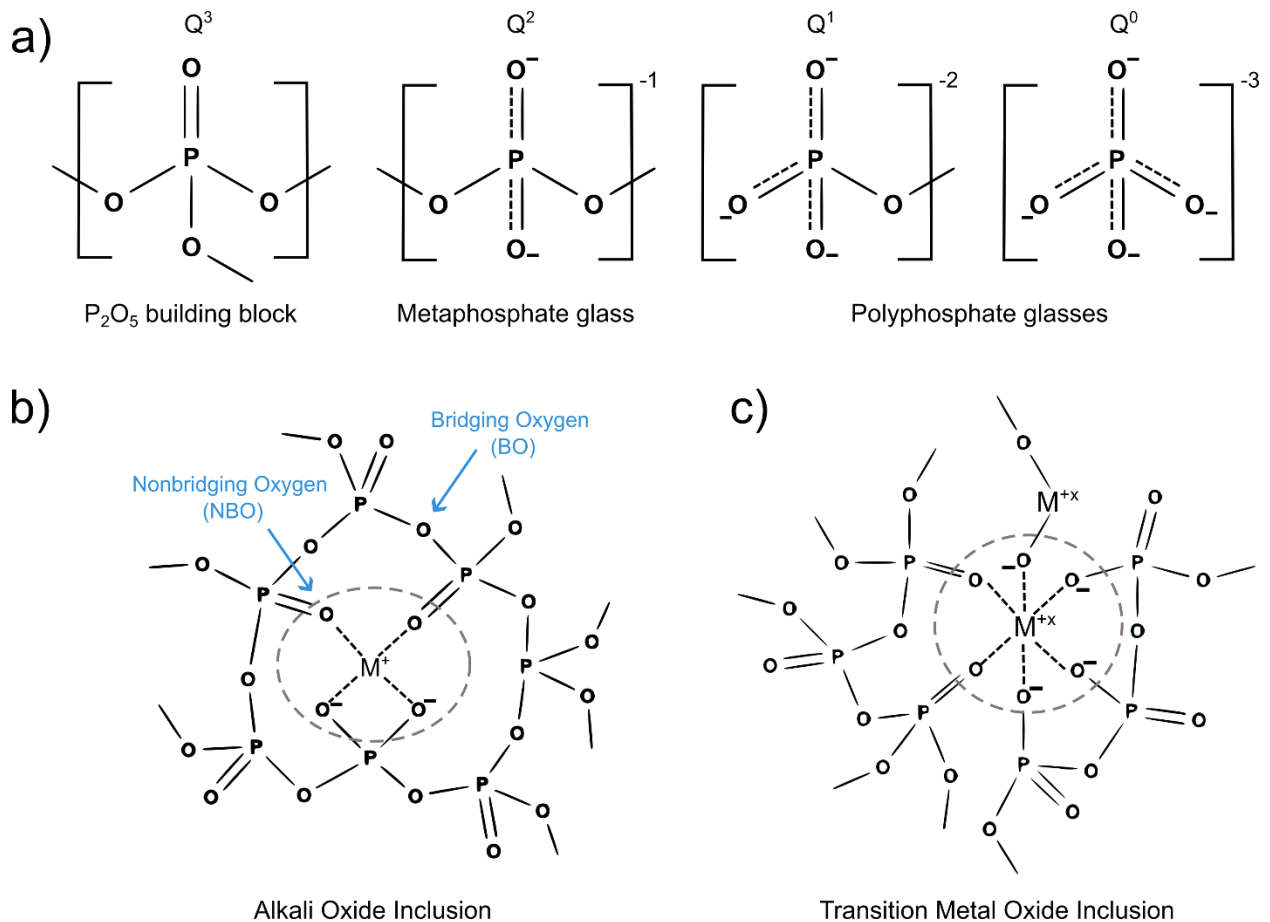


Figure 1.1. a) Representation of the different types of bonding seen in phosphate and metal phosphate networks. Adapted from Brow et. al.²⁵ Planar structural representation of b) alkali and c) transition metal cations in a phosphate network adapted from Varshneya et. al.¹⁹ Bridging and non-bridging oxygens are highlighted to show how cation valency affects phosphate bonding as described in (a).

Electronic conduction in amorphous mixed valency metal phosphates involves the transport of small polarons, which are distortions in the local structure due to a hole or electron defect. These charge carriers become more localized (and non-conducting) with increasing disorder in the structure; a process known as Anderson localization.¹⁹ Introducing a mixed valency cation (like V^{+4}/V^{+5}) into a phosphate glass leads to an increase in electronic conduction due to increasing amounts of small polaron formation. According to this model, the electronic conductivity in a mixed valency metal phosphate increases as the distance between small polarons

decreases. This can be accomplished by increasing the effective concentration of the mixed valency cations up to the point where the network is no longer continuous.²⁶

The factors that generally control the ionic conductivity in phosphate glasses are the coulombic barriers between sites (such as potential well confinement and jump distance) and strain of the “lattice” from moving sites. Martin et al. determined that the proximity of available sites is a critical factor in the determining the coulombic energy barrier. The hopping distance can be reduced by increasing the number of NBOs in a phosphate glass (controlled by varying the cation content in the phosphate). However, those NBOs must also allow the network to remain connected overall (i.e., be available sites for Li-ion hopping).^{19,27,28}

Li-ion conduction in phosphate glasses can vary depending on the degree of glass network modifier incorporation (metal oxide) and the valency of the cations. Introducing Li-ions into a phosphate system makes a modified random network in which there are regions of high BO-content and regions of high NBO-content, thus generating channels for the Li-ion conduction.¹⁹ When multivalent cations are introduced to the $\text{Li}_2\text{O}\cdot\text{P}_2\text{O}_5$ network, the number of NBOs can increase while maintaining high network connectivity.^{27,28} The degree of connectivity depends on cation valency and concentration. Increasing the number of NBOs can lead to shorter interstitial site distances and lower coulombic barriers for Li-ion hopping.²⁷ For example, $x\text{V}_2\text{O}_5\cdot(1-x)\text{P}_2\text{O}_5$ glass anodes show initially high capacities (1000-1150 mAh/g) due to improvements in conductivities with increasing V_2O_5 content. However, excessive V_2O_5 incorporation leads to interruption of Li-ion migration channels and an overall reduction in conductivity (reducing the material’s ability to store Li-ions at the same current load).²⁹

Many metal phosphate anodes undergo phase transitions (crystalline to amorphous) and face further glass network structural changes when cycling down to low potentials vs Li/Li^+ .²⁰⁻²³

Yamauchi et. al. demonstrated the $\text{SnO} \cdot \text{P}_2\text{O}_5$ glass network as an anode that initially showed long-range order in the phosphate structure but underwent simultaneous phosphate vitrification and tin oxide conversion to Sn metal at low potentials (0 V vs Li^+/Li). The structural change occurred over the first few cycles in which the incoming Li-ions replaced the vacancies left from $\text{Sn}^{(+x)}$ to $\text{Sn}(0)$ conversion. The newly Li-occupied sites cause an increase in BO formation, thus improving phosphate crosslinking and amorphization. Although the initial capacity was ~ 1150 mAh/g, the irreversible reaction in the formation cycles led to a subsequent stable capacity of ~ 600 mAh/g.²³ Similar cycling behavior is observed with $\text{V}_2\text{O}_5 \cdot \text{P}_2\text{O}_5$ glass anodes with initial capacities of ~ 1150 mAh/g that drop to ~ 400 mAh/g but remain stable over 100's of cycles.²⁹ High capacity retention is observed in multiple glass phosphate anode and cathode systems, a property which is owed to high tolerance to volume changes characteristic of glasses with large free volume.³⁰

1.4. Review of NASICON Bulk Materials System

Crystallization of phosphate glasses can be achieved by controlling the initial composition and annealing temperature. In the mixed metal phosphate glass-ceramic system, NASICON electrolytes are a garnet electrolyte which occupy a large compositional space with the chemical formula of $\text{Li}_{1-x}\text{M}_x\text{M}'_{2-x}(\text{PO}_4)_3$ where $\text{M} = \text{Al}^{+3}, \text{Cr}^{+3}, \text{Ga}^{+3}, \text{Sc}^{+3}, \text{Y}^{+3}, \text{In}^{+3},$ or La^{+3} and $\text{M}' = \text{Ti}^{+4}, \text{Ge}^{+4}, \text{Sn}^{+4}, \text{Hf}^{+4},$ or Zr^{+4} . The following section will discuss the role of crystalline $\text{LiTi}_2(\text{PO}_4)_3$ (LTP) and $\text{Li}_{1-x}\text{Al}_x\text{Ti}_{2-x}(\text{PO}_4)_3$ (LATP), where $\text{M} = \text{Al}^{+3}$ and $\text{M}' = \text{Ti}^{+4}$, as a versatile materials system for iontronics applications due to its ability to conduct and store Li-ions.

1.4.1. NASICON Solid State Electrolytes

There has been extensive work on the LTP and LATP NASICON system in bulk.^{31,32} These studies have demonstrated that annealing and sintering of amorphous composite powders at

elevated temperatures (650-1000 °C) crystallizes the material into the NASICON phase. The NASICON structure is a rhombohedral crystalline structure with PO₄ tetrahedra and TiO₆/AlO₆ octahedra. Due to the oxygen binding states in these polyhedra, there are two distinct interstitial Li sites in this structure through which the Li⁺ ions hop. Beyond 900 °C, the crystalline orthorhombic aluminum phosphate (AlPO₄) phase forms. These high temperatures lead to the removal of Al from the NASICON structure and an increase in secondary phases such as TiO₂ and Li₂O which have a very low Li-ion conductivities.³³

The improved performance in LATP is owed to the minimal Al⁺³ doping of LTP, which has high chemical and thermal stability, and low electronic conductivity.³³⁻³⁵ The effect of Al⁺³ replacing some Ti⁺⁴ ions is that oxygen electrons become more localized in the Ti-O bond, allowing for a decrease in strength of the Li-O interactions. Additionally, the smaller ionic size of Al⁺³ compared to Ti⁺⁴ induces densification of the film which reduces the unit cell size and film porosity. Ultimately, this densification allows more lithium into the film – particularly at grain boundaries – which is largely responsible for the drastic increase in ionic conductivity.^{32,33} Undoped NASICON LTP has been reported to have an ionic conductivity of 1x10⁻⁵ S/cm. However, LATP has demonstrated ionic conductivities up to 1x10⁻³ S/cm – nearing the upper bounds of bulk SSE materials (10⁻² S/cm).³⁶

1.4.2. NASICON Electrodes

LTP is traditionally an electron-blocking material, but it has been successfully made into an anode by mixing LTP particles with an electron-conducting material such as carbon or TiO₂ such that there exists a continuous electron conduction pathway.³⁷⁻⁴⁰ Crystalline LTP has been demonstrated as an anode material for aqueous alkali-ion batteries due to its chemical stability

with water, a reaction potential of -0.5 V vs SHE, and reversibility of Li^+ ion intercalation up to $\text{Li}_3\text{Ti}_2(\text{PO}_4)_3$.³⁷⁻⁴¹ As LIB anode, LTP-carbon composites were cycled reversibly in two different potential windows – $\text{LiTi}_2(\text{PO}_4)_3$ to $\text{Li}_3\text{Ti}_2(\text{PO}_4)_3$ from 1.5 to 3.5 V vs Li^+/Li and $\text{Li}_3\text{Ti}_2(\text{PO}_4)_3$ to $\text{Li}_6\text{Ti}_2(\text{PO}_4)_3$ from 0.25 to 1.2 V vs Li^+/Li .⁴²⁻⁴⁵ This body of literature demonstrates LTP as a material that can be adopted into multiple components of *iontronic* devices.

For NASICON LTP and its derivatives, it is hypothesized in the literature that at potentials from 2.8 to 1.5 V vs Li/Li^+ , Li-ions diffuse into the empty M1, M1', and M2 interstitial sites of $\text{LiTi}_2(\text{PO}_4)_3$, indicating a theoretical capacity of 169.6 mAh/g.^{39,44,46} Previous works have demonstrated that NASICON LTP and Fe-doped LTP (LFTP) anodes are quite stable at this potential window with capacities ranging from 100-140 mAh/g and clear redox peaks.^{38-40,43,44,46-50} However, Strout et. al., demonstrated that the NASICON structure is not stable at lower voltages. In the first discharge cycle down to 0.5 V vs Li^+/Li , the capacity is 567 mAh/g with distinct redox activity at 0.75 V vs Li^+/Li indicating additional lithium insertion in the system. As the system approaches 0.5 V vs Li^+/Li , the NASICON-type structure breaks down because it cannot support more than 2 additional stoichiometric lithium ions in its interstitial sites. The anode vitrifies at low voltages and does not recover the NASICON structure when cycled back up to 3 V vs Li^+/Li .⁴⁶ Despite the structural instability of the NASICON structure, the newly formed semicrystalline film continues to reversibly accept lithium ions into its matrix with capacities ranging between 100-250 mAh/g.^{43,46}

1.5. Atomic Layer Deposition as a Tool for Ion-Conducting Thin Films

ALD is a vapor phase deposition method known for its low temperature deposition, angstrom-scale thickness control, and compatibility with high aspect ratio substrate topologies. It

is a powerful technique due to the alternating sequential pulsing of gaseous metalorganic and oxidative hetero-reactive precursors. This is shown in **Figure 1.2a** for a generalized metal oxide ALD reaction in which the metalorganic precursor performs a ligand-exchange reaction with the hydroxylated surface. Once this precursor is purged out, an oxidant (typically H_2O , O_2 , or O_3) is introduced to the reactor to hydroxylate the metalorganic surface, completing one ALD cycle. The precursors are carried from a reservoir onto the film substrate by an inert carrier gas such as Ar. In this layer-by-layer approach, film composition can not only be modified by the selection of precursors in the process, but also by changing the nature of the carrier gas.^{51,52} Common metal precursors utilized in ALD processing are listed in **Table 1.1**.

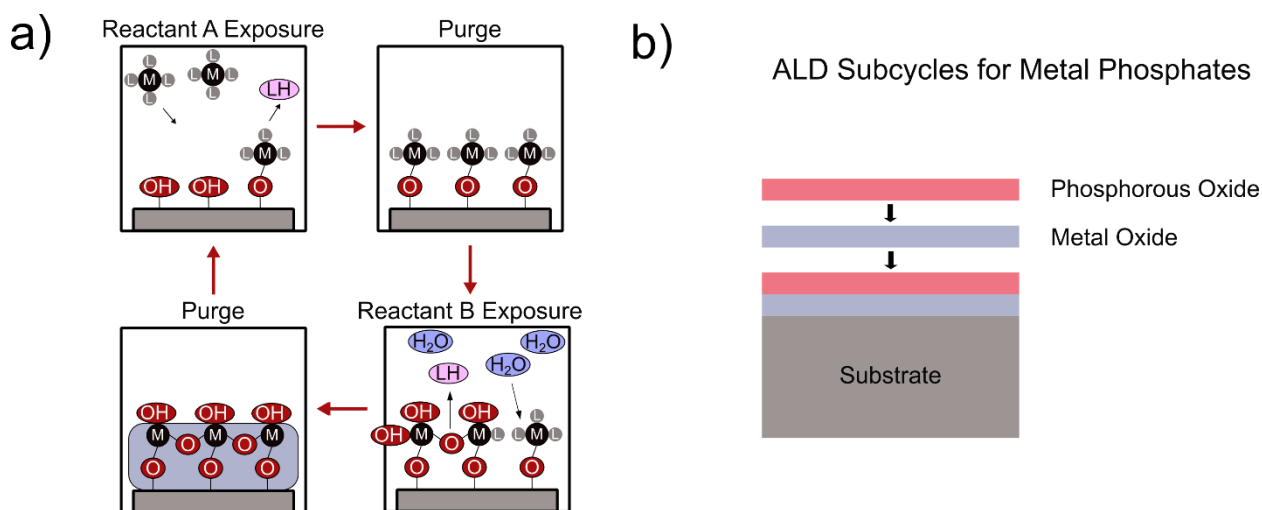


Figure 1.2. a) A generalized binary ALD process for a metal oxide thin film, which demonstrates the nature of the atomic-scale thickness control possible with ALD. b) A schematic of alternating between metal oxide and phosphorous oxide sub-processes to deposit a metal phosphate ALD film.

A phosphorous oxide can be made by a similar process as seen in **Figure 1.2a**, if the metalorganic precursor is replaced by a phosphorous-containing precursor.⁵³ As with metal oxides, the choice of oxidant in phosphorous oxides can vary and influence overall composition.⁵⁴⁻⁶⁰ A metal phosphate is then developed by alternating between metal oxide and phosphorous oxide sub-

processes (**Figure 1.2b**). Common phosphorous sources observed in ALD processes are listed in

Table 1.1.

Table 1.1. A list of common precursors for incorporation of elements relevant to the Li-Al-Ti-P-O system

| Element in Film | Precursor | Acronym | Examples in Literature |
|-----------------|-------------------------------------|-------------------|------------------------|
| P | trimethyl phosphate | TMP | 61–64 |
| | triethyl phosphate | TEP | 65 |
| | Tris(trimethylsilyl) phosphite | TTMSP | 58 |
| | Diethyl phosphoramidate | DEPA | 11,66,67 |
| | tris(dimethylamino)phosphine | TDMAP | 68,69 |
| Li | lithium <i>tert</i> -butoxide | LiOtBu | 11,64,68,69 |
| | Lithium bis(trimethylsilyl)amide | LiHMDS | 70,71 |
| Ti | Titanium (IV) chloride | TiCl ₄ | 54,58 |
| | Titanium (IV) isopropoxide | TTIP | 60,72 |
| | Tetrakis(dimethylamido)titanium(IV) | TDMAT | 73 |
| Al | Trimethyl aluminum | TMA | 63 |

1.5.1. Review of Metal Phosphate ALD Processes

A wide range of metal phosphate ALD processes have been developed to date, as shown in **Table 1.2**. The following sections detail the precursor chemistries involved in select metal phosphate ALD synthesis, and how ALD process parameters have been used to modify phosphate properties.

Table 1.2. ALD-developed metal phosphates.

| Phosphate Base | Chemistry | GPC (Å/cyc) | A ⁺ sigma_i @RT (S/cm) | Demonstrated Application | reference |
|---------------------------|---------------------------------|-------------|-----------------------------------|--------------------------|-----------|
| Lithium Phosphate | pLiPON | 1 | 1.5×10^{-7} | LIB SSE | 74 |
| | tLiPON | 0.9 | 6.5×10^{-7} | LIB SSE | 75 |
| | Li ₃ PO ₄ | 0.8 | 2.3×10^{-9} | LIB SSE | 76 |
| Titanium Phosphate | TiPO ₄ | 2.2 | - | Cathode | 58 |
| | TiP ₂ O ₇ | 6.6 | - | cathode | 72 |
| | TiPON | 6 | - | Cathode coating | 59 |
| Aluminum Phosphate | Al ₃ PO ₄ | 1.8 | - | Protection layer | 77 |
| | AlPON | 8 | - | Cathode coating | 67 |
| Iron Phosphate | LFP | 0.94 | - | LIB cathode | 61 |
| | Iron phosphate | - | - | LIB cathode | 60 |

1.5.1a. Lithium Phosphates

Though most ALD phosphates are amorphous as deposited,⁵³ ALD lithium phosphate can have varying degrees of crystallinity by controlling deposition temperatures, precursor choice, and carrier gas selection.^{67,78} Li-ion conductivities for ALD Li₃PO₄ range from 1.4×10^{-10} to 3.3×10^{-8} S/cm depending on the degree of crystallinity.⁷⁹ In the lithium phosphate system, it is thought that amorphous films outperform crystalline films due to increased phosphate network connectivity and reduced Li-ion hopping distance allowing for lower Li-ion migration energy barriers.⁸⁰ This rationale has led to a few instances of modifying the Li₃PO₄ network with glass formers such as N and Al to maximize the ionic conductivity.

Werbrouck et al. studied Al-doped Li₃PO₄ (LAP) with a LiHDMS as the lithium source, TMP as the phosphorous source, and TMA as the aluminum source. In this process, only 1% Al was incorporated into the film because most of the Al on the surface from the TMA pulse was removed by the subsequent TMP pulse.⁷⁹ Despite such low Al-doping, the ionic conductivity of LAP reached 1.5x10⁻⁷ S/cm. Due to the nature of the TMP/TMA reaction limiting the tunability of Al content in lithium phosphate, there is no current study on the effects of Al concentration and network structure in ALD LAP films. However, literature suggests that Al is acting as a glass former in the lithium phosphate network and decreasing the Li-ion migration activation energy.^{19,27,79}

There is a large body of literature on the effects of using nitrogen as a network modifier in lithium phosphate that forms a glassy structure called lithium phosphorous oxynitride (LiPON).^{62,64,81-84} Within the phosphate network, nitrogen breaks up P-O bonds to form one of two binding states – P-N<P (N_t) and P=N<P (N_d)⁸⁵ – that create sub structures of PO₃N and PO₂N₂.⁸⁰ The increase in covalency of P-N and P=N bonds reduces the strength of Li⁺-O⁻ interactions and reduces the number of BOs in the network. With increased nitrogen content, network connectivity improves and increases the Li-ion conductivity up to 10⁻⁶ S/cm (until recently, this high conductivity was achieved only by sputtering). With too much nitrogen in LiPON, the lithium environment changes such that there is the covalent nature of the Li-O interactions increases, which stagnates the Li-ion conductivity despite maintaining a well-connected network.⁸⁰ In ALD development of LiPON, different avenues have been pursued for nitrogen incorporation that have varying degrees of compositional control and Li-ion conductivity gains.

The first ALD LiPON thin film was a quaternary plasma-enhanced ALD (PEALD) process using either LiOtBu or LiHDMS as the lithium source, H₂O as the oxidant, TMP as the phosphorous source, and nitrogen plasma (pN₂) as the nitrogen source.^{64,83} This process allows for a high degree of compositional tunability and is desirable for the low temperature depositions made possible by PEALD. After the TMP/H₂O step, the radicals on the pN₂ break up the P-O bonds on the surface to form the LiPON glass. Phosphate cross-linking increases with longer pN₂ doses, which leads to a higher Li-ion conductivity of 1.5×10^{-7} S/cm – an order of magnitude higher than crystalline Li₃PO₄ by ALD.

Despite the improved conductivity, Li-ion conduction was limited by the type of nitrogen coordination (primarily N_t) possible with pN₂ as the nitrogen source. An alternative LiPON process was developed by Pearse et al. and Shibata et al. in which either DEPA or TDMAP were used simultaneously as phosphorous *and* nitrogen sources.^{75,86} Both DEPA and TDMAP have the advantage of having N_d coordinated nitrogen built into the precursor structure, thus maximizing the amount of N_d in the final film. Pearse et al. demonstrated a LiPON composition of Li₂PO₂N with dominant N_d coordination. The resulting ionic conductivity of 6.5×10^{-7} S/cm indicates that the N_d incorporation indeed improves network crosslinking.

Although this is a significant improvement, this ALD process tends to have higher carbon contamination left over from unreacted precursors that undoubtedly change the nature of the phosphate network. Compared to carbon, nitrogen is more efficient and improving network connectivity and reducing electrostatic barriers for Li-ions. Therefore, an ultraclean ALD process is required to have an uninterrupted phosphorous oxynitride network. Tsuruoka et al. achieved pristine ALD LiPON (< 3 at % carbon) with increased nitrogen content up to 13 at. % by combining the two approaches outlined above.⁶⁹ TDMAP was used as a phosphorous and nitrogen

source with built in N_d coordination. This was proceeded by an Ar plasma (pAr) or NH_3 plasma (p NH_3). pAr is effective at removing the surface ligands to minimize carbon contamination while crosslinking the phosphate network with both N_d and N_t coordination. However, p NH_3 allows for predominantly N_d coordination while introducing additional nitrogen into the LiPON film. The combination of precursor choice aided by PEALD yields an ALD LiPON film with an ionic conductivity of 1.65×10^{-6} S/cm.⁶⁹

1.5.1b. Titanium Phosphates

Titanium phosphate ALD thin films have been developed with various precursor combinations. Titanium phosphate ALD can generally be categorized as “thermal” ALD and PEALD processes. **Table 1.3** lists thermal ALD and PEALD processes for titanium phosphate, presenting a comparison of reaction conditions and precursor reactivity on the final composition and structure of the film.

Early thermal ALD process of titanium phosphate used a combination of $TiCl_4$, TMP, and H_2O , as seen in the works of Hämäläinen et al. and Wiedmann et al, which demonstrated a temperature dependence on the composition of titanium phosphate. In the $TiCl_4$ /TMP reaction (no H_2O) at a deposition temperature of 300 °C, the resulting composition is $Ti_{1.6}P_2O_{7.8}$. This composition can be broken down into various polymorphs of titanium phosphate (i.e., TiP_2O_7 , $TiPO_4$). However, X-ray photoelectron spectroscopy reveals that the Ti binding state is Ti^{+4} , which points to TiP_2O_7 . Instead, this film composition can be broken down into $TiP_2O_7 + TiO_2$, forming a composite with regions rich in phosphate and regions rich in oxide. In the $TiCl_4$ /TMP process at 300 °C, the phosphate to oxide ratio is 4:1. This ratio can be reduced to 5:2 ($Ti_{0.7}PO_{8.7}$) by introducing water after the TMP step ($TiCl_4$ /TMP/ H_2O). This decrease in relative amount of oxide is due to the hydroxylation step removing the TMP ligands from the surface and reducing steric

hinderance for the next reaction – thus allowing for a more complete reaction of TiCl_4 with the surface. However, the water step does not make the surface reaction favorable enough to completely remove the TiO_2 component in the titanium phosphate film.^{56,58}

Hämäläinen et al. demonstrated that the key to producing nearly stoichiometric TiP_2O_7 is to increase the reactor temperature to 400 °C, such that TiCl_4 and TMP have increased reactivity and leave little to no oxide sites behind on the surface. Although Dil et al. utilized TTMSp instead of TMP in their titanium phosphate process, they performed a thermal ALD process at 200 °C and saw a decrease in phosphate to oxide ratio to 1:3 ($\text{Ti}_{1.9}\text{PO}_{7.4}$) compared to the higher temperature counterparts. This further corroborates that reaction temperature is an important driving factor in controlling overall film composition and structure. This feature can be used to tune the structure of the film depending on the desired application.^{59,60}

Table 1.3. Summary of titanium phosphate ALD processes reported in literature comparing process conditions and resulting compositions. The precursors used are titanium tetrachloride (TiCl_4), titanium (IV) tetraisopropoxide (TTIP), triethyl phosphate (TEP), trimethyl phosphate (TMP), and tri(trimethylsilyl) phosphate (TTMSp) for titanium and phosphorous sources.

| Precursors Sequence | ALD type | Temp. (°C) | Composition | $\text{P}_x\text{O}_y:\text{TiO}_2$ ratio | Ref. |
|-------------------------------------------------|-----------------|------------|-----------------------------------------------|-------------------------------------------|------|
| TiCl_4/TEP | thermal | 200 | $\text{Ti}_3\text{PO}_{8.2}$ | 1:2 | 54 |
| TiCl_4/TMP | thermal | 300 | $\text{Ti}_{1.6}\text{P}_2\text{O}_{7.8}$ | 4:1 | 55 |
| TiCl_4/TMP | thermal | 400 | $\text{Ti}_{1.2}\text{P}_2\text{O}_7$ | ~1:0 | 55 |
| $\text{TiCl}_4/\text{TMP}/\text{H}_2\text{O}$ | thermal | 300 | $\text{Ti}_{0.7}\text{PO}_{8.7}$ | 5:2 | 56 |
| $\text{TiCl}_4/\text{TTMSp}/\text{H}_2\text{O}$ | thermal | 200 | $\text{Ti}_{1.9}\text{PO}_{7.4}$ | 1:3 | 58 |
| TTIP/pTMP/p O_2 | plasma-enhanced | 300 | $\text{Ti}_{1.1}\text{P}_{2.7}\text{O}_{6.1}$ | ~1:0 | 59 |
| TTIP/pTMP/p O_2 | plasma-enhanced | 300 | $\text{Ti}_{1.2}\text{P}_2\text{O}_{6.5}$ | ~1:0 | 60 |

PEALD is often advantageous when lower temperature reactions are desired. In PEALD a radicalized gas can reduce the activation energy of a reaction such that less external is required. Dobbelaere et al. identified TMP as the limiting factor in thermal ALD phosphate formation due to its low reactivity compared to the titanium precursors (TTIP and TiCl_4). They pulsed plasma Ar gas during the TMP pulse to generate TMP radicals (TMP^*) before TMP reaches the surface. This TMP^* is now more reactive and is better able to complete ligand exchange reactions with the titanium precursor (TTIP). This work demonstrates that a stoichiometric TiP_2O_7 can be achieved at lower temperatures than before (300 °C) by activating the TMP with PEALD.^{53,60} The stoichiometric TiP_2O_7 film achieved by PEALD was demonstrated as a working LIB cathode material, in which Li-ions were reversibly inserted and extracted from the metal phosphate network – indicating this ALD thin film behaves like the bulk metal phosphate glasses discussed in **Section 1.3**.⁷²

1.5.1c. Lithium Iron Phosphate

Although there is a variety of ALD metal phosphates, one of the only demonstrated mixed metal phosphate is lithium iron phosphate (LiFePO_4) – which has been used commercially in bulk applications as a LIB cathode material.^{60,61,87} Incorporating an additional metal into the film by ALD introduces a challenge in stoichiometry control due to the variable reactivity and chemical reactions involved with each precursor as well as overall complexity in the synthesis process. In many cases, this can be resolved by techniques such as super-cycling. LiFePO_4 was successfully deposited by super-cycling Li_2O and FePO_4 sub-cycles in a ratio of 1:5 $\text{Li}_2\text{O}:\text{FePO}_4$ to achieve the desired final stoichiometry. The resulting homogeneity of the film depends on the periodicity of

the super-cycle ratio and the extent to which the layers diffuse into one another during the deposition at elevated temperatures.⁸⁸

1.5.2. Further Development of Metal Phosphate ALD Processes is Necessary

A major challenge in the development of ALD Li-ion conductors has been to develop suitable high performing electrolytes for thin film solid state devices. LiPON has been the state-of-the-art thin film phosphate-based Li-ion SSE with an ionic conductivity of 1.65×10^{-6} S/cm. To date, LiPON still out-performs most other reported ALD thin film SSEs despite having a relatively low ionic conductivity in the context of bulk SSEs (with ionic conductivities up to 10^{-2}).^{17,36,74,75}

Efforts to produce higher ionic conductivity films have been made by looking at NASICON $\text{Li}_{1+x}\text{Al}_x\text{Ti}_{2-x}(\text{PO}_4)_3$ (LATP) due to its ionic conductivities ranging from 10^{-5} - 10^{-3} S/cm, anywhere from 1-3 orders of magnitude more conductive than LiPON.^{89,90} LATP is traditionally made by ball milling, melt quenching, or by the solgel method^{89,91}. The films produced by these methods are microns thick pellets and therefore not suitable for many microelectronics applications. There have been efforts towards thinner LATP films by RF sputtering and PLD.^{91,92} Film thickness ranges from 300-500 nm and the LATP films have comparable ionic conductivities to the standard bulk pellets. However, this chemistry is yet to be developed in ALD processing. Such an advancement in ALD thin film materials will enhance iontronic device performance in a way that is compatible with high aspect ratio structures used in the semiconductor industry.

The literature review of ALD metal phosphates highlights the versatility of this chemistry due to the many factors that can affect composition and structure (precursor choice, deposition temperature, carrier gas selection) before considering post-process annealing. In this dissertation, the understanding of phosphate chemistries in the literature will be applied to make more

compositionally complex films within the Li-Al-Ti-P-O materials system. With increasing complexity (i.e., adding lithium to a titanium phosphate process or aluminum to an LTP process), this work will highlight how the phosphate network structures change based on composition and reaction conditions. This work will then go beyond stoichiometric manipulation and will discuss crystallization dynamics of thin films in the Li-Al-Ti-P-O materials system, and how crystalline phases can be manipulated to select for desired electronic properties of the films.

Chapter 2: Experimental Methods

2.1. Atomic Layer Deposition Process Development

2.1.1. ALD Parameters/Conditions

2.1.1a. Precursor Details

Test-grade wafers (University Wafer) were pumped down to 10^{-7} Torr in a load-lock chamber before transferring them into the ALD reactor. Depositions were conducted at 300 °C in a Cambridge Nanotech (now Veeco) Fiji F200 Gen 1 ALD reactor coupled to an ultra-high vacuum (UHV) cluster system ($<10^{-8}$ Torr). ALD precursors used to complete this dissertation were lithium tert-butoxide (LiO^tBu) (Sigma, 97% and in-house synthesized), deionized water, trimethylphosphate (TMP) (Sigma, 99%), and titanium (IV) isopropoxide (TTIP) (Sigma, 99.99%), trimethyl aluminum (TMA) (STREM, 98%), oxygen gas (Airgas UHP, 99.99%). The base pressure of the ALD reactor was 1×10^{-6} Torr, and the process pressure was maintained at 200 mTorr by flow of UHP argon (Airgas, 99.999%) gas.

LiO^tBu Synthesis Procedure: In 2023 our source of LiOtBu stopped being sufficiently pure for our ALD reactions, leading to negligible reactivity and completely stopping production of lithium-containing films in our lab. Though we tried to source our LiOtBu elsewhere, we faced issues with the available alternatives. To go forward with the research, our group began synthesizing our LiOtBu precursor in house. LiOtBu was synthesized using tert-butanol (11.94 mL, 124.8 mmol) added to 50 mL of hexane. The mixture was cooled to 0 °C before adding n-butyllithium (11.35 mL, 11 M in hexane solution) in an argon atmosphere. The resulting solution was stirred at room temperature for 2 hours to react and form a solution of LiOtBu in hexanes. The solution was then dried to yield 14.982 g of LiOtBu as a fine white powder.

2.1.1b. Process Details

Table 2.1 describes the precursor conditions and pulse times used in all of the processes in this work. LiO^tBu was kept in a stainless-steel bubbler and delivered to the ALD reactor with 40 sccm argon carrier gas flow. Prior to the first LiO^tBu pulse delivery, the stainless-steel bubbler was kept at temperature for >10 hours to allow the LiO^tBu powder to sinter and prevent clogging of the precursor delivery manifold. TMP, and TTIP were all kept in stainless-steel vapor draw cylinders. All processes described in this section follow the precursor temperatures and pulse times highlighted in **Table 2.1**.

Table 2.1. ALD Precursor Details.

| Precursor | Temperature | Pulse time (s) | Role in Process | Process Utilization |
|--------------------------|-------------|-------------------|--------------------|---------------------------------------------------------------------------------------------------|
| LiO^tBu | 150 | 5 | Lithium-source | Li ₃ PO ₄ , LAP, tLTP, pLTP, tLATP |
| TMP | 70 | 0.2 | Phosphorous-source | Li ₃ PO ₄ , LAP, tLTP, pLTP, tLATP, tTiPO, pTiP ₂ O ₇ |
| TTIP | 100 | 0.2 | Titanium-source | tLTP, pLTP, tLATP, tTiPO, pTiP ₂ O ₇ |
| TDMAT | 115 | 0.2 | Titanium-source | tLATP |
| TMA | 25 | 0.06 | Aluminum-source | LAP, tLATP |
| H₂O | 25 | 0.06 | oxidant | Li ₃ PO ₄ , LAP, tLTP, tLATP, tTiPO |
| pO₂ | 25 | 5 | oxidant | pLTP, pTiP ₂ O ₇ |

Table 2.2 shows a list of the basic processes and sub-processes that were used to control the metal phosphate compositions throughout this work (using pulse times in **Table 2.1**). The following process descriptions will refer to the sub-processes in **Table 2.2**.

Table 2.2. Process sequences for each sub-cycle used as a building block to tune the composition of the metal phosphate films in this dissertation.

| Process Chemistry | Process Sequence |
|--------------------------------|------------------------------------------------------|
| Li ₂ O | LiOtBu / H ₂ O |
| PO _x (thermal) | TMP / H ₂ O |
| PO _x (plasma) | TMP (with flowing plasma Ar) / O ₂ plasma |
| Al ₂ O ₃ | TMA / H ₂ O |
| TiO ₂ | TTIP or TDMAT / H ₂ O |

Li₃PO₄ was deposited by alternating between Li₂O and PO_x (thermal) sub-cycles. LAP was deposited by inserting a single Al₂O₃ cycle for every x Li₃PO₄ cycles. Thermal titanium phosphate (TiPO) was deposited by alternating between TiO₂ and PO_x (thermal) sub-cycles. Thermal LTP was deposited by inserting a single Li₂O cycle for every n TiPO sub-cycles. Thermal LATP was deposited by inserting a single Al₂O₃ cycle for every y TiPO sub-cycles *and* a single Li₂O cycle for every n TiPO sub-cycles. TiP₂O₇ was deposited by alternating between TiO₂ and PO_x (plasma) sub-cycles. Plasma enhanced LTP was deposited by inserting a single Li₂O cycle for every n TiP₂O₇ sub-cycles. All processes have 20 second Ar purge after each precursor pulse.

2.1.2. Spectroscopic Ellipsometry

Real-time *in-situ* monitoring of film thickness was performed using a J.A Woollam M-2000D spectroscopic ellipsometer with a spectral range of 193-1000 nm. Film thicknesses were fit

to an optical Cauchy model and the measurements then verified by cross-sectional scanning electron spectroscopy (SEM).

2.1.3. X-Ray Photoelectron Spectroscopy (XPS)

Post-deposition, films were transferred under UHV to a Kratos Ultra DLD Surface Analysis system (1×10^{-9} Torr) for XPS analysis. XPS data were collected using a monochromatic Al K α (1486 eV) X-ray source at 15 kV and a total anode power of 150 W. Survey spectra were collected with a pass energy of 160 eV and binding energy step size of 1 eV. High resolution spectra were collected with a pass energy of 20 eV and a binding energy step size of 0.1 eV at the appropriate number of scans to produce a satisfactory signal/noise ratio. Casa XPS was used to analyze all data. XPS peaks were fit using a Shirley background and 30/70 Gaussian/Lorentzian pseudo-Voigt functions. Elemental quantification was done by comparing the ratios of high-resolution peak areas with the tabulated Kratos relative sensitivity factors. All spectra were charge calibrated to the C 1s peak at 284.8 eV.

2.2. Structural Characterization

2.2.1. Annealing Procedures

For Raman, XRD and XPS measurements, films were annealed at various times and temperatures in a tube furnace under a flowing N₂ environment. Some films were allowed to radiatively cool and others were quenched to room temperature on a metal table acting as a heat sink. For impedance and electrochemical measurements, films were annealed in the rapid thermal annealer (RTA) at 650 °C for 8.5 minutes under a flowing N₂ atmosphere and subsequently quenched to room temperature.

2.2.2. Raman Spectroscopy

Raman measurements were recorded in air with a “Labram HR” microscope system (Horiba Jobin Yvon USA). A 633 nm laser (HeNe) with a D1 intensity filter was used. The incident laser power was controlled to 1 mW and $\sim 2\mu\text{m}$ diameter spot size with a 100x microscope objective. A 600 gr/mm grating was used for acquisitions with 20s exposure and 5 repetitions.

2.2.3. X-Ray Diffraction

XRD was performed by a PANalytical XPert Pro MRD system in a grazing-incidence (GI)-XRD configuration with a scan rate of 0.025 °/s and step size of 0.05 °. Cu-K α ($\lambda = 1.54 \text{ \AA}$) radiation source was used. The diffraction patterns were compared with primary references from the International Center for Diffraction Data (ICDD) for identification. Rietveld Refinement was performed using Profex.

2.2.4. Microscopy

Scanning Electron Microscopy (SEM). SEM and focused ion beam (FIB) cross-sections were performed on a dual-beam field emission SEM/FIB system (Tescan, XEIA3) with a 10 kV acceleration voltage.

Transmission Electron Microscopy (TEM). TEM imaging was performed using a JEOL JEM-2100F operated at 200 kV. All images were formed on a Gatan OneView CMOS camera.

TEM Sample preparation. TEM cross-sections were prepared by hand polishing using a PELCO Tripod Polisher followed by final thinning in a Gatan PIPS II ion polisher.

2.3. Impedance and Electrochemical Measurements

2.3.1. Electrochemical Impedance Spectroscopy & DC Relaxation

All samples used for electrochemical impedance spectroscopy and DC relaxation were prepared in a vertical metal-insulator-metal stack configuration. An ALD metal phosphate layer was deposited on a metal bottom contact on 1x1 cm Si chips with 500 nm of SiO₂ as an insulating layer (Si/SiO₂/Au or Si/SiO₂/Pt). The ALD layer was patterned with a 0.6 cm² stainless-steel shadow mask to leave exposed metal on the edges of the chips. After the ALD deposition, a stainless-steel shadow mask with circular holes 400 μm in diameter was placed above the ALD layer to pattern a top current collector of Au, forming a vertical stack for impedance testing.

Electrochemical impedance spectroscopy (EIS) was performed with a Biologic VSP potentiostat in an argon-filled glovebox (MBraun) maintained at <0.5 ppm H₂O and O₂. Finished devices were placed on a custom-built mica glass-ceramic stage with a proportional integral-derivative (PID) temperature controller. Electrical contact was made with micromanipulator probes. EIS measurements were made at temperatures between 25 and 100 °C at frequencies of 200 kHz to 250 mHz with an AC amplitude of 20 mV.

DC relaxation was performed by applying a series of DC voltages (50, 100, 350, 500 mV) for 10 minutes each. *Sample Preparation:* LTP was deposited on Si/SiO₂/Ti/Pt stacks.

2.3.2. Electrochemical Measurements

The samples for liquid cell electrochemical measurements were prepared identically to the description in **Section 2.3.1**, but no top current collector layer was deposited after the ALD layer. Liquid based electrochemistry measurements were performed in a 2-electrode beaker cell in a 1 M LiClO₄ in propylene carbonate (Sigma Aldrich) and a Li metal anode punched out from Li foil.

Chapter 3: Effect of Metal Phosphate ALD Network on Thin Film Electrical Properties

3.1. Chapter Summary

The strategy for ALD Li⁺ ion conductors to date has largely focused on the amorphization of binary metal phosphates like Li₃PO₄ by introducing glass-formers such as Al⁺³, Si, or N. While this strategy has led to success for the state-of-the-art ALD electrolyte lithium phosphorous oxynitride (LiPON), new strategies for glassy electrolytes need to be explored. This chapter delves deeper into understanding the limits of Al-doping Li₃PO₄ as a solution for fast Li-ion conduction as well as looking at alternative strategies. For example, multivalent metal phosphates can promote network connectivity due to higher coordination numbers. This effect combined with glass forming effect of Al⁺³ shows promise in pushing the boundary of fast Li⁺ conductors beyond 10⁻⁷ S/cm.

This chapter details the ALD process development of various metal phosphates with tunable phosphate networks and their corresponding electrical properties. Section 3.2 discusses the effects of Al-doping of Li₃PO₄ in more detail than has been reported in the literature with the goal of understanding the limits of the glass forming effect of Al⁺³ and what changes to the phosphate network occur at high and low extremes of aluminum doping. ALD process development of lithium titanium phosphate (LTP) based processes are found in Section 3.3 in which XPS reveals the overall changes to the phosphate network bonding depending on precursor choice and process conditions. Section 3.4 discusses the consequences that ALD processing (and corresponding glass network character) has on electrical properties in the LTP-based glass network.

3.2. Al^{+3} as a Glass Former in the Lithium Phosphate System

3.2.1. ALD Process Development of Al-doped Lithium Phosphate

Al-doped Li_3PO_4 (LAP) was developed by super-cycling trimethyl aluminum (TMA) and H_2O into the well-established Li_3PO_4 process which uses lithium tert-butoxide ($LiOtBu$) and trimethyl phosphate (TMP) as shown in **Figure 3.1a**.⁷⁶ ALD process parameters were probed by using in-operando spectroscopic ellipsometry to determine the temperature window and precursor pulse times. We note that the TMA/ H_2O super-cycle was attempted both before and after the $LiOtBu/H_2O$ pulse to check for reaction compatibility. The order of the TMA/ H_2O pulse did not affect the GPC of the LAP film, nor did it have a notable effect on the chemical properties. The symmetry of the reactions is not surprising due to the high reactivity of TMA with -OH terminating surfaces.⁹³ The growth rate per cycle (GPC) of LAP with 2 at. % Al as a function of reaction temperature is relatively constant between 250-300 °C with a GPC of 0.8 Å/cyc at 250-275 °C and a slight increase to 0.9 Å/cyc at 300 °C as seen in **Figure 3.1b**. This is within the range of growth rates found in literature for Li_3PO_4 0.7-1.2 Å/cyc and Al_2O_3 0.9-1.1 Å/cyc.^{78,94}

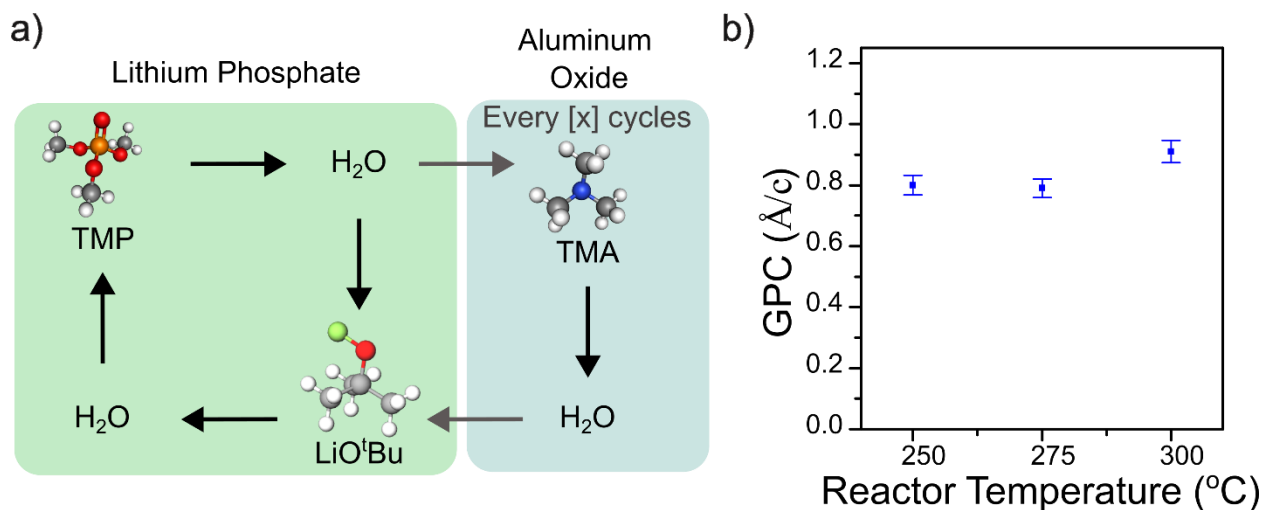


Figure 3.1. a) schematic of ALD precursor sequence for LAP with lithium phosphate and aluminum oxide subcycles. b) Growth rate of LAP over the temperature range between 250-300 °C.

Chemical and Structural Characterization. The range of aluminum concentrations accessible with the super-cycling method are shown in **Figure 3.2a**. Super-cycling ratios of $\text{Li}_3\text{PO}_4:\text{Al}_2\text{O}_3$ ranging between 1-120 shows a rapid decline in aluminum concentration from a supercycle ratio of 1 (21.4 at. % Al) to 5 (3.7 at. % Al). Using a supercycle ratio of 120, the aluminum concentration can be tuned down to 0.9 at. %. The profile of phosphorous and lithium mirror that of aluminum with increasing supercycle ratio, indicating that at higher concentrations of aluminum there is reduced lithium phosphate. However, the oxygen profile is more nuanced – likely due to the re-distribution of BOs and NBOs with varying degrees of Li^+ and Al^{+3} ions in the phosphate network.

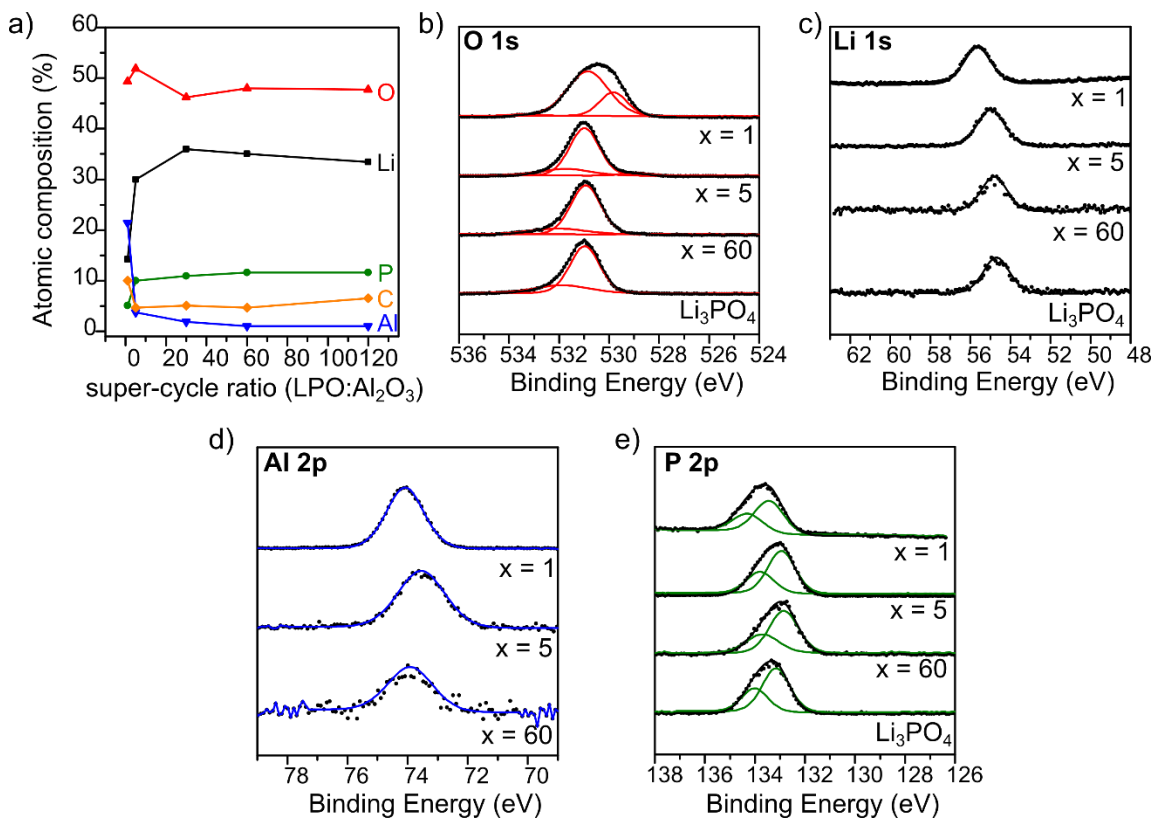


Figure 3.2. a) atomic composition breakdown by element of LAP films with respect to super-cycle ratio. Normalized high resolution spectra of Li₃PO₄ and LAP films: b) O 1s, c) Li 1s, d) Al 2p, and d) P 2p.

The nature of the phosphate network can be better understood by analyzing the high resolution XPS spectra, which shows any changes in binding environment with respect to the changing aluminum concentration. **Figure 3.2b-e** shows the high resolution spectra of O 1s, P 2p, Al 2p, and Li 1s, respectively, comparing Li₃PO₄ and LAP with different supercycle ratios. The O 1s spectra of Li₃PO₄ shows a peak at 531 eV representing the P-O bonding in the phosphate network and a peak at 531.9 eV indicating carbon contamination (corroborated by the C 1s spectra).^{64,75} The O 1s spectra of x = 60 (1 at. % Al) remains largely unchanged except for a small component that emerges at 528.6 eV indicating Li₂O formation.⁹⁵ This agrees with the picture of multivalent ion doping generating more BOs in the phosphate network as described in **Section 1.3**.

However, at higher aluminum concentrations, the low binding energy peak shifts to 529 eV for $x = 5$ (3.7 at. % Al) and 529.8 eV for $x = 1$ (21.4 at. % Al). This shift to higher binding energies indicates LiAlO_2 formation for $x = 5$ and AlPO_4 formation for $x = 1$.^{96,97}

Further evidence of phosphate network modification by Al^{+3} is found in the Li 1s and Al 2p high resolution spectra. The Li 1s peak for pristine Li_3PO_4 is at 54.7 eV, in agreement with literature of semicrystalline lithium phosphate.⁶⁴ With only 1 at. Al ($x = 60$), the Li 1s peak shifts by 0.1 eV to 54.8 eV. However, the shift becomes more dramatic with 3.7 and 21.4 at. % Al (55.0 and 55.6 eV, respectively) due to the new LiAlO_2 binding environment.⁹⁶ The Al 2p high resolution spectra agree with the trends found in Li 1s and O 1s. In samples with only 1 at. % Al ($x = 60$), the Al 2p peak starts at 73.9 eV – indicating predominantly Al-O-P bonds with Al acting as a dopant to the phosphate network. At 4.7 at. % Al ($x = 5$), the Al 2p peak shifts to 73.4 eV, which more closely represents generation of a LiAlO_2 subphase. At this point aluminum is not just a glass former but is a network modifier.¹⁹ With the maximum aluminum concentration of 21.4 at. % ($x = 1$), most of the aluminum has formed an aluminum phosphate (AlPO_4) subphase, shifting the Al 2p peak back to 74.1 eV.⁹⁸ Likewise, the P 2p spectra shows a minor shift to lower binding energies in both $x = 60$ and $x = 5$ compared to Li_3PO_4 . In cases with aluminum dosing < 4 at. %, the dominant P-O bonding is of the lithium phosphate network in which Al^{+3} doping lowers the binding energy by creating a less covalent phosphate bond. However, at high aluminum concentrations ($x = 1$), the P 2p peak shifts to higher binding energies (133.4 eV), in agreement with AlPO_4 formation.⁹⁸

Along with chemical modifications that impact the type of phosphates present in the film, Al-doping can also impact the crystallinity of Li_3PO_4 . Al^{+3} is known to be a glass-former in metal phosphate films, which is evident in the XRD for varying levels of Al-doping in **Figure 3.3**. The

normalized pristine Li_3PO_4 spectrum demonstrates peaks associated with crystalline Li_3PO_4 annealed at 250-300 °C with the dominant diffraction peaks appearing at 22.3° and 23.2° 2 θ for the (120) and (101) indices (PDF Card 00-015-0760). It is common to see semi-crystalline as-deposited Li_3PO_4 by ALD despite most other metal phosphates being amorphous.⁵³ The normalized LAP XRD spectrum shows a reduction in signal-to-noise ratio accompanied by peak broadening compared to the Li_3PO_4 spectrum, indicating loss of crystallinity even at dosing levels as low as 0.9 at. % Al.

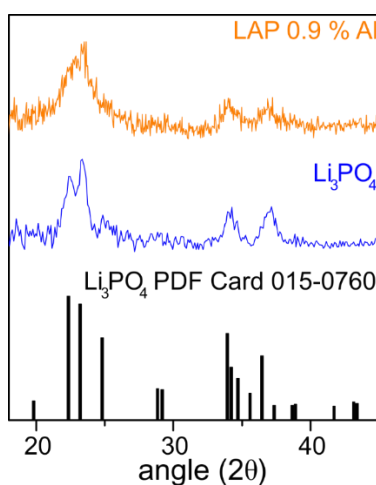


Figure 3.3. Normalized XRD spectra of LAP $x = 60$ (0.9 % Al) (orange), lithium phosphate (blue), and a reference lithium phosphate (black).

3.2.2. Ion Conduction in Al-doped Lithium Phosphate

Electrochemical impedance spectroscopy (EIS) was performed on the LAP and LPO thin films, as shown in the Nyquist plot in **Figure 3.4a**, to understand the evolution of ionic behavior with respect to aluminum concentration. Analysis of Nyquist plots requires fitting the data with an equivalent circuit model in which the electrical components of the circuit represent physical phenomena in the materials system.^{99,100} Therefore, some assumptions need to be established gathered by XPS and XRD results:

1. The sample is composed of a metal-insulator-metal stack in which the metals are imperfect ion-blocking materials (see inset in **Figure 3.4a**).
2. When Li_3PO_4 is the insulator, it is a semicrystalline film composed of some Li_3PO_4 grains embedded in a compositionally similar amorphous matrix.
3. When LAP (any composition) is the insulator, the Li_3PO_4 grains are disrupted by a compositionally non-uniform matrix of some form of Li-Al-P-O.

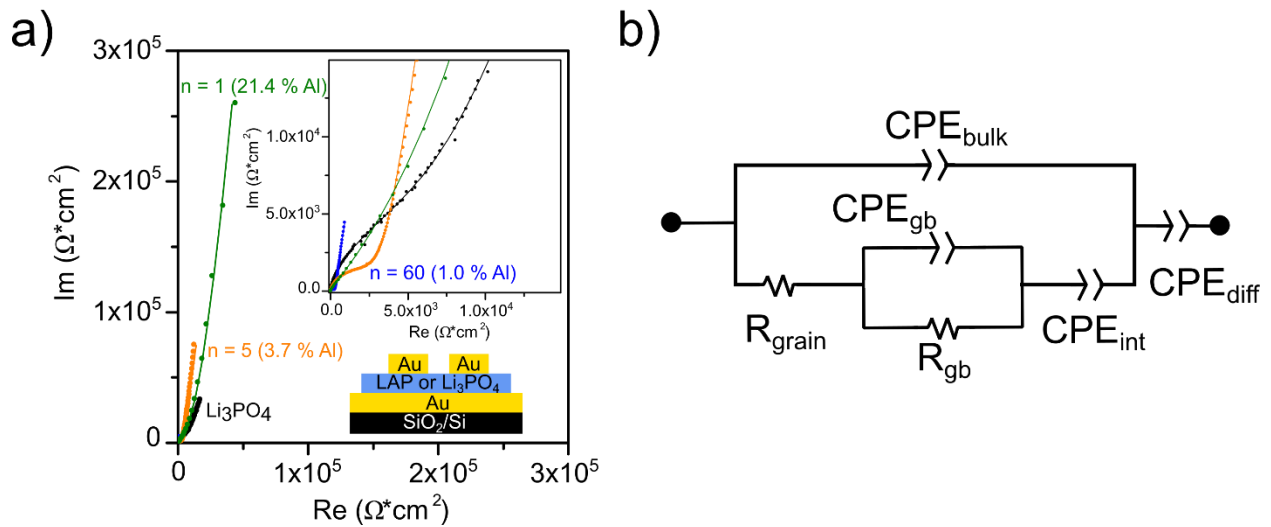


Figure 3.4. a) Normalized Nyquist plot of Li_3PO_4 (black), LAP $x = 1$ (green), LAP $x = 5$ (orange), and LAP $x = 60$ (blue, inset) films measured in a metal-insulator-metal stack (inset). b) Diagram of equivalent circuit used to fit the Nyquist plots and extract ionic conductivities of the grain and grain boundary components.

In both the LAP and Li_3PO_4 films there are grain boundaries that must be considered when a small AC voltage is applied across the MIM stack and the frequency is varied. The ions have a frequency-independent resistance through the grains and the grain boundaries, represented by R_{grain} and R_{gb} in series, respectively. At high frequencies, the Li^+ ions oscillate over a short distance, polarizing and forming a bulk capacitance, represented by CPE_{bulk} in **Figure 3.4b**. Ions at the grain boundaries or amorphous region also get polarized and form a grain boundary

capacitance, CPE_{gb} . At low frequencies, the ions are allowed to diffuse to the ion-blocking interface, forming a space charge region and an interfacial capacitance represented by CPE_{int} . The resistance values R_{grain} and R_{gb} can be extracted by fitting the Nyquist plots to this equivalent circuit. The ionic conductivity can then be calculated by plugging in R_{grain} and R_{gb} into R in **equation (1)** where σ_i is the ionic conductivity, R is the resistance (extracted from the equivalent circuit model fitting), L is the sample thickness, and A is the cross-sectional area of the measurement.

$$\sigma_i = \frac{L}{RA} \quad (1)$$

Both Li_3PO_4 and LAP show semicircular arcs at high frequencies with a diffusion tail at low frequencies. **Table 3.1** shows the results of fitting the Li_3PO_4 and LAP films of various concentrations. According to the fitting results, the ionic conductivity of the crystalline grains in the pristine Li_3PO_4 is 8.4×10^{-8} S/cm with a grain boundary conductivity of 7.3×10^{-10} S/cm. Upon doping of only 1 at. % Al, the grain ionic conductivity increases to 5.3×10^{-7} S/cm – an order of magnitude increase, like Werbrouck et. al. in their 1 at. % Al doped lithium phosphate.⁷⁹ The grain boundary component also increases up to 3.4×10^{-8} S/cm. The increase of the grain conductivity is owed to the glass forming nature of Al^{+3} and the increase in NBOs to improve Li^+ conduction (observed by Li_2O formation in the XPS O 1s spectra). Due to the partial amorphization of the film, there may be a smoother transition between grain and grain boundary, where the grain boundary also sees network rearrangement that benefits ion conduction.

Table 3.1. Ionic conductivity values as calculated from R2 and R3 in **Figure 3.4b**, representing the crystalline phases and grain boundaries in the Li₃PO and LAP films, respectively.

| Sample Chemistry | Aluminum concentration (%) | Grain Conductivity (S/cm) | GB Conductivity (S/cm) |
|---------------------------------|----------------------------|---------------------------|------------------------|
| Li ₃ PO ₄ | 0 | 8.4x10 ⁻⁸ | 7.3x10 ⁻¹⁰ |
| LAP x = 60 | 1.0 | 5.3x10 ⁻⁷ | 3.4x10 ⁻⁸ |
| LAP x = 5 | 3.7 | 1.0x10 ⁻⁷ | 2.2x10 ⁻⁹ |
| LAP x = 1 | 21.4 | 3.9x10 ⁻⁸ | 1.7x10 ⁻¹⁰ |

However, beyond 1 at. % Al, the ionic conductivity begins to drop in both the grain and grain boundary components. XPS analysis revealed that at 3.7 at. % Al (x = 5), there is an emergence of a LiAlO₂ subphase, which is known to have a low ionic conductivity on the order of 10⁻⁹ S/cm (measured at 400 °C) for crystalline γ -LiAlO₂,¹⁰¹ up to 10⁻⁸ S/cm with a modified defect structure.¹⁰² Other techniques like XRD and ^{Li}NMR may give helpful hints about what order of magnitude to expect from the LiAlO₂ subphase. But, with the available information, 2.2x10⁻⁹ S/cm is within reason. The decrease in grain conductivity at this aluminum concentration indicates that the grain composition or phosphate network connectivity is changing due to the addition of a secondary phase. This is further corroborated by the x = 1 sample with 21.4 at. % Al, in which the grain conductivity drops back down to 3.9x10⁻⁸ S/cm. XPS analysis revealed that with this much aluminum, AlPO₄ begins to form. AlPO₄ domains disconnect the lithium phosphate network and return that part of the sample back to undoped or nearly undoped lithium phosphate. EIS, XRD and XPS results, together, show that aluminum acts as a glass network former in low doping amounts (< 3.7 at. %) in which the lithium phosphate network connectivity is maximized for Li⁺ conduction. However, at higher concentrations (> 3.7 at. %), aluminum starts to become a network

modifier that separates the phosphate network into different domains with varying Li^+ conduction abilities.¹⁹

3.2.3. Discussion on Aluminum as a Dopant and Modifier in Lithium Phosphate Network

An interesting comparison between ALD chemistries for LAP processes can be made that suggests that the nature of the ALD reaction can impact the tunability of Al-doping and type of phosphate network available based on the reaction pathway. XPS and XRD data for both Al-doping methods demonstrates that changing how Al is introduced into the film can lead to different kinds of modifications to the lithium phosphate structure. Early efforts on LAP thin films by ALD were discussed in **Section 1.5.1a** of the work of Werbrouck et. al. in which TMA was dosed in between LiHDMS and TMP ALD precursors. Werbrouck et. al. assert that TMA acts to polymerize the TMP to form lithium pyrophosphate ($\text{Li}_4\text{P}_2\text{O}_7$) which is largely responsible for the change in crystallinity with the TMA dose despite only incorporating 1% Al. This was analyzed by structural techniques such as XRD and FTIR and by comparing the O/P ratio in films with and without a TMA step. In their work the O/P ratio decreased from 4.4 (Li_3PO_4) to 3.9 (LAP), indicating a mixture of ortho and pyrophosphates due to the TMA/TMP reaction. This is not the case for the LiO^tBu LAP process in this work. Instead, the O/P ratio *increases* from 4.4 (Li_3PO_4) to 4.8 (LAP) – indicating LAP predominantly forms an orthophosphate with the ALD process developed in **Section 3.2.1**. XPS and XRD also indicate that the dominant phosphate peak corresponds to the orthophosphate, not pyrophosphate.

A possible hypothesis for the differences between this work and that of Werbrouck et. al. is that the water step after each precursor in this work generates a different leaving group on the surface and changes the reaction core. Werbrouck et. al., TMP removes the $-\text{Al}(\text{CH}_3)_2$ group, likely forming gaseous $\text{Al}(\text{CH}_3)_3$ byproducts – thus removing most of the Al on the surface with very

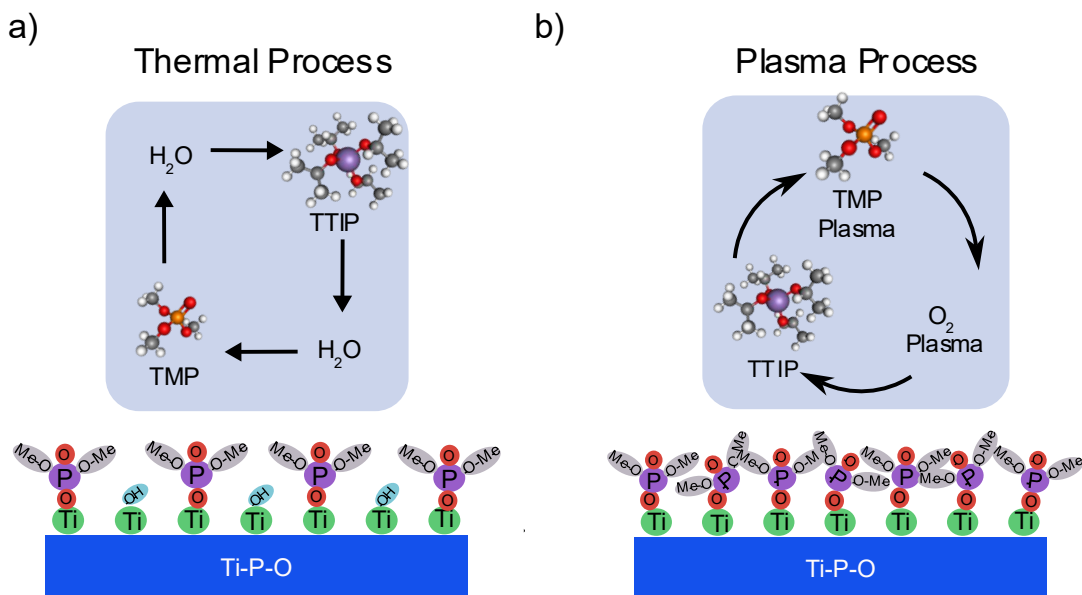
little selectivity. In this work, TMA follows the $\text{LiOtBu}/\text{H}_2\text{O}$ reaction that leaves an OH-terminated surface. TMP then reacts with the Al-OH surface to form $\text{Al-PO}(\text{CH}_3)_2$ on the surface and CH_3OH gaseous byproducts. In this case, the amount of aluminum in the film can be finely tuned simply by controlling the number of TMA/ H_2O pulses in the ALD process. To truly understand the differences between these reactions, further work would be needed such as in-situ quadrupole mass spectroscopy such that the byproducts of each reaction can be detected to help predict a reaction mechanism.

3.3. Glass-formers: Li and Al in the Ti-P-O System ALD Processes

3.3.1. Tunable TiO_2 Content in Titanium Phosphate ALD Process

Titanium phosphate (TiPO) serves as the building block for the $\text{Li}_{1-x}\text{Ti}_{2-x}\text{Al}_x(\text{PO}_4)_3$ NASICON system that will be explored in the remainder of this work. In the bulk, NASICON anode particle composites were achieved by mixing LTP with a carbon additive to provide the necessary electronic conduction for electrode functionality.^{39,46} In thin films, a nanocomposite could, in principal, be developed in which LTP and an electronically conducting phase co-exist to have mixed ionic/electronic conductivity. In the Ti-P-O system, it is feasible to control the composition and crystalline phases such that TiO_2 – an electronic conductor due to small electron polaron hopping¹⁰³ – can serve a similar role as carbon-black in bulk LTP anodes.^{49,104}

Scheme 3.1. Simplified reaction schematic and molecular representation of a) thermal titanium phosphate ALD process and b) plasma titanium phosphate ALD process.



As discussed in **Section 1.5.1b**, the choice of precursor and process conditions enables control over the purity of a titanium phosphate thin film. As seen in previous works, thermal ALD processes result in composite glasses of $\text{TiO}_2 + \text{TiP}_2\text{O}_7$ while PEALD allows for deposition of pure TiP_2O_7 . **Scheme 3.1a-b** shows the thermal (a) and PEALD (b) reaction sequences selected for this work with TTIP as the titanium source, TMP as the phosphorous source, and H_2O or pO_2 as the choice of oxidant. The film surface diagram in **Scheme 3.1a** shows a simplified view of the top layer that has partially exposed Ti-OH on the surface after the TMP pulse that allows for TiO_2 formation with subsequent cycles. On the other hand, the effect of the activated TMP plasma is shown in the film surface diagram of **Scheme 3.1b**, in which the TMP fully saturates the surface to form pure titanium phosphate. The O 1s high resolution XPS spectra (**Figure 3.5**) of the thermal and PEALD processes show peaks at 533.5 eV (C-O), 531.8 eV (P-O), and 530.8 eV (Ti-O). In the thermal process, Ti-O bonding consists of 25.1 at. % of oxygen bonding, whereas in the

PEALD process the Ti-O bonding is negligible. This indicates that we have a reliable method to control the presence of the TiO₂ subphase in the Ti-P-O film.

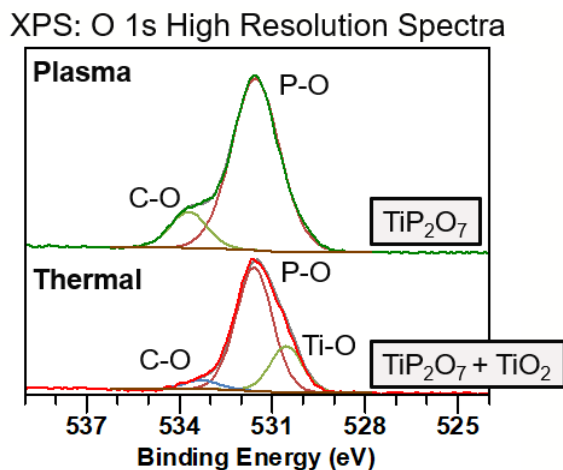


Figure 3.5. O 1s high resolution XPS spectra of plasma titanium phosphate (top) and thermal titanium phosphate (bottom) ALD thin films.

3.3.2. Lithium Titanium Phosphate (LTP) ALD Process Development

Thermal ALD Process. The supercycling sequence between lithium oxide (Li₂O) and titanium phosphate (TiPO) that was used to vary the LTP composition is shown *scheme 3.2a*. Adjustment of the LTP stoichiometry was achieved by changing the super-cycling ratio, n , between the values of 1-10. *Scheme 3.2b* shows an exaggerated representation of the film growth with this super-cycling approach. The thermal TiPO process with TMP, TTIP, and H₂O precursors was chosen as described in the previous section to simultaneously introduce a phosphate and oxide component, similar to previous works.^{54,56,58}

The atomic composition with respect to the super-cycling ratio is shown in **Figure 3.6a** in which a ratio of $n = 0$ is titanium phosphate only. Quantitative analysis of the titanium phosphate film approximately indicates a 1:2 ratio of TiP₂O₇:TiO₂. The lithium atomic % varies the most across the super-cycling range (34.4 to 8.3 atomic %). The titanium atomic % increases gradually

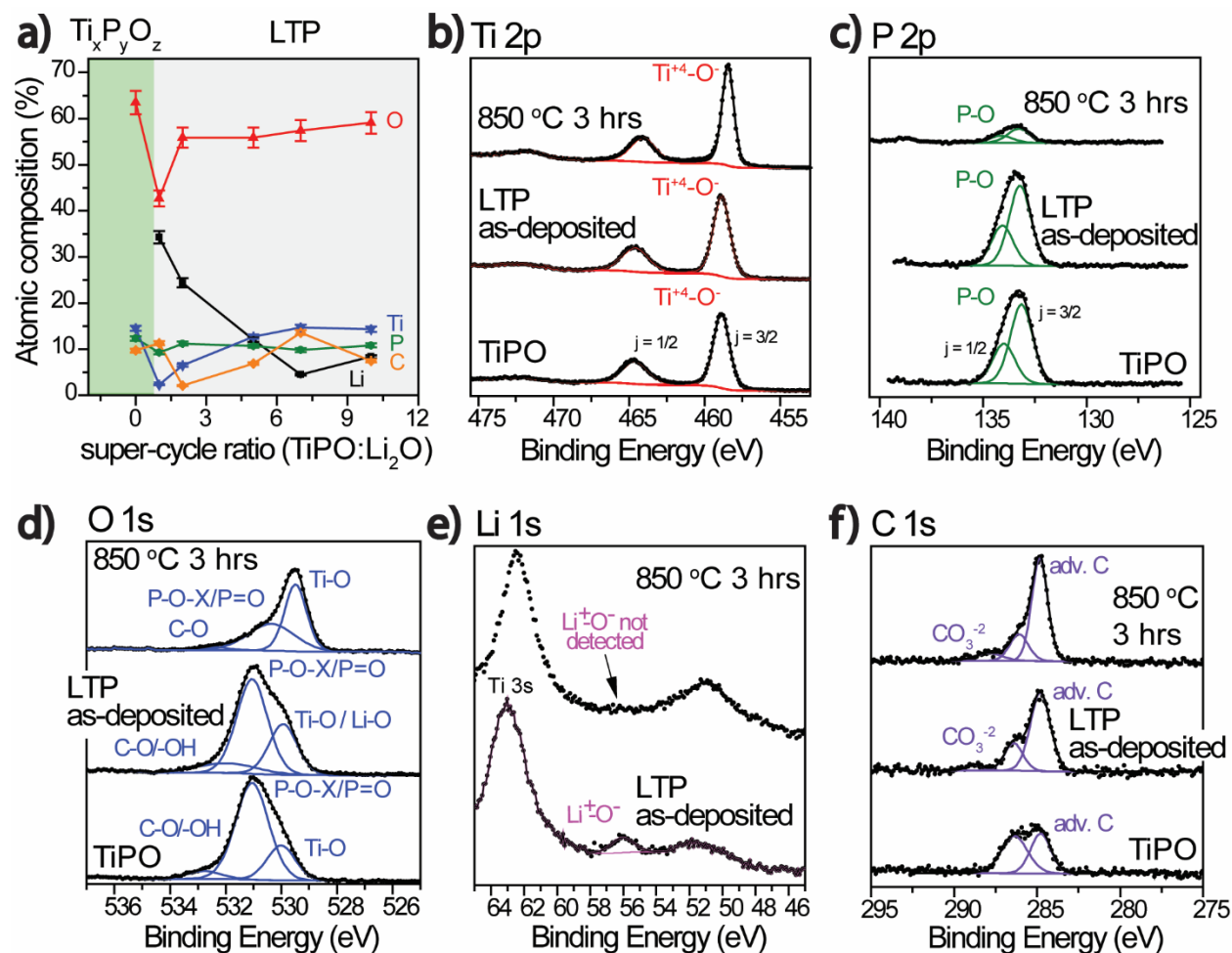


Figure 3.6. a) Atomic composition of thermal LTP system with respect to super-cycle ratio. High resolution XPS spectra of b) Ti 2p, c) P 2p, d) O 1s, e) Li 1s and f) C 1s for TiPO, thermal LTP ($n = 7$) as deposited, and thermal LTP ($n = 7$) annealed at 850 °C for 3hrs.

XPS of the as-deposited LTP film shows 4.5 atomic % lithium with a binding energy of 56.0 eV. The O 1s, Ti 2p, and P 2p spectra in LTP remain largely unchanged upon addition of Li by the super cycling method. However, the C-O component in the O 1s region of as-deposited LTP appears broader and is shifted to lower binding energies by 0.5 eV compared to TiPO. This is likely due to formation of Li-OH from the Li₂O monolayers which overlaps with the low end of

the C-O binding energy region.⁹⁵ Additionally, the peak previously assigned at Ti-O is slightly broader and more intense due to the presence of Li-O bonds that overlap with this region.^{54,58,95}

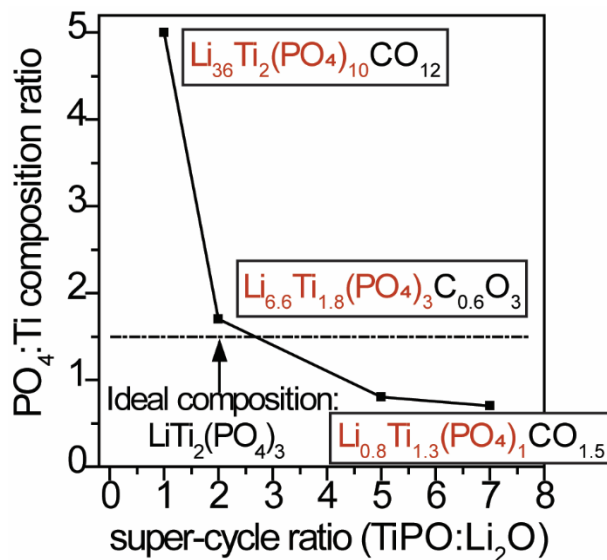


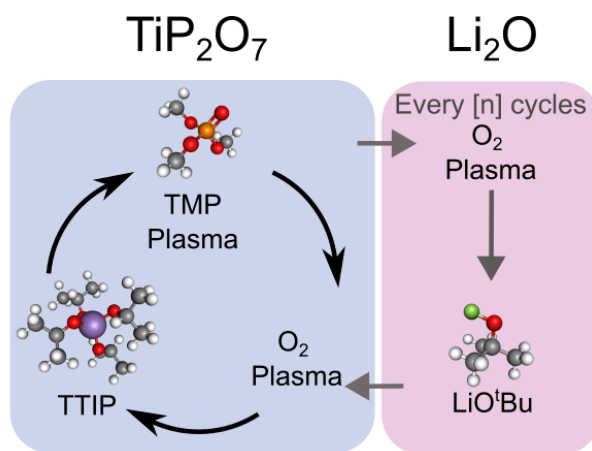
Figure 3.7. Ratio of PO₄:Ti with respect to super-cycle ratio as an ideality marker of the LTP stoichiometry.

There is a large collection of literature on bulk LTP that indicates the ideal composition is LiTi₂(PO₄)₃ for optimized ionic conductivity of this material in its NASICON crystalline phase due to the Li⁺-conducting 3D network that is formed.^{89,105} In **Figure 3.7** we show the stoichiometries at each super cycle ratio along with the ideal ratio defined as PO₄:Ti (a ratio of 1.5 corresponds to the ideal LTP stoichiometry). The PO₄:Ti ratio has a decaying profile with increasing super-cycling ratio. At one extreme (super-cycle ratio, n = 1) there is excess of both Li and PO₄ in the film, with a composition of Li₃₆Ti₂(PO₄)₁₀CO₁₂. On the other extreme (super cycle ratio, n = 7), there is excess Ti with a composition of Li_{0.8}Ti_{1.3}(PO₄)₁CO_{1.5}. The middle ground appears to be with a super cycle ratio of 2 where there is good agreement between the ideality ratio while also retaining some excess Li in the film (with a composition of Li_{6.6}Ti_{1.8}(PO₄)₃C_{0.6}O₃) before annealing.

Figure 3.7 summarizes these data and demonstrates the chemical tunability of the process, in which the super cycle ratio can be chosen such that there is excess Li, PO₄, or Ti in the as-deposited film. In **Chapters 4 and 5**, we primarily focus on thermal LTP films with super cycle ratios of $n = 1, 2,$ and 7 to illustrate the consequences of initial film stoichiometry on post-annealing crystal structure and electrochemical performance in the NASICON family of materials.

Plasma Enhanced ALD Process. For an electronically insulating LTP film, the supercycling method was used with a PEALD TiPO process and Li₂O as the sub-cycles (**Scheme 3.3**), such that the oxide content is minimized.

Scheme 3.3. Supercycle scheme for plasma-enhanced ALD of lithium titanium phosphate



The XPS spectra in **Figure 3.8a-d** directly compares the PEALD and thermal LTP processes. The 529.5 eV O 1s peak associated with M-O bonding (M = Ti, Li) shifts to lower binding energies by 0.3 eV, indicating weaker Ti-O bond strength. The P-O-X/P=O (X = P, Ti) peak at 530.6 eV shifts to lower binding energy by 0.4 eV, consistent with an increase in the weaker P-O-X bonds and decrease in the stronger P=O that generates non-bridging oxygens.^{106,107} This suggests that the LTP phosphate network has higher connectivity in the PEALD process compared to the thermal process. The Ti 2p $j = 1/2$ and $j = 3/2$ peaks shift to a more metallic state (-0.2 eV

shift) that is likely a result of the redistribution of oxygen electron density favoring phosphorous in Ti-O-P. The Li 1s peak in the PEALD LTP shifts to higher binding energies by 0.3 eV, showing more ionic character in the well-connected phosphate network. Perhaps surprisingly, the compositional breakdown shown in **Figure 3.8f** shows that pLTP ($n = 2$) and tLTP ($n = 2$) are almost identical except for higher carbon content in the pLTP ($n = 2$) process. However, XPS fitting analysis indicates that there is a notable difference in the phosphate network type that will be reflected in the electrical properties of these films (discussed in further detail in **Section 3.4**).

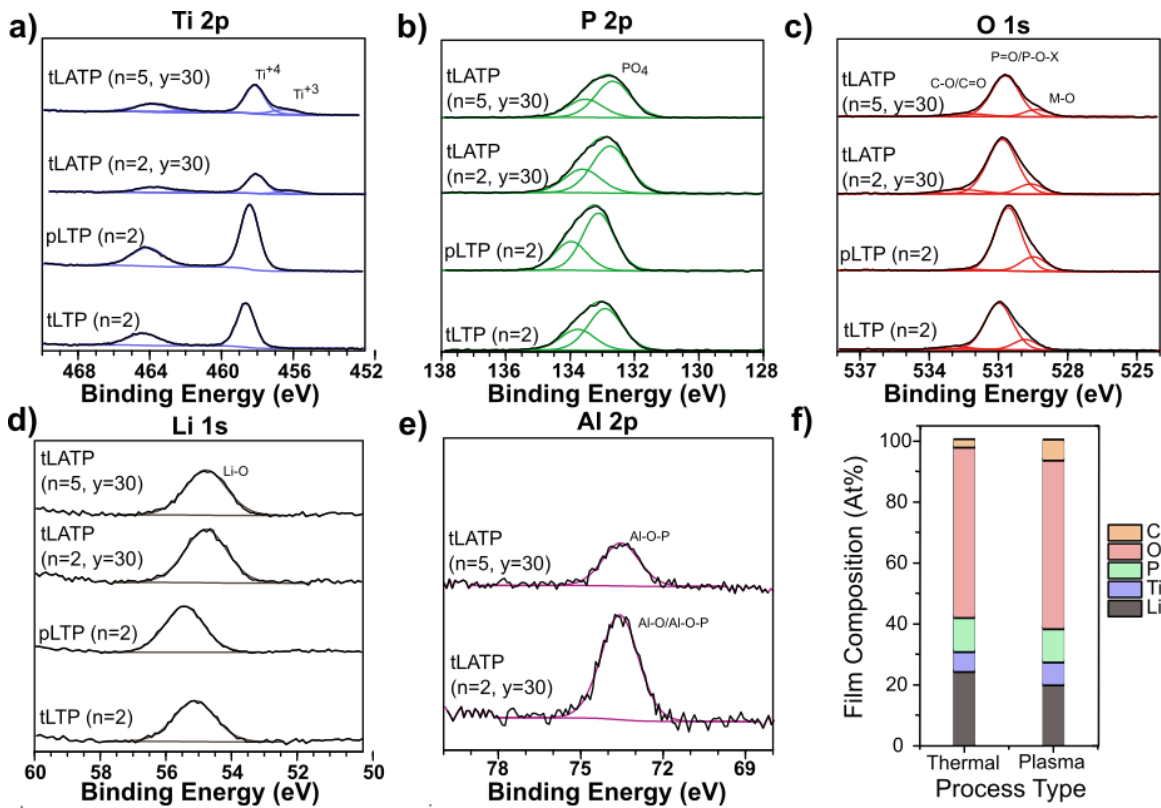


Figure 3.8. High resolution XPS spectra of a) Ti 2p, b) O 1s, c) O 1s, d) Li 1s, and f) Al 2p of thermal LTP ($n = 2$), PEALD LTP ($n=2$), thermal LTP ($n = 2, y = 30$), and thermal LTP ($n = 5, y = 30$) from bottom to top. f) Compositional breakdown of thermal LTP ($n = 2$) and PEALD LTP ($n = 2$).

3.3.3. Lithium Aluminum Titanium Phosphate (LATP) ALD Process

As discussed in the **Section 1.4**, the NASICON crystalline phase performs best with an $\text{Li}_{1-x}\text{Al}_x\text{Ti}_2\text{-x}(\text{PO}_4)_3$ composition – corresponding to 1-2 at. % Al-doping in LTP. With that goal in mind, an ALD process of thermal TiPO, Li_2O , and Al_2O_3 subcycles were used to deposit amorphous LATP as depicted in **Scheme 3.4**. In this process, a monolayer of Li_2O is deposited every n cycles of TiPO and a monolayer of Al_2O_3 is deposited every y cycles of TiPO to tune the LATP composition. This section details the chemical characterization of the as-deposited LATP and implications for how Al^{+3} doping can alter the LTP glass network.

Scheme 3.4. Supercycling scheme of the thermal LATP process of thermal TiPO with Li_2O every n cycles and Al_2O_3 every y cycles.

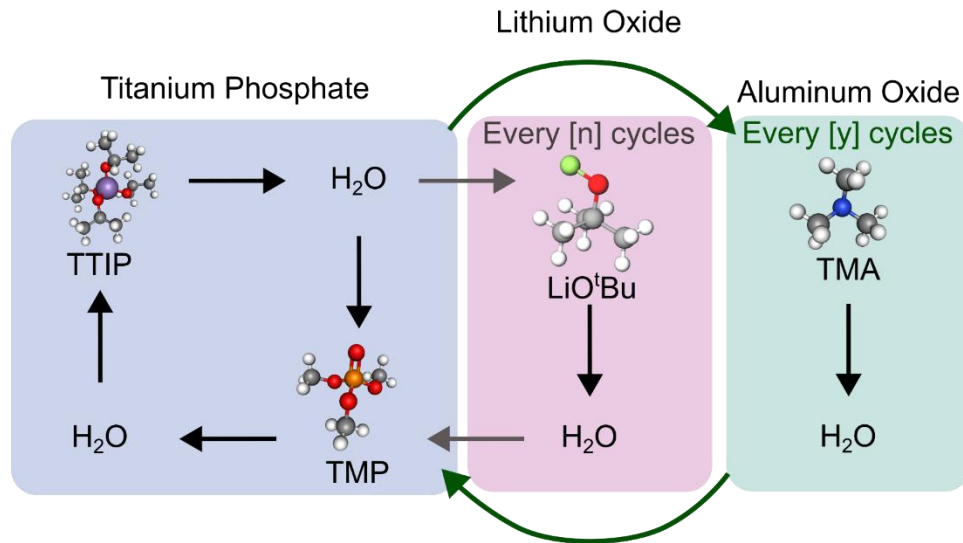


Table 3.2 shows the compositions of the two LATP films that were studied in this work. A supercycling ratio of $n = 2$ and $y = 30$ was chosen as the starting point to serve as a direct comparison for both the tLTP ($n = 2$) and LAP ($x = 30$) discussed in previous sections. At this supercycling ratio Al-doping is 1.2 at %, in agreement with the Al-doping work in the LAP thin films. The drop in Ti at. % from 7.3 to 3.9 at. % between tLTP ($n = 2$) and LATP ($n = 2, y = 30$) suggests that Al^{+3} is taking the place of Ti^{+4} in the phosphate network.

An additional supercycling ratio of $n = 5$ and $y = 30$ was chosen to show the consequences of changing the supercycle ratio and as a direct comparison to tLTP ($n = 5$). In this case, the titanium in the film is partially recovered to 7.5 at. % by increasing the number of TiPO cycles between Li_2O monolayers, while the aluminum content increases to 6 at. %. Again, this suggests that the Al atoms are partially replacing the Ti in the phosphate network. Like the tLTP ($n = 5$) film, the L ATP ($n = 5, y = 30$) film is Li- and PO_4 -deficient relative to the ideal composition for the NASICON crystalline phase (based on a composition of $\text{Li}_{2.8}\text{Al}_{1.2}\text{Ti}_{1.5}(\text{PO}_4)_2\text{C}_{1.1}\text{O}_9$).

Table 3.2. Compositions of thermal L ATP ($n = 2$ or $5, y = 30$) compared to thermal L TP ($n = 2$ or 5) as-deposited films.

| n Li₂O | y Al₂O₃ | Li (at %) | Al (at %) | Ti (at %) | P (at %) | O (at %) | C (at %) |
|------------------------------------|------------------------------------------------|------------------|------------------|------------------|-----------------|-----------------|-----------------|
| 2 | 30 | 24.7 | 1.2 | 3.9 | 9.9 | 53.5 | 6.8 |
| 2 | - | 23.9 | - | 7.3 | 10.9 | 54.6 | 4.3 |
| 5 | 30 | 14.1 | 6 | 7.5 | 10.2 | 56.3 | 5.9 |
| 5 | - | 12 | - | 12.7 | 10.7 | 57.7 | 6.9 |

The high resolution XPS spectra in **Figure 3.8a-e** show the L ATP ($n = 2, y = 30$) and L ATP ($n = 5, y = 30$) that can be compared directly to the chemical environments of the PEALD and thermal L TP ($n = 2$) processes discussed in the previous sections. In both L ATP films the Ti 2p spectra show two distinct bonding environments at 458.1 eV and 456.2 eV corresponding to the Ti^{+4} and Ti^{+3} $j = 3/2$ peaks, respectively. The Ti^{+4} components in both films shift to lower binding energies by -0.5 eV compared the tLTP ($n = 2$) film, indicating that the Ti^{+4} state has weaker Ti-O interactions. Likewise, the P 2p $j = 1/2$ and $j = 3/2$ peaks shift to lower binding energies by -0.1 eV compared to tLTP ($n = 2$) due to an increase in the relative amount of ionic character of the phosphate bonds (i.e, Ti-O-P and Al-O-P as opposed to more covalent P-O-P) with the

incorporation of aluminum in the film. The P-O-X/P=O components in the O 1s spectra for L ATP at 530.8 eV lie between tLTP (n = 2) and pLTP (n = 2) indicating a decrease in the relative amount of terminal P=O bonds present in L ATP compared to the thermal LTP process. Despite L ATP being a thermal process with higher propensity for oxide formation, these results suggest that the L ATP phosphate network generally has more bridging oxygens with lower binding energies than that of the thermal LTP process. Aluminum in L ATP is acting as a glass former and connecting the phosphate network by interrupting the TiO₂ domains and creating more Ti-O-P and Al-O-P bonds. Lastly, the Li 1s peaks for both of the L ATP films are at lower binding energies 54.8 eV compared to the LTP processes, due to a more delocalized Li⁺ environment. In the next section we will discuss implications of these changes in the phosphate network structures of LAP, tLTP, pLTP, and L ATP on Li⁺ and e⁻ conduction.

3.4. Effects of Network-Type and Local Structure on Thin Film Properties

Electrochemical impedance spectroscopy (EIS) was used on metal-insulator-metal stacks of the thermal LTP (n = 2), PEALD LTP (n = 2) and L ATP (n = 2, y = 30) thin films to understand the consequences of the process-induced glass network structure and electronic properties. The Nyquist plot of the tLTP (n = 2) film (**Figure 3.9a**) features a high impedance asymmetric semicircle with no diffusion tail, indicating possible electronic leakage. DC relaxation (**Figure 3.9b**) results in a measured electronic leakage current of 9.7×10^{-11} S/cm. As discussed in XPS measurements of tLTP (n = 2), this film has a high degree of oxide content embedded in the lithium titanium phosphate glass network due to the thermal ALD titanium phosphate reaction (discussed in **Section 3.3.1**). Given the evidence of electronic leakage from DC relaxation and EIS, it is reasonable to assume that the density of the TiO₂ domains is high enough to form a continuous electronic conduction pathway (depicted in **Figure 3.9c**). Although it is difficult to ascertain from

this evidence alone due to the amorphous nature of this film, these assumptions are further confirmed with a combination of diffraction and EIS measurements of crystalline versions of tLTP ($n = 2$) in **Sections 4.2 and 5.2**.

An equivalent circuit model shown in **Figure 3.9d** was used to fit the Nyquist plot based on the assumptions that there are parallel Li-ion and electron conduction paths through the lithium titanium phosphate and amorphous TiO_2 , respectively. In this equivalent circuit model, constant phase elements (CPEs) are used to represent imperfect capacitances in the material. $\text{CPE}_{\text{interface}}$, and CPE_{bulk} represent capacities at the film/metal interface and the bulk of the film, respectively. R_{TiO_2} represents the electronic conduction through TiO_2 domains. R_{LTP} and represents Li^+ ion conduction through the lithium titanium phosphate. The electronic conductivity resulting from the equivalent circuit model fit is $4.1 \times 10^{-10} \text{ S/cm}$, in agreement with the DC relaxation measurements. The ionic conductivity of the glass phosphate network of $2.1 \times 10^{-9} \text{ S/cm}$ falls short of the expected literature value of 10^{-6} S/cm of LTP.⁹² This can be explained by the presence of the TiO_2 domains creating a tortuous pathway for Li^+ within the phosphate glass and increasing the hopping distance for Li^+ conduction (**Figure 3.9c**). This is a likely scenario supported by bulk phosphate work that shows similar behavior due to large amounts of oxide disrupting network connectivity.^{27,108}

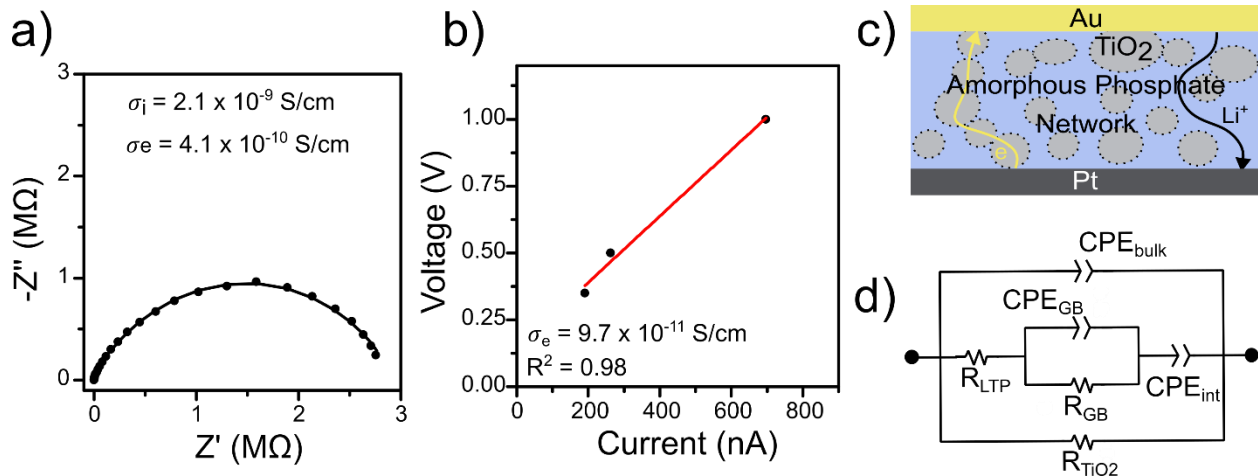


Figure 3.9. Impedance results of the Pt/tLTP/Au metal-insulator-metal stack of a) Nyquist plot from EIS and b) DC relaxation data. c) Physical representation of ionic and electronic behavior in the tLTP ($n = 2$) film and d) corresponding equivalent electric circuit used to fit the Nyquist plot in (a).

Unlike the tLTP ($n=2$) film, the Nyquist plot of pLTP ($n = 2$) film (**Figure 3.10a**) indicates that it is electronically insulating due to the diffusion tail at low frequencies. This is confirmed by DC relaxation experiments that show a current below the detection limit of the instrument. The equivalent circuit used to fit the Nyquist plot is a simple Randall's circuit (**Figure 3.10c**) that assumes a homogeneous Li^+ conductor with no electronic leakage (depicted in **Figure 3.10b**). Like in the previous equivalent circuit model, $\text{CPE}_{\text{interface}}$, and CPE_{bulk} represent capacities at the film/metal interface and the bulk of the film, respectively. R_{LTP} represents Li^+ ion conduction through the lithium titanium phosphate, and CPE_{diff} represents the Li^+ diffusion into the imperfect ion-blocking metal contacts.^{99,109} The ionic conductivity of pLTP ($n = 2$) is 1.5×10^{-6} S/cm, exceeding the that of the state-of-the-art ALD Li^+ conductor lithium phosphorous oxynitride (LiPON) by an order of magnitude.^{64,75}

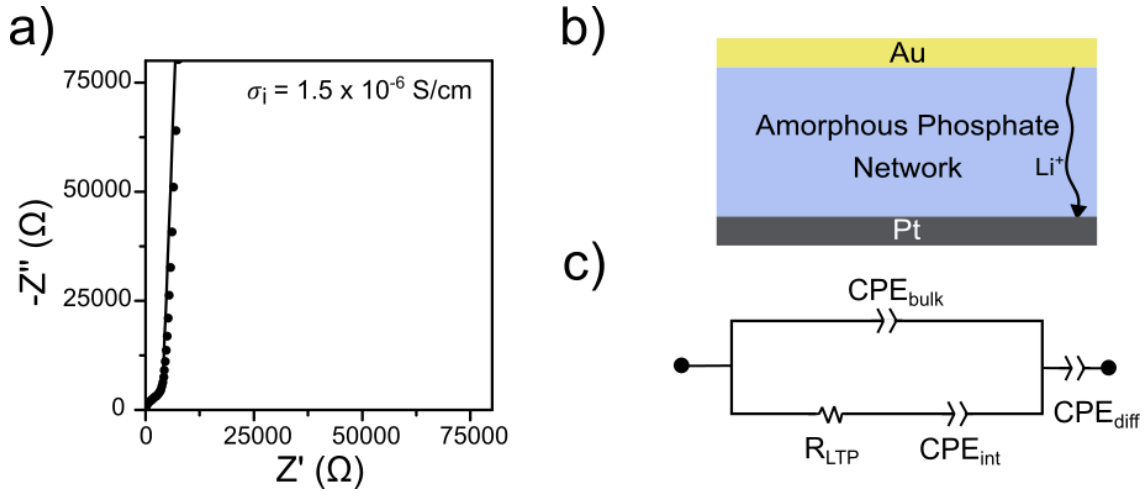


Figure 3.10. a) Nyquist plot of pLTP ($n = 2$) with corresponding b) physical representation of film structure and c) equivalent circuit model.

Figure 3.11a shows the Nyquist plot for the LTP ($n = 2, y = 30$) film in which there is a flattened semicircle at high frequencies followed by a diffusion tail at low frequencies. The insulating character of this film (confirmed by DC relaxation) indicates that the Al-doping of thermal LTP has sufficiently disrupted the TiO_2 domains and removed a viable electron conduction pathway. The asymmetry of the Nyquist plot suggests that there exists a low impedance Li^+ conducting phase and a high impedance phase that retains some capacitance separate from the interfacial capacitance between the film and the blocking electrodes. There is not enough information to confidently identify what the high impedance phase may be, but it is likely a result of a capacitance between small isolated TiO_2 domains and the LTP phosphate network. A schematic of the hypothesized sample structure is shown along with the corresponding equivalent circuit model (**Figure 3.11b-c**). The equivalent circuit model is a modified Randall's circuit similar to **Figure 3.10c** but with an additional RC circuit in series with the bulk Li^+ conduction representing the capacitance ($\text{CPE}_{\text{TiO}_2}$) at the boundaries of the isolated TiO_2 domains and its corresponding resistance (R_{TiO_2}). Based on this fitting model, the bulk ionic conductivity (through

the LATP glass phosphate network) is 1.8×10^{-6} S/cm while the high impedance phase conductivity is 8.1×10^{-10} S/cm. The bulk conductivity is very similar to the PEALD LTP process and in agreement with amorphous LATP literature.⁹²

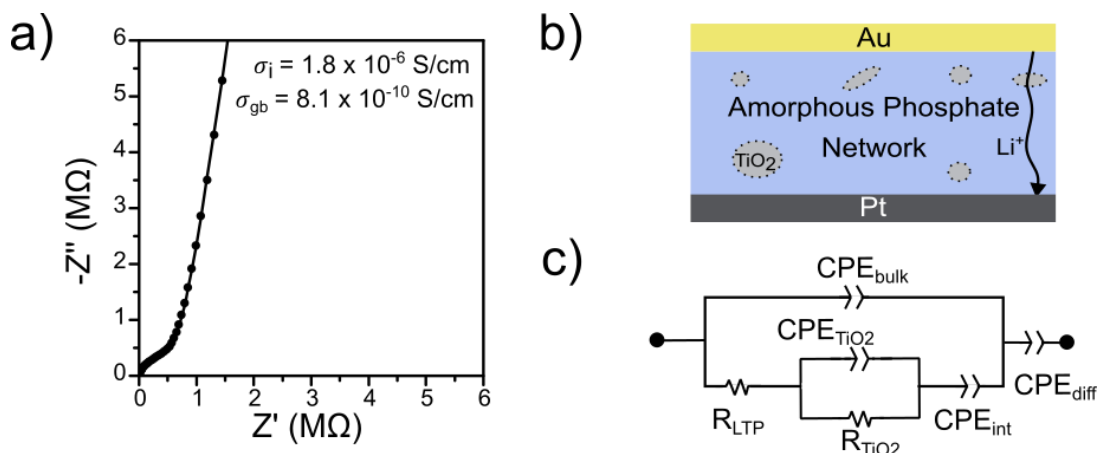


Figure 3.11. a) Nyquist plot of LATP ($n = 2$, $y = 30$) with corresponding b) physical representation of film structure and c) equivalent circuit model.

3.5. Conclusions and Future Work – Glassy ALD Metal Phosphates

This chapter explores strategies for maximizing ionic conductivity in amorphous metal phosphates and for tuning mixed ion/electron conduction in ALD thin films. The TiP_2O_7 -based metal phosphate proved to be a more ideal strategy for increasing the Li^+ conductivity compared to Li_3PO_4 -based systems. Unlike Li_3PO_4 , LTP has the advantage of already being in an amorphous state. Ti^{+4} allows for a high degree of network connectivity that promotes a Li^+ conductivity of 1.5×10^{-6} S/cm. Al-doping was done on a thermal LTP process that yielded a Li^+ conductivity of 1.8×10^{-6} S/cm despite being riddled with small TiO_2 domains. As evidenced by Al-doping of Li_3PO_4 in this work and in literature, as little as 1-3 % Al-doping can have a big impact on Li^+ conduction (~1 order of magnitude). This incentivizes a full study into the effects of Al-doping on the

amorphous LTP system with the well-connected phosphate network that can be produced with the PEALD TiP_2O_7 ALD sub-process.

In the LTP materials system, we found that intentionally introducing TiO_2 impurities in the titanium phosphate sub-process is an effective way to create an electron conducting pathway by forming a high density of TiO_2 domains within the lithium titanium phosphate glassy matrix. This is a good starting point for a mixed electronic/ionic conductor for ionic devices, but the presence of the TiO_2 domains disconnects the phosphate network and creates a high barrier for Li^+ conduction, reducing the ionic conductivity by ~ 3 orders of magnitude. In its amorphous state, TiO_2 is also a poor electronic conductor that would not make for a suitable electrode material. However, both LTP and TiO_2 can attain high conductivities in their crystalline states (NASICON and anatase/rutile, respectively). Phase engineering of this material is required to take advantage of the crystalline states of this nanocomposite as an electrode material (to be discussed in Chapters 4 and 5).

Chapter 4: Phase Engineering Strategies and Challenges of the Li-Ti-P-O Thin Film Materials System

4.1. Chapter Summary

As discussed in **Section 1.1**, development of ionic conductors by ALD has been predominantly amorphous materials. In **Chapter 3** we developed various amorphous thin films in the Li-Al-Ti-P-O materials system as a precursor to the study of their crystalline counter parts. This chapter will elaborate on the crystallization routes towards the NASICON phase in the LTP thin films developed in **Section 3.3.2**. In **Section 4.2** we discuss the process development of annealing conditions for thermal LTP films ($n = 2$ and 7). In **Section 4.3** we discuss the current progress and challenges of phase control with thin film systems as pure electrolyte materials.

4.2. Phase Engineering Towards an LTP/TiO₂ Nanocomposite Electrode Material

This section focuses on the effect of factors, like initial composition and annealing conditions, on the resulting thermal budgets and phase purity in the thermal LTP films from **Section 3.3.2**. As previously detailed, the chosen supercycle ratio (n) dictates the film composition. For the remainder of this section, we will discuss the films in terms of the relative amount of PO₄ and Li that the films contain compared to the ideal composition for the NASICON phase. This composition is designated by the horizontal line in **Figure 3.7** with an ideal PO₄/Ti ratio of 1.5. The ideal composition is approached by ALD with a supercycle ratio of $n = 2$ (corresponding to a PO₄/Ti ratio of 1.7).

Starting with the composition of a super cycle ratio of $n = 7$, **Figure 3.7** shows a Li and PO₄-deficient film relative to the predicted stoichiometry of the NASICON LTP phase. **Figure 4.1a**

shows the Raman spectrum of this film annealed at 850 °C for 10 hrs that was allowed to cool radiatively over the course of 10 hrs. This complex Raman spectrum can be deconvoluted into a variety of phases: anatase TiO₂, rutile TiO₂, brookite TiO₂, LiTiPO₅, γ -Li₃PO₄, β -Li₃PO₄, TiPO₄, and TiP₂O₇, with the peak assignments summarized in **Table 4.1**.¹¹⁰⁻¹¹⁷ Although the characteristic NASICON peaks are not present here, TiO₂ and LiTiPO₅ are common impurities in bulk NASICON LTP and LATP found in literature.¹¹⁸ The complexity of this film is owed to the extended time at elevated temperatures, which we hypothesize enables constant rearrangement of atoms that crystallize into various types of phosphates and oxides depending on the local composition. Therefore, control over the film structure can be achieved by annealing for shorter times and quenching to room temperature at the end of the annealing period.¹¹⁹

Table 4.1. Raman peak assignments for representative LTP n = 7, 2, and 1 annealed films.

| <i>Phase</i> | <i>Ref.</i> | <i>LTP (n = 7)</i> | | <i>LTP (n = 2)</i> | | |
|------------------------------------|-------------------------------------|--------------------|----------------------|--------------------|--------------------|-----------------------------------------|
| | <i>Wavenumber (cm⁻¹)</i> | <i>Ref.</i> | <i>850 °C 10 hrs</i> | <i>3hrs</i> | <i>650 °C 1 hr</i> | <i>LTP (n = 1) 850 °C 30 min center</i> |
| TiO₂ Anatase | 147 | | 147 | | | |
| | 198 | | | 195 | 198 | 193 |
| | 398 | ¹¹⁰ | | 395 | 396 | 393 |
| | 515 | | | 515 | 518 | 516 |
| | 640 | | | 636 | 637 | 637 |
| TiO₂ Rutile | 144 | ¹¹⁰ | | 142 | 143 | 142 |
| | 235 | | 233 | | | |
| | 153 | ¹¹¹ | 151 | | | |

| | | | | | |
|---------------------------------------|------|----------------|----------|------|-----------|
| TiO₂ | 214 | 213 | | | |
| Brookite | | | | | |
| LiTiPO₅ | 745 | ¹¹⁷ | 749 | | |
| NASICON | 214 | | 213 | | |
| | 239 | | | 237 | 238 238 |
| | 273 | | | 272 | 278 271 |
| | 309 | | | 308 | 310 309 |
| | 351 | | | 348 | 350 347 |
| | 432 | ¹¹² | | 431 | 430 431 |
| | 446 | | | 444 | 446 445 |
| | 970 | | | 967 | 967 966 |
| | 989 | | | 985 | 986 986 |
| | 1006 | | | 1003 | 1004 1003 |
| | 1017 | | 1011 | | |
| | 1095 | | | 1092 | 1095 |
| TiPO₄ | 173 | | | 172 | |
| | 294 | ¹¹⁶ | 290 | | |
| | 606 | | 604 | | |
| | 1047 | | 1051 | | |
| β-Li₃PO₄ | 478 | | 475, 481 | | |
| | 586 | ¹¹³ | 583 | | |
| | 622 | | 625 | | |
| | 1023 | | 1022 | | |

| | | | |
|-------------------------------------------|------|----------------|------|
| | 1063 | | 1063 |
| γ -Li ₃ PO ₄ | 426 | | 421 |
| | 607 | | 604 |
| | 631 | ¹¹³ | 625 |
| | 1023 | | 1022 |
| | 1063 | | 1063 |
| TiP ₂ O ₇ | 625 | ¹¹⁴ | 625 |

To address this, we annealed the $n = 7$ sample at 850 °C for 3 hrs and introduced a post anneal quench to room temperature. The resulting Raman spectrum (**Figure 4.1a**) has characteristic NASICON peaks in the high wavenumber region (965 – 1095 cm⁻¹) and in the lower wavenumber region (237 – 445 cm⁻¹), matching the NASICON LTP reference peaks detailed in **Table 4.1**. The remaining peaks match anatase and rutile TiO₂. This is a significant improvement in the phase purity of the film, owed to shorter exposure to high temperatures. As discussed in the **Section 3.3.1**, the base TiPO ALD process already contains a TiO₂ phase impurity from the TTIP/H₂O step.^{58,120} Having pre-formed amorphous TiO₂ can lead to preferential anatase grain growth, which is observed in both annealing conditions discussed here.

The XPS spectra of the $n = 7$ film annealed at 850 °C for 3 hrs reveals a drastic loss of P (from 9.8 to 3.4 atomic %) and Li (from 4.5 to 0 atomic %) paired with an increase in C content (from 13.6 to 24.9 atomic %) on the surface (**Figure 3.6b-f**). Before annealing, the C 1s spectra of as-deposited LTP has a peak at 288.8 eV, which lies in between lithium carbonate and titanium carbonate reported peak positions.^{58,75} After the 850 °C anneal in air, the C 1s spectra for LTP has a peak at 287.6 eV that corresponds to carbonyl groups (C=O). Since there is also no more Li

present in the surface of the LTP sample after the anneal, this suggests that most of the carbonates from the as-deposited LTP were Li_2CO_3 and were converted into organic carbonyl groups as the Li evaporated from the film.¹²¹ The O 1s peaks of the annealed LTP more closely match semi-crystalline Li_3PO_4 ,⁷⁴ with a phosphorous component peak shift to lower binding energies at 530.5 eV, suggesting a change in structure at high temperatures formed PO_4 tetrahedral units. The Ti 2p in the annealed LTP shows a shift to lower binding energies by 0.3 eV, indicating a change in chemical environment attributable to TiO_6 octahedra formation.¹²²

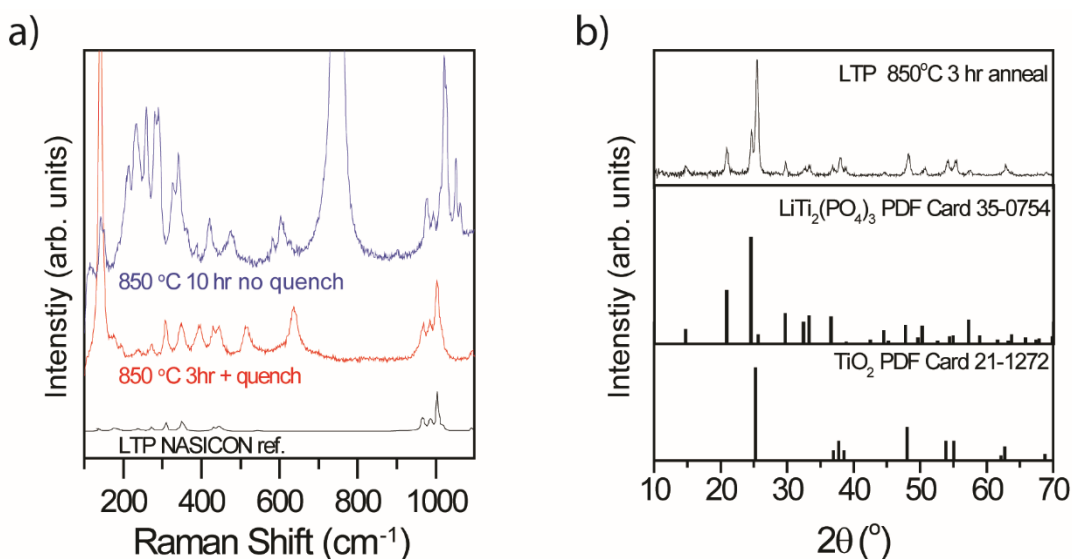


Figure 4.1. a) Raman spectra for LTP ($n = 7$) annealed at 850 °C for 10 hrs (blue) and 850 °C for 3 hrs and quenched (red). b) GI-XRD of LTP ($n = 7$) annealed at 850 °C for 3 hrs and quenched (top) with reference spectra of NASICON LTP (middle) and TiO_2 anatase (bottom).

Crystallographic characterization was performed with GI-XRD of the $n = 7$, Li and PO_4 -deficient LTP film annealed at 850 °C for 3 hrs as shown in **Figure 4.1b**. There is a match between the annealed LTP sample and characteristic NASICON LTP crystalline peaks, particularly at 14.8 °, 20.9 °, 24.5 °, 29.8 °, 32.5 °, and 33.4 ° $2(\theta)$. Although the (101) face of anatase TiO_2 overlaps with the (113) face of NASICON LTP (PDF Card 35-0754), anatase TiO_2 can be identified by three characteristic peaks at 36.9 °, 37.9 °, and 38.6 ° $2(\theta)$ (PDF Card 21-1272).

Rietveld refinement of the LTP GI-XRD spectra estimates a relative composition of 55.2 % anatase TiO₂ and 44.8 % NASICON LTP (**Figure 4.2**).

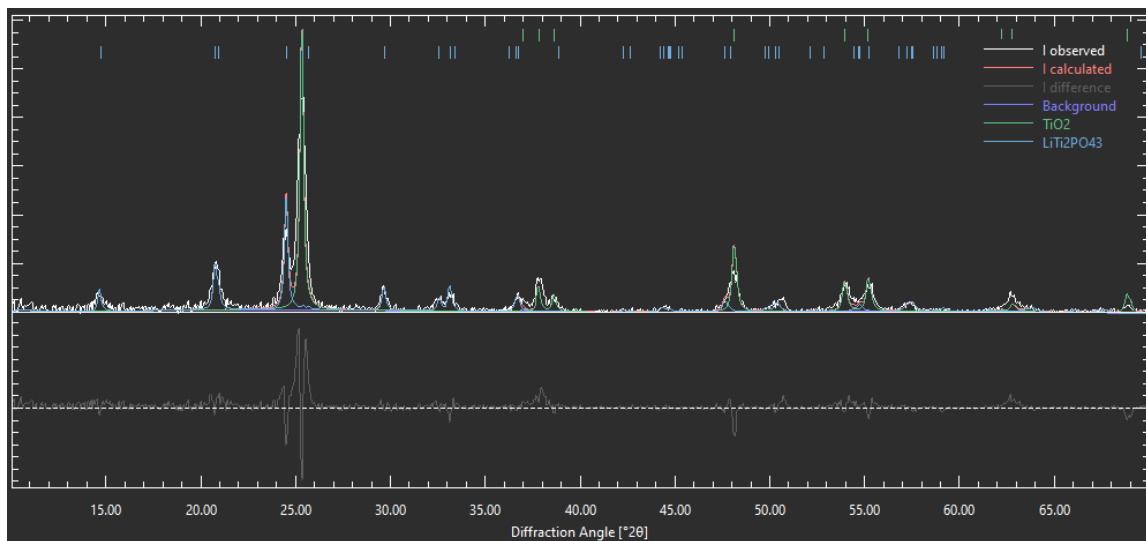


Figure 4.2. Rietveld refinement of LTP $n = 2$ annealed at 850 °C for 3 hours, which results in a chemical composition of 55.2 % TiO₂ anatase and 44.8 % LTP NASICON crystallites.

Although the NASICON phase is observed with improved annealing conditions, **Figure 4.3** demonstrates that phase inhomogeneities exist spatially across the LTP films for Li and PO₄-deficient samples. **Figure 4.3a** shows the two extreme compositions ($n = 7$ and $n = 1$) annealed at 850 °C for 30 minutes with Raman spectra taken at the center and edge of the samples. Li and PO₄-rich films ($n = 1$) show good uniformity with nearly identical spectra at the center and edge. However, in the Li and PO₄-deficient films, there is a spatial phase non-uniformity present. The center contains LiTiPO₅, anatase TiO₂, and TiPO₄. There are additional peaks in the high wavenumber region (966-1050 cm⁻¹) that are likely overlapping mixed phosphate peaks and difficult to identify. However, the edge has crystalline phase contributions of NASICON LTP, TiO₂ anatase and rutile TiO₂ only. This disparity is likely due to compositional gradients that form,

which appear to become homogeneous given enough excess Li and P in the initial film composition to compensate for Li loss at high temperatures.

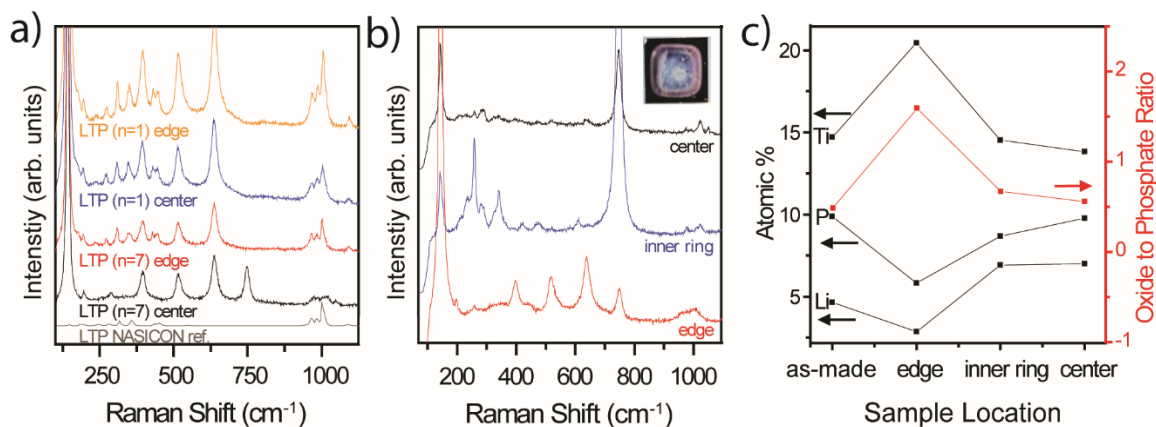


Figure 4.3. a) Raman spectra of Li and PO_4 -deficient ($n = 7$) films annealed at $850\text{ }^\circ\text{C}$ for 30 min taken at the center (black) and edge (red) compared to Li and PO_4 -rich ($n = 1$) films taken at the center (blue) and edge (orange). b) Raman spectra of Li and PO_4 -deficient ($n = 7$) films annealed at $650\text{ }^\circ\text{C}$ for 10 hrs without quenching taken at the edge (red), inner ring (blue), and center (black). c) XPS compositional analysis of the Li, Ti, and P concentrations (left axis) and the $\text{TiO}_2:\text{PO}_4$ ratio from the O 1s high resolution spectra corresponding to the same regions as (b).

To verify the existence of a compositional gradient, XPS and Raman mapping were performed on Li and PO_4 -deficient ($n = 7$) samples that were annealed at $650\text{ }^\circ\text{C}$ for 10 hrs without quenching (**Figure 4.3b**). The inset in **Figure 4.3b** of the annealed sample shows an obvious inhomogeneity within the sample with three distinct regions: the center white dot, the blue inner ring, and the purple edge. Raman and XPS spectra were taken at each of these regions. The Raman spectra (**Figure 4.3b**) show phase non-uniformity in which the edge of the sample contains NASICON LTP, LiTiPO_5 , and TiO_2 phases while the inner ring and center show dominant LiTiPO_5 peaks, with lower intensity anatase TiO_2 , brookite TiO_2 , rutile TiO_2 , TiPO_4 , $\gamma\text{-Li}_3\text{PO}_4$, and $\beta\text{-Li}_3\text{PO}_4$. The XPS map (**Figure 4.3c**) taken in the same regions displays a Li and P gradient increasing from the edge to the center while the Ti decreases in the same direction. The ratio of

oxide to phosphate in the O 1s high resolution spectra was quantified to compare to the phases observed in the Raman map. The edge of the sample has the most intense TiO₂ Raman peaks accompanied by NASICON peaks (**Figure 4.3b**). In **Figure 4.3c**, the TiO₂:PO₄ ratio decreases quickly from the edge (1.6) to the inner ring (0.7) where it stabilizes compared to the center (0.6). In the Li and P-rich regions the LiTiPO₅ phase appears dominant. Since this anneal ramps down slowly without quenching, and LiTiPO₅ crystallizes at 570 °C (~280 - 90 °C lower than NASICON LTP),¹²³ it is likely that the LiTiPO₅ phase is more readily available at lower temperatures, leaving little to no Li and P to form the NASICON phase in the center and inner ring. The annealing condition in **Figure 4.3b** follows the same pattern as the Raman spectra of the 850 °C 30 min quenched anneal in **Figure 4.3a**, in which LiTiPO₅ and TiPO₄ consume Ti at the expense of TiO₂. In instances where the dominant phosphate phase is NASICON, little to no other phosphates are observed, leading to abundant resources for TiO₂ formation.

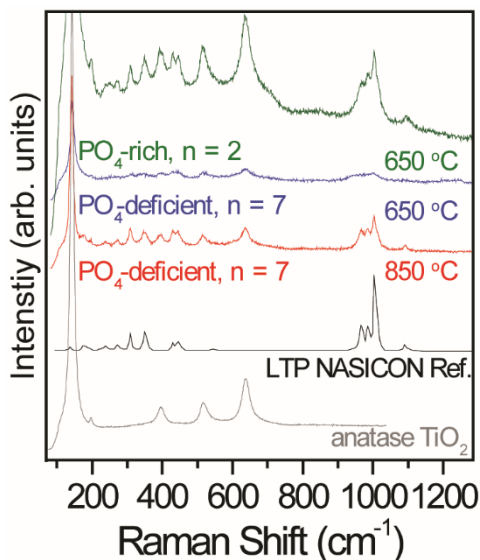


Figure 4.4. Raman spectra of Li and PO₄-rich (n = 2) and Li and PO₄-deficient LTP (n = 7) annealed at 650 °C and 850 °C for 1 hour under N₂ flow.

In addition to phase homogeneity, initial composition influences the temperature required to observe the NASICON phase. In **Figure 4.4**, Raman spectra of Li and PO₄-deficient films are compared to Li and PO₄-rich films. Peaks associated with anatase TiO₂ and rutile TiO₂ are present in all cases. The characteristic NASICON peaks are very prominent in the 850 °C annealed condition of the Li and PO₄-deficient film (n = 7). This signature is diminished when annealed at 650 °C for the same amount of time. In contrast, at an annealing temperature of only 650 °C the Li and PO₄-rich film (n = 2) shows well-defined NASICON peaks in the high wave number region with relatively high intensities. Typical synthetic methods for LTP in the bulk require high temperature processes (ranging from 800 – 1450 °C) to achieve the desired structure.⁸⁹ A reduction in crystallization temperature as much as 200 °C is achieved by starting with a Li and PO₄-rich LTP film. In this case 650 °C is required – a much lower annealing requirement than in bulk NASICON SSEs. Reduced thermal budgets is a feature of thin films that can be leveraged with ALD given the angstrom-scale thickness control it affords.

The structure of the Li and PO₄-rich films (n = 2) are studied in greater detail to elucidate a physical representation of the phase distribution that will aid in our impedance analysis in **Section 5.2**. The n = 2 samples were annealed in a rapid thermal annealer (RTA) at 650 °C for 9 min. The Raman spectra and GI-XRD of this sample in **Figure 4.5a-b** show that the NASICON and anatase peaks are retained despite the film being less crystalline with shorter annealing time. These conditions were chosen with a metal-insulator-metal (MIM) stack in mind to minimize the well-documented volume shrinking known to occur in LTP upon crystallization, such that the film remains continuous after the annealing step.^{119,124}

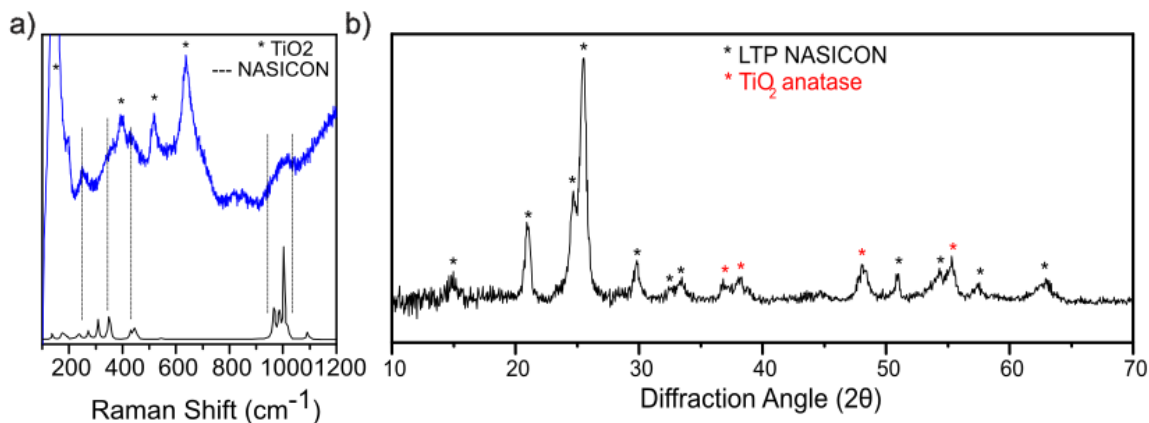


Figure 4.5. a) Raman and b) XRD of the thermal LTP n = 2 650 °C 8.5 min film

SEM cross-sectional images in **Figure 4.6a-d** show the morphological improvement on the annealed LTP film from 850 °C for 3 hrs to 650 °C for 9 min suitable for an MIM stack. The planar view in **Figure 4.6b** shows individual grains with sections that are out of focus. This agrees with the overall picture from Raman and XRD that it is a semicrystalline film. The cross-sectional SEM in **Figure 4.6a** of this sample shows a film of 60 nm thickness in good contact with the Pt and Au blocking electrodes with a textured structure. The 850 °C annealed samples **Figure 4.6c-d** show dramatic morphological deformations, likely due to volume changes that come with the phase transition to the NASICON phase leading to strain between the film and the substrate.⁹²

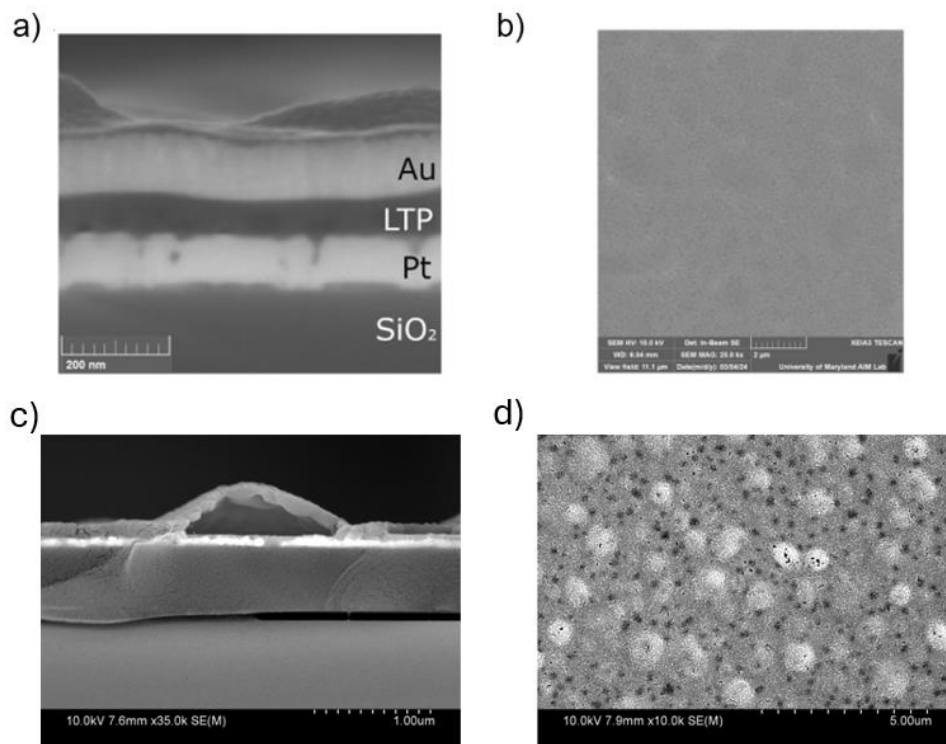


Figure 4.6. Planar and cross-sectional SEM images of thermal LTP annealed under different conditions. a) thermal LTP (n = 2) annealed at 650 °C 8.5 minutes cross sectional SEM view. b) thermal LTP (n = 2) annealed at 650 °C 8.5 minutes planar SEM view. c) thermal LTP (n = 7) annealed at 850 °C 3 hours cross sectional SEM view. d) thermal LTP (n = 7) annealed at 850 °C 3 hours planar SEM view.

Raman and GI-XRD of this material indicates that it is a semicrystalline film with a mixture of anatase TiO_2 and NASICON LTP grains with an average size of 29.0 nm and 44.1 nm, respectively (Scherrer analysis included in **Table 4.7**). High-resolution transmission electron microscopy (HRTEM) confirmed a large variation in particle size, with particles of both anatase TiO_2 and NASICON LTP ranging from $\sim 5 - 40$ nm in an amorphous matrix. No individual particles with sizes near the film thickness were observed. Particles were identified as anatase TiO_2 or NASICON LTP by comparing d-spacings observed in XRD to those observed in HRTEM and selected area electron diffraction (SAED). **Figure 4.8a-b** shows representative HRTEM and corresponding SAED patterns for isolated NASICON LTP and TiO_2 particles.

| NASICON peaks | | | | |
|-----------------------------|--------------|------|--------------------|---------------|
| peak position (2 θ) | Miller Index | FWHM | Particle Size (nm) | d spacing (Å) |
| 14.98 | 012 | 0.87 | 68.8 | 5.91 |
| 21.00 | 104 | 0.55 | 78.0 | 4.23 |
| 24.65 | 113 | 0.73 | 50.3 | 3.61 |
| 25.52 | 202 | 0.62 | 56.9 | 3.49 |
| 29.79 | 024 | 0.66 | 45.6 | 3.00 |
| 32.67 | 211 | 0.50 | 55.6 | 2.74 |
| 33.49 | 116 | 0.79 | 34.0 | 2.67 |
| 44.69 | 223 | 0.80 | 25.2 | 2.03 |
| 50.71 | 042 | 0.42 | 41.8 | 1.80 |
| 57.41 | 410 | 0.84 | 18.6 | 1.60 |
| 62.95 | 327 | 1.34 | 10.7 | 1.47 |
| Anatase peaks | | | | |
| peak position (2 θ) | Miller Index | FWHM | Particle Size (nm) | d spacing (Å) |
| 36.87 | 103 | 0.66 | 37.1 | 2.44 |
| 38.20 | 112 | 1.16 | 20.4 | 2.35 |
| 48.20 | 200 | 0.94 | 19.9 | 1.89 |
| 55.20 | 211 | 0.52 | 31.5 | 1.66 |

Table 4.7. Table of Scherrer analysis on the XRD spectrum of LTP n = 2 annealed at 650 °C for 9 minutes. Particle size was determined by the FWHM and position of the peaks according to the equation $D = \frac{K\lambda}{\beta \cos(\theta)}$ where D is the crystallite diameter, K is the shape factor, β is the FWHM, λ is the X-ray wavelength, and θ is the Bragg angle. The LTP and TiO₂ grains are assumed to be spherical, so a shape factor of 0.89 was chosen.

The HRTEM cross section of the LTP film in **Figure 4.8c** shows contrast from both crystalline and amorphous regions. The LTP and TiO₂ particles appear to be uniformly distributed in an amorphous matrix in the film. Based on their estimated weight percentage and particle size, it is plausible for there to be a continuous pathway of TiO₂ grains throughout the 60 nm thickness of the film. A schematic of the system for the Li and PO₄-rich (n = 2) film is proposed in **Figure 4.8d** based on the evidence shown in **Figures 4.1-4.5 and 4.8**. Due to the complexity of the system created by annealing a 5-component ALD film, a specific composition cannot be assigned to the amorphous region. This physical representation of the system is used in **Section 5.2** to develop an equivalent circuit model for the EIS results.⁹⁹

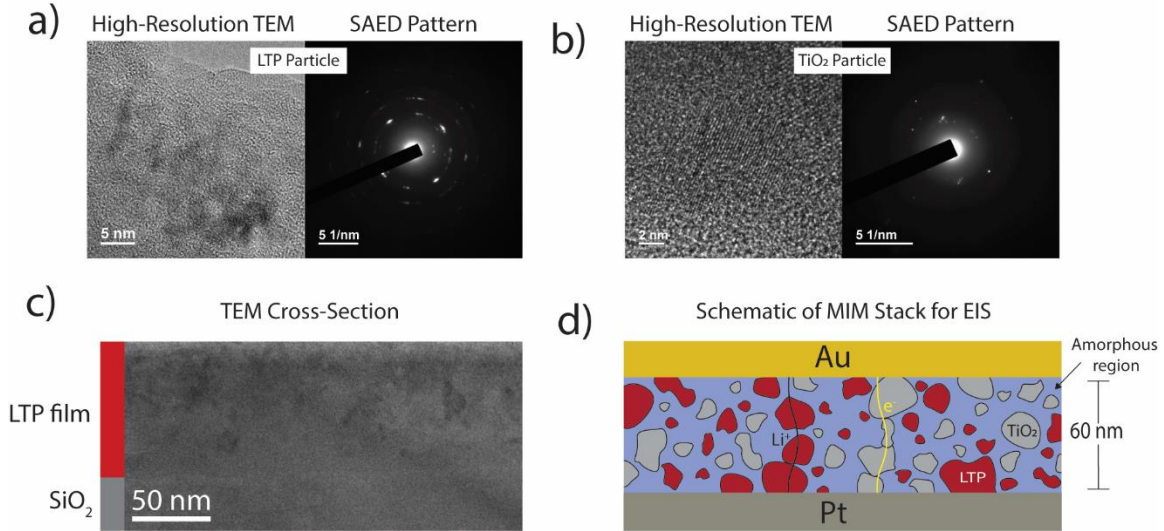


Figure 4.8. Annealed LTP ($n = 2$) ($650\text{ }^{\circ}\text{C}$ for 9 min) cross section. High-resolution TEM and corresponding SAED pattern for a) an LTP particle and b) a TiO_2 particle. c) TEM cross-section of the annealed LTP. d) Schematic cross-section of the annealed LTP film in an MIM stack configuration based on TEM and crystallographic evidence.

4.3. Challenges and Future Considerations with Phase Engineering Towards a NASICON ALD

Electrolyte

In the case of the NASICON thin film as an electrolyte, the purity requirements are more stringent requiring no electron-conducting sub-phases in the film. In this section we discuss the annealing conditions studied to work towards a NASICON ALD thin film electrolyte. Ultimately this is challenging due to thermal requirements for phase purity and substrate compatibility considerations. Initial results of annealing the PEALD LTP film (**Section 4.3.1**) will be discussed. The parameter space for controlling the crystallization in LTP and LATP is quite large and was therefore not fully developed within the time constraints of this dissertation. However, the following sections serve as a starting point towards understanding some critical factors and discuss how to address the challenges faced in future work.

4.3.1. Crystallization Behavior of Plasma Enhanced LTP Electrolyte

The PEALD LTP ($n = 2$) film was annealed under various conditions with the goal of crystallizing the amorphous phosphate into the NASION-type phase with minimal TiO_2 impurities such that the film can remain electronically insulating. **Figure 4.9** shows the Raman spectra of the various annealing temperatures performed on PEALD LTP films. In all cases, the films were quenched to room temperature to retain the phases stable at high temperatures.

The as-deposited film in **Figure 4.9a** is completely featureless in the Raman spectra, indicating that it is amorphous (as was assumed for the Nyquist plot fitting in **Section 3.4**). At $650\text{ }^\circ\text{C}$ for 9 minutes (**Figure 4.9b**) the Raman spectra has dominant TiO_2 anatase peaks at 142, 398, 517, and 637 cm^{-1} and a peak at 746 cm^{-1} corresponding to LiTiPO_5 . Some small peaks emerge in the high wavenumber region at 946 and 1024 cm^{-1} but a specific phase is difficult to identify without additional information. An increase in temperature to $850\text{ }^\circ\text{C}$ for 9 minutes (**Figure 4.9c**) still shows retention of the TiO_2 anatase and LiTiPO_5 phases, though additional peaks emerge in the high and low wavenumber regions of the spectrum. The peaks at 951, 974, 1024, 1050, and 1113 cm^{-1} correspond to $\gamma\text{-Li}_3\text{PO}_4$ and 198, 257, 289, and 322 cm^{-1} correspond to TiP_2O_7 . The presence of the $\gamma\text{-Li}_3\text{PO}_4$ crystalline system is corroborated by the overall loss of order in **Figure 4.9d-e** where the film was held at $850\text{ }^\circ\text{C}$ for 40 minutes and $950\text{ }^\circ\text{C}$ for 30 minutes. $\gamma\text{-Li}_3\text{PO}_4$ transitions into the less ordered $\alpha\text{-Li}_3\text{PO}_4$ phase with increasing time and temperature,¹¹³ indicated by the peaks that emerge at 444 and 610 cm^{-1} in **Figure 4.9c** that grow in intensity at $950\text{ }^\circ\text{C}$ (**Figure 4.9e**). As the $\alpha\text{-Li}_3\text{PO}_4$ phase becomes dominant, the TiP_2O_7 features broaden due to induced bulk disorder throughout the film from the lithium phosphate phase transition.

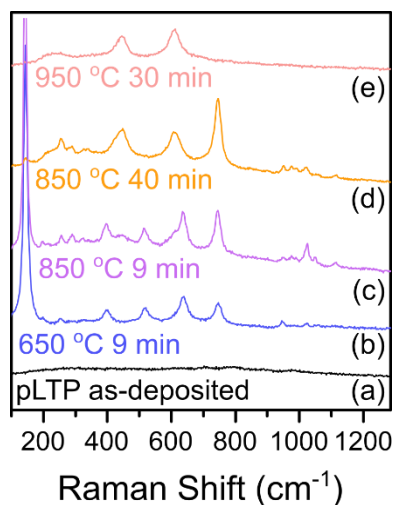


Figure 4.9. Raman spectra of as-deposited (black) and annealed PEALD LTP ($n = 2$) films at 650 °C 9 minutes (blue), 850 °C 9 minutes (purple), 850 °C 40 minutes (orange), and 950 °C 30 minutes (red).

Though the NASICON LTP phase is not present under these annealing conditions, the TiO_2 anatase phase is nearly gone at 850 °C for 9 minutes with only a small peak at 144 cm^{-1} and not detectable when held at the same temperature for 40 minutes. TiO_2 grains still nucleate first at lower temperatures even though the as-deposited PEALD LTP starts out with minimal oxide bonding compared to the thermal process. The TiO_2 grains are fully consumed in favor of LiTiPO_5 at higher temperatures (as seen in **Figure 4.9d**). This indicates that the volume fraction of TiO_2 anatase nucleated at 650 °C may be smaller in the PEALD LTP film due to the nature of the phosphate network structure (which agrees with compositional analysis in **Section 3.3.1** of the as-deposited films).

Unlike the thermal process, the PEALD LTP crystallization process appears to have segregated Li-rich and Li-deficient regions that allow the growth of $\gamma\text{-Li}_3\text{PO}_4$ and TiP_2O_7 grains as opposed to NASICON $\text{LiTi}_2(\text{PO}_4)_3$. The PEALD LTP ($n = 2$) film has an initial composition of $\text{Li}_{2.4}\text{Ti}_2(\text{PO}_4)_3\text{O}_{3.3}\text{C}_{1.6}$ with only 6.5 % more lithium than is required for the NASICON structure.

Due to the reported loss of lithium during high temperature anneals (**Section 4.2** in this work and in literature¹²⁵), homogeneity in the film can be improved by increasing the amount of lithium content with ALD processing. Within the time constraints of this work, a compositional study was not completed but various routes to increasing Li retention in the film can be explored in the future. For example, a super-cycle ratio to $n = 1$ could allow for sufficient lithium concentration in the film after annealing but may also alter the relative amount of phosphate in the film as was seen in **Section 3.3.2** in thermal LTP development. Alternatively, the film can be annealed in the presence of Li_2O powder as a lithium source to compensate for the lithium loss that is observed here without introducing excess phosphate into the network – which may be contributing to the Li_3PO_4 crystallization route as well.^{92,125} Compositional studies should be done at the different annealing temperatures to determine if a lack of lithium or excess phosphate is contributing to complex phase distributions at high temperatures.

4.3.2. Considerations and Future Work for Crystalline NASICON and ALD Thin Film Electrolytes

Of course, the annealing conditions shown here are not exhaustive and there is more to learn about the crystallization route to the NASICON phase starting from this well-connected LTP phosphate network. Not all glass networks are created equal though they are difficult to characterize when amorphous (as evidenced by the nearly identical composition of the thermal and PEALD LTP processes that behave quite differently electronically and in crystallization routes). The number of degrees of freedom when considering experimental design make this a challenging system. Never the less, it has been well-documented in this work, and in literature,^{92,118} that composition and network structure are major players when determining the crystallization mechanism. Therefore, this field would benefit from further work systematically controlling

composition and network structure with changes in ALD process parameters to elucidate a better understanding of the crystallization mechanism in this complicated thin film system.

Other factors that have not been considered here but have been reported to affect crystallization of the NASICON phase in thin films are choice of substrate, varied ramp rates, and staged annealing strategies.⁹² The route to NASICON with ALD films should be studied in more detail in the Li-Ti-P-O materials system before introducing additional complexities like Al-doping that may introduce yet more opportunities for impurities and increased thermal budgets.¹²⁶

Chapter 5: Electrochemical Behavior of LTP/TiO₂ Nanocomposite Electrode

5.1. Chapter Summary

In **Section 4.2** a mixed ionic/electronic conducting nanocomposite was developed by tuning ALD process parameters and annealing conditions to select for the anatase electron conducting phase and the NASICON ionic conducting phase. In **Section 5.2** we study the ionic and electronic conduction of this nanocomposite with electrochemical impedance spectroscopy. Lastly, in **Section 5.3** we will demonstrate the electrochemical behavior of this ALD nanocomposite as a proof of concept in a half cell configuration vs lithium metal. The results in this chapter are an indication that this is a promising material system to continue to optimize and study for high rate and high capacity iontronics applications.

5.2. Deconvolutions of Electrical Behavior in LTP Semicrystalline Nanocomposite Thin Film

The Li and PO₄-rich (n = 2) LTP thin films from **Figure 4.8** were studied electrochemically in a MIM stack of Pt/LTP/Au due to the low crystallization temperature required to observe the desired phases. Based on the Schematic in **Figure 4.8d**, we must consider the effects of the high percentage of TiO₂ on the electronic properties of this film. TiO₂ is a mixed conductor with an electronic conductivity ranging from 10⁻⁷-10⁻⁵ S/cm¹⁰⁴ and has been known to serve as an anode material in LIBs.¹²⁷ Due to the significant TiO₂ impurity present upon annealing, we expect there to be both an electronic leakage pathway through the TiO₂ grains and a Li⁺ ion conduction pathway through the LTP grains. Both possible conduction pathways exist in parallel in this semicrystalline film and must be considered in the impedance analysis. The LTP bulk and amorphous components of the film will be constructed in series to represent the Li⁺ ion conduction path in the semicrystalline film.

The mobile species are represented in the equivalent circuit model in **Figure 5.1a** (based on the schematic in **Figure 4.8d**) which was used to fit the Nyquist plots. In this equivalent circuit model, constant phase elements (CPEs) are used to represent imperfect capacitances in the material. CPE_{gb} , $CPE_{interface}$, and CPE_{bulk} represent capacities at the grain boundaries, the film/metal interface, and the bulk of the film, respectively. R_{TiO_2} represents the electronic conduction through TiO_2 grains. R_{LTP} and R_{gb} represent Li^+ ion conduction through the LTP grains and the grain boundaries, respectively.

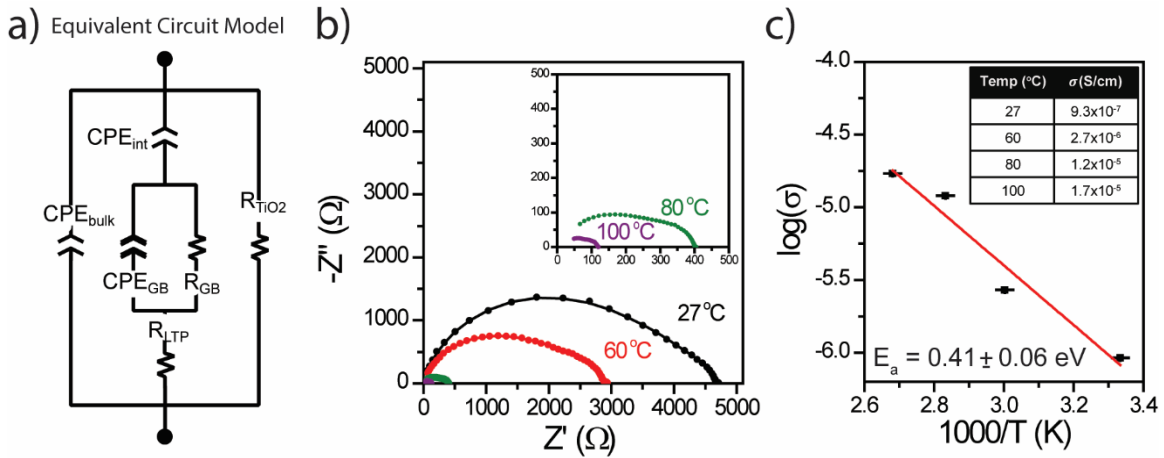


Figure 5.1. Electrochemical data for LTP ($n = 2$) MIM stack annealed at 650 °C for 9 min in the RTA. a) The equivalent circuit model used to fit the EIS data for the Au/LTP/Pt stack. b) Nyquist plots of Au/LTP/Pt probed at 27, 60, 80, and 100 °C. c) Arrhenius plot of LTP with the respective ionic conductivities at each temperature.

The room temperature Nyquist plot in **Figure 5.1b** shows an asymmetric semicircle that approaches the real axis at the low frequency limit. This indicates an electronic leakage pathway consistent with the density of TiO_2 impurities measured by GI-XRD, Raman spectroscopy, and HRTEM. The equivalent circuit model fitting results in a TiO_2 electronic conductivity of 2.5×10^{-7} S/cm, very close to the total film electronic conductivity measured by DC relaxation experiments of 8.5×10^{-8} S/cm (shown in **Figure 5.2**). This result, in conjunction with the TiO_2 peak positions

in the Raman and XRD in **Figure 4.1b** indicate, that the anatase TiO₂ present in the film is not lithiated after annealing.^{115,128}

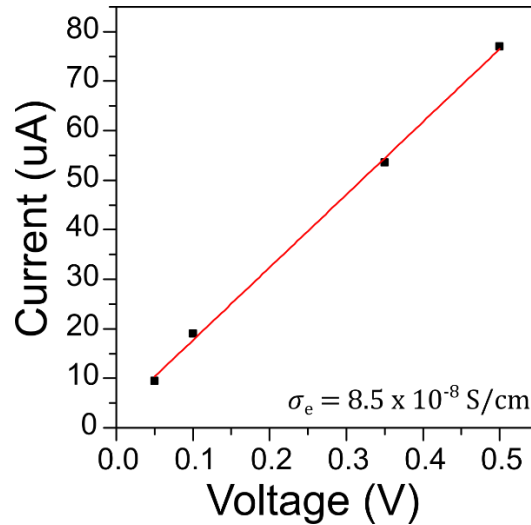


Figure 5.2. DC relaxation measurements of as-deposited LTP n = 2 film annealed at 650 °C for 8.5 minutes. The electronic conductivity is extracted from the slope of the applied voltage vs current response curve.

The LTP bulk conductivity, extracted from R_{LTP} in **Figure 5.1a-b**, is 9.3×10^{-7} S/cm room temperature (6.2x greater than the competing ALD LiPON SSE) and 1.2×10^{-5} S/cm at 80 °C. The grain boundary conductivity, extracted from R_{GB} in **Figure 5.1a-b**, is 5.6×10^{-9} S/cm at room temperature, giving a total ionic conductivity of the nanocomposite thin film of 4.7×10^{-7} S/cm at room temperature. These results agree with literature, reporting the total ionic conductivity of LTP between 10^{-8} to 10^{-6} S/cm due to variations in the grain boundary composition and overall porosity of the SSE.¹⁰⁵

The sample temperature was adjusted *in situ* to produce the rest of the EIS data shown in the Nyquist traces in **Figure 5.1b** and the Arrhenius plot in **Figure 5.1c**. The Nyquist plots show a reduction in overall impedance of the film at elevated temperatures, as well as a slight change in the ratio between the two semi-circle elements. The latter implies two different activation energies

for the transport they represent (see **Figure 5.3**). The Arrhenius plot shows a linear relationship between the log of ionic conductivity calculated from R_{LTP} and temperature – indicating an ion hopping mechanism in the LTP grains.¹²⁹ The LTP bulk has an activation energy of 0.41 ± 0.06 eV, which closely matches literature for a semicrystalline NASICON film.⁹²

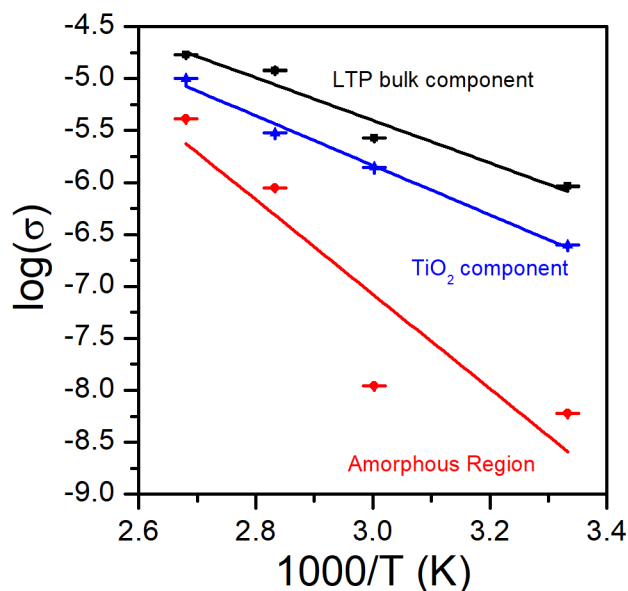


Figure 5.3. Arrhenius plot of the LTP $n = 2$ bulk component, the TiO_2 component, and the amorphous region component gathered from fitting the EIS data with the equivalent circuit model in Figure 5a in the manuscript. The activation energies of each component are 0.41 eV, 0.47 eV, and 0.90 eV, respectively.

The solid-state impedance measurements in this chapter show that the ALD nanocomposite composed of NASICON LTP and anatase TiO_2 grains have the mixed ionic-electronic conduction properties required for an electrode material, with ionic and electronic conductivities closely matched. The next chapters will demonstrate the electrochemical properties of the ALD nanocomposite as an electrode material (**Section 5.2**) and discuss future directions to take in developing fast-ion conducting ALD films for microelectronics (**Section 6.1-6.3**).

5.3. LTP Nanocomposite as a High-Rate Electrode Material

The following section highlights the electrochemical behavior of the thermal LTP ($n = 2$) nanocomposite electrode by studying it in a two-electrode half-cell configuration with the LTP/TiO₂ ALD film as the working electrode, Li metal as the counter and reference electrode, both dipped in a liquid electrolyte (1M LiClO₄ in polycarbonate). Recall, from **Sections 5.1** and **4.2**, that the nanocomposite contains anatase TiO₂ grains that provide a source of electronic conduction within the film and NASICON LTP grains that provide a source of ionic conduction within the film. Both crystalline phases are embedded in an amorphous phosphate that provides good contact between grains and is an additional source of ionic conduction. Cyclic voltammetry was performed to study the redox reactions and electrochemical stability of these subphases in two different voltage windows. Gravimetric voltammetry was performed to study the rate retention of the phases present in the nanocomposite at fast charging rates.

The nanocomposite was first cycled from 1.2 – 3.5 V vs Li/Li⁺ (**Figure 5.4**) which includes the regions where both the NASICON LTP and anatase TiO₂ crystalline phases are redox active.^{39,46,130} The high degree of electrochemical reversibility in this potential window indicates intimate contact between the anatase and NASICON grains aided by the amorphous matrix. The cycled film shows a predominant Li insertion peak at 1.7 V vs Li/Li⁺ and extraction peak at 1.95 V vs Li/Li⁺ that correspond to lithiation/delithiation of anatase TiO₂.¹³⁰ There is a small redox pair at 1.42 and 1.65 V vs Li/Li⁺ that matches redox activity of rutile TiO₂,¹³¹ indicating a small impurity present that is difficult to assign with the Raman or XRD in **Section 4.2** due to the low degree of crystallinity. The anatase redox pair has a relatively low peak separation of 240 mV (compared to 650 mV peak separations reported in micron-scale anatase particle electrodes).¹³² Anatase redox peak separation is known to decrease with increased surface area – which helps

improve kinetics of Li-insertion/extraction. For example, Attia et. al. saw a peak separation of 380 mV with particle sizes of 30-60 nm (whereas those of this work range from 5-40 nm as shown by TEM in Figure 4.8c).

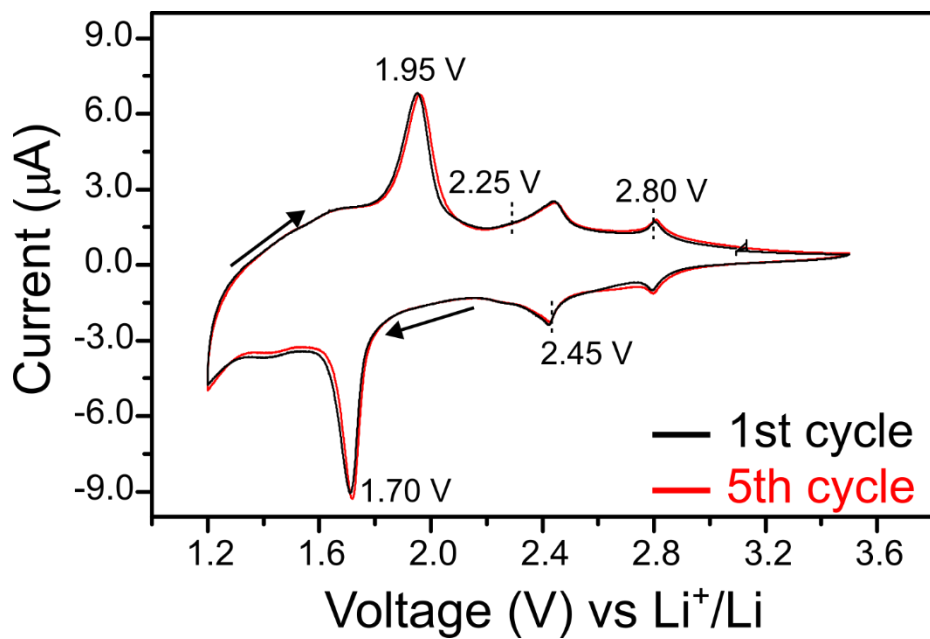


Figure 5.4. Cyclic voltammetry of LTP ($n = 2$) annealed at 650 °C for 8.5 min as the working electrode in a beaker cell with lithium metal as the counter and reference electrodes, cycled at 0.2 mV/s between 1.2 – 3.5 V vs Li⁺/Li.

At higher voltages there are three redox pairs that have been observed in literature of bulk NASICON electrodes. The strongest redox pair is centered at 2.45 V vs Li⁺/Li and corresponds to lithium insertion into the NASICON structure.^{44,46,49,50,133} In the literature, using more traditional synthesis methods such as solid state reaction with particle grinding, this is the only redox peak indicating a two-phase lithium insertion reaction in the NASICON structure.^{44,50} However, in this work there is a reversible redox pair centered at 2.8 V vs Li⁺/Li that has been observed in the literature as a shoulder of the 2.45 V pair, though only in works with sub-micron particle sizes to our knowledge.^{46,49,133,134} Assignment of this peak is challenging without more information about

the site of Li insertion at the 2.8 V reaction potential. It is feasible to imagine that in electrodes where the NASICON grains approach the nanoscale, the energy landscape is altered by local stresses and interfacial energy that may have a larger effect on the available path for lithium insertion into the lattice.⁴⁹ Such nanosizing effects have been known to alter phase transitions in cathode materials like V₂O₅ upon lithiation.¹³⁵ A more detailed study on the lithium insertion mechanism is required to understand the nature of the 2.8 V redox pair.

The nanocomposite film was then cycled from 0.25 – 3.5 V vs Li/Li⁺ as shown in **Figure 5.5a**. In the first lithiation cycle down to 0.25 V, the reduction peaks are present at 2.8 V and 2.45 V vs Li⁺/Li as expected for the lithiation of the NASICON grains. However, in subsequent cycles the NASICON redox peaks broaden and eventually disappear. This behavior has been observed in bulk NASICON electrode systems in which cycling below 1 V vs Li⁺/Li leads to irreversible vitrification of the NASICON phase.^{43,46} This structural change demonstrated in the Raman spectra in **Figure 5.5b** of a sample that was cycled between 0.25 – 3.5 V and removed from the cell at 3.5 V. Post-cycling, the NASICON region flattens out and a few broad features emerge at 711 and 855 cm⁻¹ that indicate the formation of low crystallinity phases after repeated exposure to low potentials (down to 0.25 V vs Li⁺/Li).

The first cycle has a strong peak at 0.5 V vs Li⁺/Li due to SEI formation caused by the degradation of 1 M LiClO₄ in PC electrolyte on the lithium metal surface that does not repeat in following cycles.¹³⁶ The reversible redox pair centered at 0.85 V vs Li⁺/Li in subsequent cycles suggests a new stable redox active phase has formed as a result of the structural change that occurred in the first reduction half-cycle. Due to the semicrystalline nature of this nanocomposite, the loss of the NASICON grains has little effect on the overall electrochemical reversibility of the film at this potential window. Despite the loss of the NASICON phase, there is still a significant

contribution to the overall capacity coming from the anatase grains, the newly formed phase, and pseudocapacitance from the amorphous matrix totaling a stable capacity of 1520 mAh/g. In contrast, Wang et al. showed fast decay in capacity in this voltage window of a carbon coated highly crystalline NASICON LTP electrode.⁴³

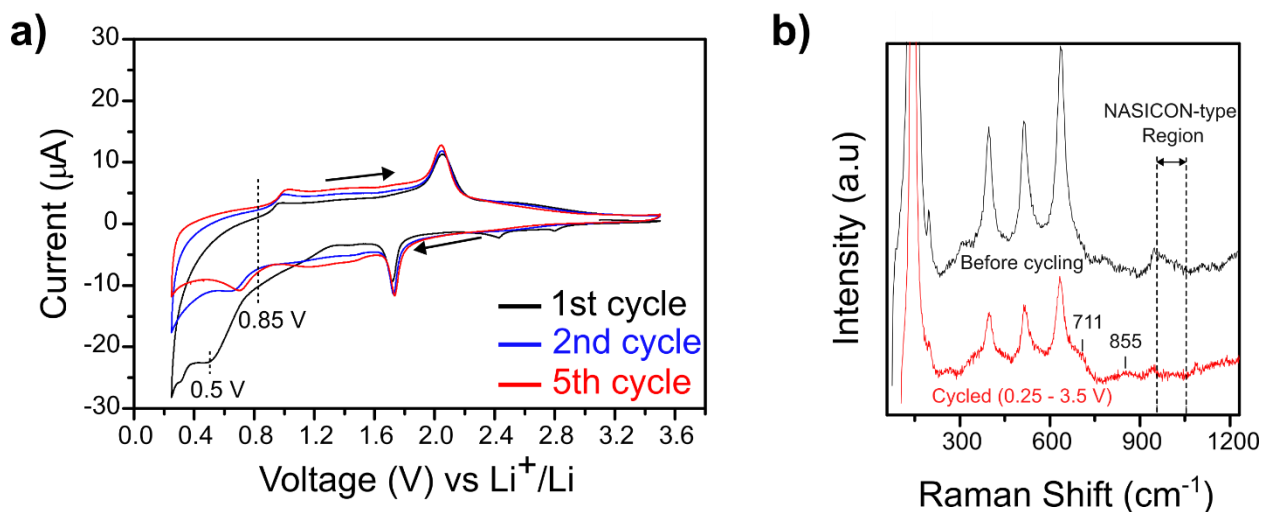


Figure 5.5. LTP ($n = 2$) annealed at 650 C for 8.5 min a) cycled in a beaker cell with lithium metal as the counter and reference electrodes, cycled at 0.2 mV/s between 1.2 – 3.5 V vs Li+/Li. b) Raman spectra of the uncycled film (black) and cycled film taken out at 3.5 V vs Li/Li+ (red).

Figure 5.6a shows gravimetric voltammetry of the nanocomposite cycled in the region where both the NASICON and anatase phase are redox active (1.6 – 3.5 V vs Li/Li+). The plateaus in the charge and discharge match the redox peaks present in the cyclic voltammogram in **Figure 5.4** and show a total capacity of 328 mAh/g within this voltage window. Deconvolution of capacity contributions of a semi-crystalline nanocomposite thin film can be quite tricky due to the number of contributors to the total capacity. The plateaus indicate the portion of the capacity that stored in the crystalline phases. However, the charge and discharge traces develop a slope as the system approaches lower voltages, indicating a pseudocapacitive contribution. Pseudocapacitive behavior is likely due in part to the amorphous phosphate matrix that surrounds the crystalline grains.¹³⁷

Since this is a thin film, electric double layer formation at the nanocomposite/electrolyte interface may also be contributing a non-negligible capacitance that is indistinguishable from that of the amorphous matrix. **Figure 5.6b** shows the capacity of the nanocomposite cycled at 1 C remains stable for over 160 cycles.

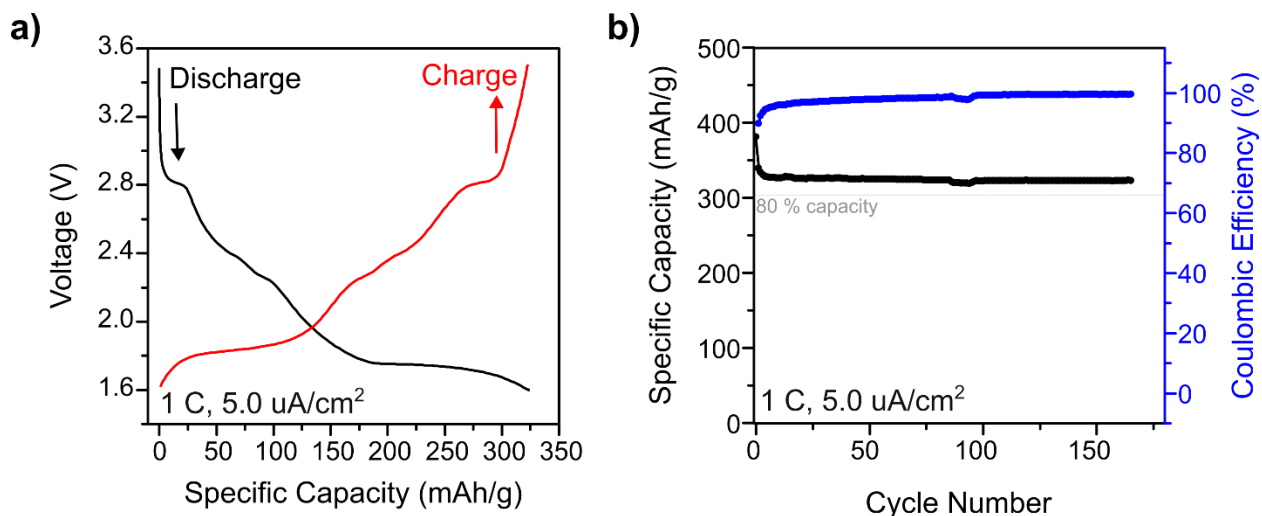


Figure 5.6. a) gravimetric voltammetry charge and discharge and b) capacity retention over 140 cycles of thermal LTP ($n = 2$) annealed at 650 °C for 8.5 minutes in a beaker cell vs Li⁺/Li cycled between 1.2 – 3.5 V at a rate of 1 C (5 uA/cm²).

Figure 5.7a shows the rate-retention behavior of the nanocomposite cycled in the NASICON and anatase active region (1.6 – 3.5 V vs Li/Li⁺) between 1 and 20 C for 10 cycles at each current density. The capacity gradually decreases with an increasing C-rate, however at a C-rate as high as 20 C the nanocomposite retains 71 % of its initial capacity. The capacity then fully recovers to 328 mAh/g after returning to a C-rate of 1 C. This thin film electrode shows very good reversibility and fast kinetics, even at high charging/discharging rates. **Figure 5.7b** shows the discharge curves at 1, 10, and 20 C for the same voltage window to identify the source of capacity loss at fast discharging rates. It is evident that anatase is responsible for most of the capacity loss at 20 C as seen by the plateau at 1.7 V vs Li⁺/Li losing 43 mAh/g at 20 C compared to 1 C. An

additional capacity loss of 15 mAh/g is observed from the sloping region between 1.7 – 2.4 V vs Li+/Li attributed to the pseudocapacitance contribution from the amorphous matrix.

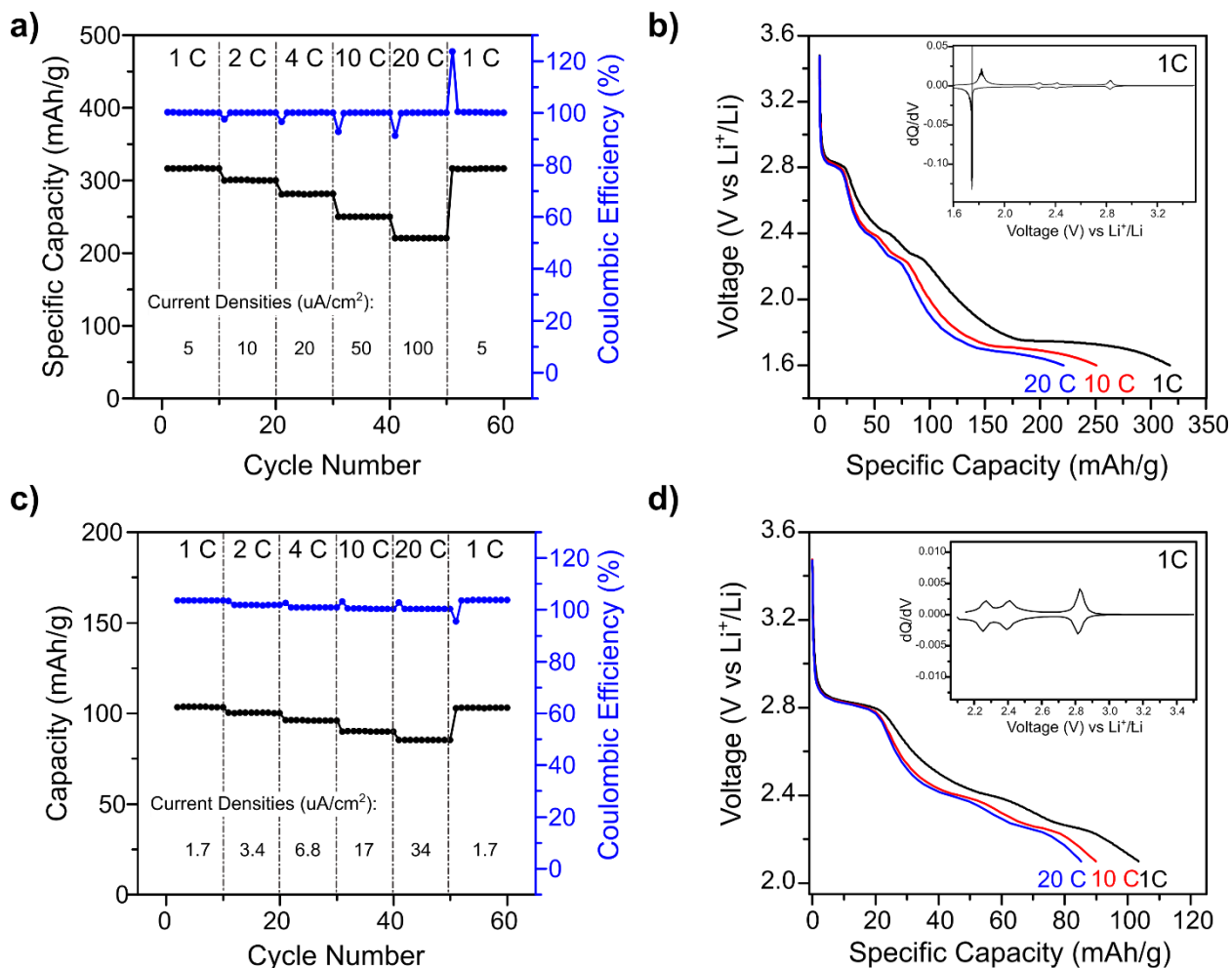


Figure 5.7. Rate retention results for thermal LTP ($n = 2$) annealed at 650 °C for 8.5 minutes cycled in a beaker cell vs lithium metal in 1M LiClO₄ in PC liquid electrolyte between 1.2 – 3.5 V (a,b) and 2.1 – 3.5 V (c,d) at charging rates of 1C, 2C, 4C, 10C, and 20 C.

The kinetics of the nanocomposite were further studied by replicating the rate retention test in the region where only NASICON grains are redox active (2.1 – 3.5 V vs Li/Li⁺), shown in **Figure 5.7d-c**. In this range the capacity at 1 C drops to 103 mAh/g due to a combination of ions stored in the NASICON crystalline grains and in the pseudocapacitive component. However, the

nanocomposite retains 82.5 % of its capacity at a cycling rate of 20 C in this voltage window. A similar analysis of the discharge curves at 1, 10, and 20 C shows that the bulk of the capacity loss between 2.1-3.5 V vs Li⁺/Li is due to the pseudocapacitance (i.e., lithium insertion into the amorphous phosphate matrix).

Whether it's between 2.1 – 3.5 V (NASICON only is redox active) or between 1.6 – 3.5V (NASICON and TiO₂ are both redox active), this thin film nanocomposite has high capacity retention at fast cycling rates. A combination of the high mobility crystalline phases present as well as the nano-scaling of both the film and the grains facilitate lithium insertion/extraction into the various components of the nanocomposite. As discussed in **Section 1.1**, working in the nanoscale naturally increases high-rate capacity retention and power delivery due to the short diffusion paths travelled in the device. But in addition to that, the high surface area provided by the nano-scale redox active grains in the nanocomposite increases the number of sites available for redox activity of each crystalline phase.

This work demonstrates the first instance of the NASICON phase utilized as an ALD thin film electrode material and can serve as a springboard to make further improvements in its electrochemical behavior for high power applications. For example, in the NASICON-only voltage window (2.1-3.5 V vs Li⁺/Li) the ratio of the film that contains NASICON grains as opposed to amorphous matrix should increase so that the high mobility phase is dominant in the nanocomposite. Such a change in film morphology can be achieved by increasing the annealing time and temperature or utilizing more PO₄⁻ and Li⁻ rich compositions (i.e, n = 1 supercycling ratio) to facilitate NASICON phase formation. However, there are tradeoffs that come with increasing the NASICON grain partial fraction. The challenges of process development for a high density phase in a thin film are discussed in **Section 4.2-4.3** that showed how drastic increases in

density leads to pinhole formation and delamination of the film from the substrate. To increase the relative portion of NASICON grains, there must still exist a critical fraction of amorphous matrix that maintains a continuous film with intimate contact at the film/substrate interface.

Chapter 6: Conclusions and Future Work

6.1. The Amorphous Route to Fast-Ion Conductors

From a manufacturing standpoint, SSEs and electrodes with low processing temperatures will always be preferred for maximum compatibility with existing industrial processes and commercially developed materials. This alone makes the amorphous route to increased ionic conductivity of ALD films an attractive avenue. The limits of ALD Li-ion conductors were pushed in this work by turning to titanium phosphate-based systems (LTP and LATP) as amorphous Li-ion conductors achieving an ionic conductivity of $1.5\text{-}1.8 \times 10^{-6}$ S/cm. In the LTP system, Al-doping did not have a large effect on the ionic conductivity, likely owed to the already well-connected nature of the phosphate network in the PEALD LTP process. However, only a thermal LATP process was attempted in this work – a process that otherwise contains large TiO_2 domains before introducing aluminum. It is unclear if Al-doping in the PEALD process would further improve the ionic conductivity due to network modifications or if the PEALD LTP process has already reached a threshold phosphate bridging beyond which increases in Li-ion mobility are marginal (as has been the case for other amorphous Li-ion conductors like LiPON¹³⁸⁻¹⁴⁰ and lithium silicates^{141,142}).

6.2. The Crystalline Route to Fast Ion-Conductors

Nanocomposite Electrode:

This work has demonstrated that an ionic conductivity of 9.3×10^{-7} S/cm can be achieved by the NASICON phase in a low crystallinity state. The ionic conductivity of the NASICON phase can be improved by optimizing annealing conditions in both the thermal and PEALD LTP processes. However, care should be taken to balance the degree of crystallinity with grain boundary

contact by the amorphous matrix. Annealing thin films into higher density phases can present challenges of film porosity and void formation if the film is too crystalline. In bulk synthesis methods, an amorphous layer is intentionally introduced by including sintering agents to maintain good contact between grains and improve total ionic conductivity.¹⁴³ Future development of the LTP crystalline system should take this into consideration to maximize overall performance as an ionic material.

Further improvements to the ionic conductivity in this materials system will require the development of a better electronic conducting sub-phase to match the ionic conductivity. One can look at other ALD-compatible electronic conductors like TiN or even various metals (e.g, Pt, Ru, Cu) to introduce into the film by supercycling between LTP and the electronic conductor. Unwanted oxidation will be an issue for most metals and must be considered when selecting an electron conductor. Depending on the material of choice, this will require careful development of the annealing conditions such that the desired phases are present in the nanocomposite electrode.

Solid State Electrolyte:

Due to time constraints, a crystalline NASICON electrolyte was not fully developed in this dissertation. There is still much to learn about the crystallization route of the LTP system and how compositional and network structural changes will affect thermal budgets of NASICON grain growth while maintaining phase purity. This can not only be considered for the compositional changes within LTP but also by tuning the aluminum concentration in LATP.

6.3. Solid State Devices for Advanced Iontronics Applications

This work also demonstrated the electrochemical behavior of the LTP/TiO₂ nanocomposite as a proof of concept in a liquid half-cell. A highlight of this material is that it is stable under

different potential windows that can offer selective benefits depending on application demands. For example, the good contact between the TiO₂ and NASICON grains allow for fast kinetics (82.5% capacity retention at 20 C) that can be used in high power delivery applications. On the other hand, the amorphous matrix and anatase grains enable high energy density (1520 mAh/g stable capacity) despite the loss of the NASICON phase at low potentials.

In addition to the individual materials optimization described in **Sections 6.1-6.2**, this material system should be studied in solid state devices (i.e., microbatteries, pseudocapacitors). This can be done by using both the nanocomposite electrode *and* the solid-state electrolyte developed in this work in a single material phosphate-based system with LiFePO₄ as the cathode material.⁶¹ Experiments similar to those performed in this work can be done to understand the stability of these films in an all-solid-state system and understand the nature of the interfaces in such a device. Additionally, parameters relevant to power electronics should be understood such as the cutoff frequency of the LTP electrolyte, and time to charge behavior of a capacitor stack. Lastly, for application in microelectronics, conformal ALD processes of the discussed materials should be developed to deposit uniform films onto 3D structures for increased power and energy densities.

6.4. Publication and Communication Outcomes During Doctoral Degree

6.4.1. Publications

- (1) **Fontecha, D. R.;** Rubloff, G. W.; Gregorczyk, K. E. Atomic Layer Deposition of NASICON-type LTP Nanocomposite Electrode with Electrochemical Phase Control. *In preparation.*
- (2) **Fontecha, D. R.;** Kozen, A. C.; Stewart, D. M.; Hall, A. T.; Cumings, J.; Rubloff, G. W.; Gregorczyk, K. E. Nanoscale Mixed Ion-Electron-Conducting NASICON-Type Thin Films: Lithium Titanium Phosphate via Atomic Layer Deposition. *ACS Appl. Mater.*

Interfaces **2025**, 17 (17), 25358-25369. <https://doi.org/10.1021/acsami.5c02201>.

- a. **Contributions:** Developed the plans for the research with input from Keith Gregorczyk and Gary Rubloff. Developed the ALD process, fabricated the devices, and characterized the films. Wrote the manuscript with input from all authors.
- (3) Wang, Y.; Ko, J.; Lee, M.; Klueter, S.; Kallon, E.; Hoerauf, J.; **Fontecha, D.**; Lee, C.; Rubloff, G. W.; Lee, S. B.; Kozen, A. C. Suppression of Electrochemical and Chemical Degradation of Li₁₀GeP₂S₁₂ by an Elastomeric Artificial Solid Electrolyte Interphase. *ACS Appl. Energy Mater.* **2023**, 6 (15), 8266-8276. <https://doi.org/10.1021/acsam.3c01397>.
 - a. **Contributions:** Performed XPS and XPS analysis on samples.
 - (4) **Fontecha, D.**; Nuwayhid, R. B.; Kozen, A. C.; Stewart, D. M.; Rubloff, G. W.; Gregorczyk, K. E. Low Temperature Plasma-Enhanced Atomic Layer Deposition of Sodium Phosphorus Oxynitride with Tunable Nitrogen Content. *J. Vac. Sci. Technol. A* **2022**, 40 (3), 032403. <https://doi.org/10.1116/6.0001752>.
 - a. **Contributions:** Developed the plans for the research with input from Ramsey Blake Nuwayhid, Gary Rubloff, Alexander Kozen, and Keith Gregorczyk. Co-developed the ALD process with Ramsey Blake Nuwayhid. Performed XPS, SEM characterization, and electrochemical measurements. Wrote the manuscript with input from all authors.
 - (5) Nuwayhid, R. B.; **Fontecha, D.**; Kozen, A. C.; Jarry, A.; Lee, S. B.; Rubloff, G. W.; Gregorczyk, K. E. Nanoscale Li, Na, and K Ion-Conducting Polyphosphazenes by Atomic Layer Deposition. *Dalt. Trans.* **2022**, 51 (5), 2068–2082. <https://doi.org/10.1039/d1dt03736f>.
 - a. **Contributions:** Co-wrote the manuscript with Ramsey Blake Nuwayhid with input from Keith Gregorczyk.

6.4.2. Conference Proceedings

- (1) “Tuning the Composition and Structure of Thin Film Ionic Conductors with Atomic Layer Deposition”. *American Vacuum Society (AVS)*. **2024**.
- (2) “Atomic Layer Deposition (ALD) of Fast Li-ion Conducting Thin Films”. *American Vacuum Society (AVS) Regional Conference at NIST*. **2024**.
- (3) “Towards NASICON-type LATP: Atomic Layer Deposition of Ternary Metal Phosphates”. *Atomic Layer Deposition (ALD)*. **2023**.
- (4) “Atomic Layer Deposition of Sodium Phosphorous Oxynitride”. *Materials Research Society (MRS) Spring*. **2022**.

Bibliography

- (1) Puurunen, R. L. A Short History of Atomic Layer Deposition: Tuomo Suntola's Atomic Layer Epitaxy. *Chem. Vap. Depos.* **2014**, *20* (10–12), 332–344.
<https://doi.org/10.1002/cvde.201402012>.
- (2) Xie, J.; Zhao, J.; Liu, Y.; Wang, H.; Liu, C.; Wu, T.; Hsu, P. C.; Lin, D.; Jin, Y.; Cui, Y. Engineering the Surface of LiCoO₂ Electrodes Using Atomic Layer Deposition for Stable High-Voltage Lithium Ion Batteries. *Nano Res.* **2017**, *10* (11), 3754–3764.
<https://doi.org/10.1007/s12274-017-1588-1>.
- (3) Hyung, J.; Gwon, S.; Han, D.; Jong, H.; Yongmin, C.; Shicheng, K.; Jihwan, X. Atomic Layer Deposition for Surface Engineering of Solid Oxide Fuel Cell Electrodes. *Int. J. Precis. Eng. Manuf. Technol.* **2019**, *6* (3), 629–646. <https://doi.org/10.1007/s40684-019-00092-7>.
- (4) Bakke, J. R.; Pickrahn, K. L.; Brennan, T. P.; Bent, S. F. Nanoscale Nanoengineering and Interfacial Engineering of Photovoltaics by Atomic Layer. **2011**.
<https://doi.org/10.1039/c1nr10349k>.
- (5) Hwang, C. S.; Yoo, C. Y. *Atomic Layer Deposition for Semiconductors*; 2014.
- (6) Chen, R.; Li, Y.; Cai, J.; Cao, K.; Lee, H. Atomic Level Deposition to Extend Moore's Law and beyond. **2020**.
- (7) George, S. M.; Ferguson, J. D.; Weimer, A. W. Atomic Layer Controlled Deposition on Particle Surfaces (US Patent 6,613,383 B1), 2003.
- (8) George, S. M.; Ferguson, J. D.; Weimer, A. W.; Wank, J. R. Insulating and Functionalizing Fine Metal-Containing Particles with Conformal Ultra-Thin Films. (U.S. Patent 6,713,177). 2004.

- (9) Nano, F. High Throughput Method for Manufacturing ALD Coatings (Any Powder) (US Patent No. 9,546,424).
- (10) Li, T.; Xiao, K. Solid-State Iontronic Devices: Mechanisms and Applications. *Adv. Mater. Technol.* **2022**, 7 (12), 1–17. <https://doi.org/10.1002/admt.202200205>.
- (11) Pearse, A.; Schmitt, T.; Sahadeo, E.; Stewart, D. M.; Kozen, A.; Gerasopoulos, K.; Talin, A. A.; Lee, S. B.; Rubloff, G. W.; Gregorczyk, K. E. Three-Dimensional Solid-State Lithium-Ion Batteries Fabricated by Conformal Vapor-Phase Chemistry. *ACS Nano* **2018**, 12 (5), 4286–4294. <https://doi.org/10.1021/acsnano.7b08751>.
- (12) Banerjee, P.; Perez, I.; Henn-lecordier, L.; Lee, S. B.; Rubloff, G. W. Nanotubular Metal – Insulator – Metal Capacitor Arrays for Energy Storage. **2009**, 4 (March), 292–296. <https://doi.org/10.1038/NNANO.2009.37>.
- (13) Fuller, E. J.; Gabaly, F. El; Léonard, F.; Agarwal, S.; Plimpton, S. J.; Jacobs-Gedrim, R. B.; James, C. D.; Marinella, M. J.; Talin, A. A. Li-Ion Synaptic Transistor for Low Power Analog Computing. *Adv. Mater.* **2017**, 29 (4), 1–8. <https://doi.org/10.1002/adma.201604310>.
- (14) Islam, R.; Shi, Y.; de Oliveira Silva, G. V.; Sachdev, M.; Miao, G. X. Volatile and Nonvolatile Programmable Iontronic Memristor with Lithium Imbued TiOx for Neuromorphic Computing Applications. *ACS Nano*. 2024. <https://doi.org/10.1021/acsnano.4c05137>.
- (15) Patel, K. J.; Bhatt, G. G.; Ray, J. R.; Suryavanshi, P.; Panchal, C. J. All-Inorganic Solid-State Electrochromic Devices: A Review. *J. Solid State Electrochem.* **2017**, 21 (2), 337–347. <https://doi.org/10.1007/s10008-016-3408-z>.
- (16) Bu, X.; Xu, H.; Shang, D.; Li, Y.; Lv, H.; Liu, Q. Ion-Gated Transistor: An Enabler for

- Sensing and Computing Integration. *Adv. Intell. Syst.* **2020**, 2 (12), 2000156.
<https://doi.org/10.1002/aisy.202000156>.
- (17) Han, L.; Hsieh, C. Te; Chandra Mallick, B.; Li, J.; Ashraf Gandomi, Y. Recent Progress and Future Prospects of Atomic Layer Deposition to Prepare/Modify Solid-State Electrolytes and Interfaces between Electrodes for next-Generation Lithium Batteries. *Nanoscale Advances*. Royal Society of Chemistry May 21, 2021, pp 2728–2740.
<https://doi.org/10.1039/d0na01072c>.
- (18) Choi, C.; Ashby, D. S.; Butts, D. M.; DeBlock, R. H.; Wei, Q.; Lau, J.; Dunn, B. Achieving High Energy Density and High Power Density with Pseudocapacitive Materials. *Nature Reviews Materials*. Nature Research January 1, 2020, pp 5–19.
<https://doi.org/10.1038/s41578-019-0142-z>.
- (19) Varshneya, A. K.; Mauro, J. C. *Fundamentals of Inorganic Glasses*; 2019.
<https://doi.org/10.1016/C2017-0-04281-7>.
- (20) Wang, Z.; Luo, S. hua; Zhang, X.; Guo, S.; Li, P.; Yan, S. Glass and Glass Ceramic Electrodes and Solid Electrolyte Materials for Lithium Ion Batteries: A Review. *Journal of Non-Crystalline Solids*. Elsevier B.V. November 1, 2023.
<https://doi.org/10.1016/j.jnoncrysol.2023.122581>.
- (21) Shang, C.; Li, X.; Wei, R.; Liu, X.; Xu, S.; Zhang, J. Research Progress of Metal Oxide Glass Anode Materials for Lithium-Ion Batteries: A Review. *J. Non. Cryst. Solids* **2023**, 618 (June), 122547. <https://doi.org/10.1016/j.jnoncrysol.2023.122547>.
- (22) Zhang, Y. Glass Anodes for Lithium Ion Batteries: Insight from the Structural Evolution during Discharging/Charging. *Int. J. Appl. Glas. Sci.* **2020**, 11 (3), 577–589.
<https://doi.org/10.1111/ijag.15079>.

- (23) Yamauchi, H.; Park, G.; Nagakane, T.; Honma, T.; Komatsu, T.; Sakai, T.; Sakamoto, A. Performance of Lithium-Ion Battery with Tin-Phosphate Glass Anode and Its Characteristics. *J. Electrochem. Soc.* **2013**, *160* (10), A1725–A1730. <https://doi.org/10.1149/2.049310jes>.
- (24) Yan, J. Glass-Based Anodes for Lithium-Ion Batteries, 2022.
- (25) Brow, R. K. Review : The Structure of Simple Phosphate Glasses. **2000**, *264*.
- (26) Dutta, B.; Fahmy, N. A.; Pegg, I. L. Effect of Mixed Transition-Metal Ions in Glasses . Part III : The $P_2O_5 - V_2O_5 - MnO$ System. **2006**, *352*, 2100–2108. <https://doi.org/10.1016/j.jnoncrysol.2006.02.043>.
- (27) Martin, S. W. Ionic Conduction in Phosphate Glasses. *J. Am. Ceram. Soc.* **1991**, *74* (8), 1767–1784. <https://doi.org/10.1111/j.1151-2916.1991.tb07788.x>.
- (28) Chatterjee, A.; Majumdar, S.; Ghosh, A. Effect of Network Structure on Dynamics of Lithium Ions in Molybdenum Phosphate Mixed Former Glasses. *Solid State Ionics* **2020**, *347* (January), 115238. <https://doi.org/10.1016/j.ssi.2020.115238>.
- (29) Yu, L. qiang; Zhao, S. X.; Wu, X.; Li, J. W.; Zhao, E. L.; Wei, G. D. Lithium Ion Storage Behaviors of $(100-x)V_2O_5-(x)P_2O_5$ Glass as Novel Anode Materials for Lithium Ion Battery. *J. Alloys Compd.* **2019**, *810*. <https://doi.org/10.1016/j.jallcom.2019.151938>.
- (30) Kercher, A. K.; Ramey, J. O.; Carroll, K. J.; Kiggans, J. O.; Dudney, N. J.; Meisner, R. A.; Boatner, L. A.; Veith, G. M. Mixed Polyanion Glass Cathodes : Iron Phosphate Vanadate Glasses. **2014**, *161* (14), 2210–2215. <https://doi.org/10.1149/2.0881414jes>.
- (31) Nuspl, G.; Takeuchi, T.; Weiß, A.; Kageyama, H.; Yoshizawa, K.; Yamabe, T. Lithium Ion Migration Pathways in $LiTi_2(PO_4)_3$ and Related Materials. *J. Appl. Phys.* **1999**, *86* (10), 5484–5491. <https://doi.org/10.1063/1.371550>.

- (32) Aono, H.; Sugimoto, E.; Sadaoka, Y.; Imanaka, N.; Adachi, G. Ionic Conductivity of Solid Electrolytes Based on $\text{Li}_{1.3}\text{Al}_{0.3}\text{Ti}_{1.7}(\text{PO}_4)_3$. *Russ. J. Appl. Chem.* **1996**, *69* (3), 385–388.
- (33) DeWees, R.; Wang, H. Synthesis and Properties of NaSICON-Type LATP and LAGP Solid Electrolytes. *ChemSusChem* **2019**, *12* (16), 3713–3725.
<https://doi.org/10.1002/cssc.201900725>.
- (34) Kwatek, K.; Ślubowska, W.; Ruiz, C.; Sobrados, I.; Sanz, J.; Garbarczyk, J. E.; Nowiński, J. L. The Mechanism of Enhanced Ionic Conductivity in $\text{Li}_{1.3}\text{Al}_{0.3}\text{Ti}_{1.7}(\text{PO}_4)_3$ – $(0.75\text{Li}_2\text{O}\cdot 0.25\text{B}_2\text{O}_3)$ Composites. *J. Alloys Compd.* **2020**, *838*, 1–13.
<https://doi.org/10.1016/j.jallcom.2020.155623>.
- (35) Kwatek, K.; Ślubowska, W.; Nowiński, J. L.; Krawczyńska, A. T.; Sobrados, I.; Sanz, J. Electrical and Structural Properties of $\text{Li}_{1.3}\text{Al}_{0.3}\text{Ti}_{1.7}(\text{PO}_4)_3$ -Based Ceramics Prepared with the Addition of Li_4SiO_4 . *Materials (Basel)*. **2021**, *14* (19), 1–15.
<https://doi.org/10.3390/ma14195729>.
- (36) Bachman, J. C.; Muy, S.; Grimaud, A.; Chang, H. H.; Pour, N.; Lux, S. F.; Paschos, O.; Maglia, F.; Lupart, S.; Lamp, P.; Giordano, L.; Shao-Horn, Y. Inorganic Solid-State Electrolytes for Lithium Batteries: Mechanisms and Properties Governing Ion Conduction. *Chem. Rev.* **2016**, *116* (1), 140–162.
https://doi.org/10.1021/ACS.CHEMREV.5B00563/SUPPL_FILE/CR5B00563_SI_001.PDF.
- (37) Scarpioni, F.; Khalid, S.; Chukwu, R.; Pianta, N.; LaMantia, F.; Ruffo, R. Electrochemical Impedance Spectroscopy for Electrode Process Evaluation: Lithium Titanium Phosphate in Concentrated Aqueous Electrolyte. *ChemElectroChem* **2023**, *10*, 1–12.

- (38) Zhang, Q.; Schierholz, R.; Dzieciol, K.; Yu, S.; Tempel, H.; Kungl, H.; Eichel, R.-A. Microstructural Details of Spindle-like Lithium Titanium Phosphate Revealed in Three Dimensions. *RSC Adv.* **2021**, *11*, 34605–34612. <https://doi.org/10.1039/d1ra05754e>.
- (39) Delmas, C.; Nadiri, A.; Soubeyroux, J. L. The Nasicon-Type Titanium Phosphates $\text{A}_2\text{Ti}_2(\text{PO}_4)_3$ (A=Li, Na) as Electrode Materials. *Solid State Ionics* **1988**, *28–30*, 419–423. [https://doi.org/10.1016/S0167-2738\(88\)80075-4](https://doi.org/10.1016/S0167-2738(88)80075-4).
- (40) Wessells, C.; Mantia, F. La; Deshazer, H.; Huggins, R. A.; Cui, Y. Synthesis and Electrochemical Performance of a Lithium Titanium Phosphate Anode for Aqueous Lithium-Ion Batteries. *J. Electrochem. Soc.* **2011**, *158* (3), 352–355. <https://doi.org/10.1149/1.3536619>.
- (41) Kee, Y.; Dimov, N.; Minami, K.; Okada, S. Electrochimica Acta Orthorhombic Lithium Titanium Phosphate as an Anode Material for Li-Ion Rechargeable Battery. *Electrochim. Acta* **2015**, *174*, 516–520. <https://doi.org/10.1016/j.electacta.2015.06.032>.
- (42) Yu, S.; Tempel, H.; Schierholz, R.; Aslanbas, Ö.; Gao, X.; Mertens, J.; de Haart, L. G. J.; Kungl, H.; Eichel, R. A. $\text{LiTi}_2(\text{PO}_4)_3/\text{C}$ Anode Material with a Spindle-Like Morphology for Batteries with High Rate Capability and Improved Cycle Life. *ChemElectroChem* **2016**, *3* (7), 1157–1169. <https://doi.org/10.1002/celec.201600125>.
- (43) Wang, G. X.; Bradhurst, D. H.; Dou, S. X.; Liu, H. K. $\text{LiTi}_2(\text{PO}_4)_3$ with NASICON-Type Structure as Lithium-Storage Materials. *J. Power Sources* **2003**, *124* (1), 231–236. [https://doi.org/10.1016/S0378-7753\(03\)00609-8](https://doi.org/10.1016/S0378-7753(03)00609-8).
- (44) Aatiq, A.; Ménétrier, M.; Croguennec, L.; Suard, E.; Delmas, C. On the Structure of $\text{Li}_3\text{Ti}_2(\text{PO}_4)_3$. *J. Mater. Chem.* **2002**, *12* (10), 2971–2978. <https://doi.org/10.1039/b203652p>.

- (45) He, Y.; Zhang, Z.; Feng, G.; Li, H. Two-Dimensional LiTi₂(PO₄)₃ Flakes for Enhanced Lithium Ions Battery Anode. *Heliyon* **2024**, *10* (1), e23396.
<https://doi.org/10.1016/j.heliyon.2023.e23396>.
- (46) Srout, M.; Lasri, K.; Dahbi, M.; Kara, A.; Tetard, L.; Saadoune, I.; Science, M.; Vi, M.; Rachid, L. M.; Guerir, B. Understanding of the Li-Insertion Process in a Phosphate Based Electrode Material for Lithium Ion Batteries. *J. Power Sources* **2019**, *435* (June), 226803.
<https://doi.org/10.1016/j.jpowsour.2019.226803>.
- (47) Sharma, N.; Dalvi, A. Vanadium Substituted Li_{1-x}-NASICON Systems : Tailoring Electronic Conductivity for Electrode Applications. *J. Alloys Compd.* **2021**, *861*, 157954.
<https://doi.org/10.1016/j.jallcom.2020.157954>.
- (48) Plashnitsa, L. S.; Kobayashi, E.; Noguchi, Y.; Okada, S.; Yamaki, J. Performance of NASICON Symmetric Cell with Ionic Liquid Electrolyte. *J. Electrochem. Soc.* **2010**, 536–543. <https://doi.org/10.1149/1.3298903>.
- (49) Yu, S.; Tempel, H.; Schierholz, R.; Aslanbas, Ö.; Gao, X.; Mertens, J.; de Haart, L. G. J.; Kungl, H.; Eichel, R. A. LiTi₂(PO₄)₃/C Anode Material with a Spindle-Like Morphology for Batteries with High Rate Capability and Improved Cycle Life. *ChemElectroChem* **2016**, *3* (7), 1157–1169. <https://doi.org/10.1002/celec.201600125>.
- (50) Patoux, S.; Masquelier, C. Lithium Insertion into Titanium Phosphates, Silicates, and Sulfates. *Chem. Mater.* **2002**, *14*, 5057–5068.
- (51) Leskelä, M.; Ritala, M. Atomic Layer Deposition (ALD): From Precursors to Thin Film Structures. *Thin Solid Films* **2002**, *409* (1), 138–146. [https://doi.org/10.1016/S0040-6090\(02\)00117-7](https://doi.org/10.1016/S0040-6090(02)00117-7).
- (52) George, S. M. Atomic Layer Deposition: An Overview. *Chem. Rev.* **2010**, *110* (1), 111–

131. <https://doi.org/10.1021/cr900056b>.
- (53) Henderick, L.; Dhara, A.; Werbrouck, A.; Dendooven, J.; Detavernier, C. Atomic Layer Deposition of Metal Phosphates. *Appl. Phys. Rev.* **2022**, *9* (1), 011310. <https://doi.org/10.1063/5.0069647>.
- (54) Militzer, C.; Buchsbaum, J.; Dzhagan, V.; Zahn, D. R. T.; Wulff, H.; Helm, C. A.; Goedel, W. A. Atomic Layer Deposition of Titanium Phosphate from Titanium Tetrachloride and Triethyl Phosphate onto Carbon Fibers. *Adv. Mater. Interfaces* **2018**, *5* (16), 1–11. <https://doi.org/10.1002/admi.201800423>.
- (55) Hämäläinen, J.; Holopainen, J.; Munnik, F.; Heikkilä, M.; Ritala, M.; Leskelä, M. Atomic Layer Deposition of Aluminum and Titanium Phosphates. *J. Phys. Chem. C* **2012**, *116* (9), 5920–5925. <https://doi.org/10.1021/jp205222g>.
- (56) Wiedmann, M. K.; Jackson, D. H. K.; Pagan-Torres, Y. J.; Cho, E.; Dumesic, J. A.; Kuech, T. F. Atomic Layer Deposition of Titanium Phosphate on Silica Nanoparticles. *J. Vac. Sci. Technol. A Vacuum, Surfaces, Film.* **2012**, *30* (1). <https://doi.org/10.1116/1.3664097>.
- (57) Getz, M. N.; Hansen, P. A.; Fjellvåg, H.; Nilsen, O. Luminescent Properties of Europium Titanium Phosphate Thin Films Deposited by Atomic Layer Deposition. *RSC Adv.* **2017**, *7* (13), 8051–8059. <https://doi.org/10.1039/c6ra27644j>.
- (58) Dill, P.; Ren, X.; Hintersatz, H.; Franz, M.; Dentel, D.; Tegenkamp, C.; Ebert, S. Atomic Layer Deposition of Titanium Phosphate onto Reinforcing Fibers Using Titanium Tetrachloride, Water, and Tris(Trimethylsilyl) Phosphate as Precursors. *J. Vac. Sci. Technol. A* **2022**, *40* (2), 022403. <https://doi.org/10.1116/6.0001514>.
- (59) Henderick, L.; Hamed, H.; Mattelaer, F.; Minjauw, M.; Nisula, M.; Meersschant, J.;

- Dendooven, J.; Safari, M.; Vereecken, P.; Detavernier, C. Plasma Enhanced Atomic Layer Deposition of a (Nitrogen Doped) Ti Phosphate Coating for Improved Energy Storage in Li-Ion Batteries. *J. Power Sources* **2021**, 497 (February).
<https://doi.org/10.1016/j.jpowsour.2021.229866>.
- (60) Dobbelaere, T.; Mattelaer, F.; Dendooven, J.; Vereecken, P. M.; Detavernier, C. Plasma-Enhanced Atomic Layer Deposition of Iron and Titanium Phosphates as Electrode Materials for 3D-Structured Lithium-Ion Microbatteries. *ECS Trans.* **2016**, 75 (6), 35–44.
<https://doi.org/10.1149/07506.0035ecst>.
- (61) Liu, J.; Banis, M. N.; Sun, Q.; Lushington, A.; Li, R.; Sham, T. K.; Sun, X. Rational Design of Atomic-Layer-Deposited LiFePO₄ as a High-Performance Cathode for Lithium-Ion Batteries. *Adv. Mater.* **2014**, 26 (37), 6472–6477.
<https://doi.org/10.1002/adma.201401805>.
- (62) Fontecha, D.; Nuwayhid, R. B.; Kozen, A. C.; Stewart, D. M.; Rubloff, G. W.; Gregorczyk, K. E. Low Temperature Plasma-Enhanced Atomic Layer Deposition of Sodium Phosphorus Oxynitride with Tunable Nitrogen Content. *J. Vac. Sci. Technol. A* **2022**, 40 (3), 032403. <https://doi.org/10.1116/6.0001752>.
- (63) Hämäläinen, J.; Holopainen, J.; Munnik, F.; Heikkilä, M.; Ritala, M.; Leskelä, M. Atomic Layer Deposition of Aluminum and Titanium Phosphates. *J. Phys. Chem. C* **2012**, 116 (9), 5920–5925. <https://doi.org/10.1021/jp205222g>.
- (64) Kozen, A. C.; Pearse, A. J.; Lin, C. F.; Noked, M.; Rubloff, G. W. Atomic Layer Deposition of the Solid Electrolyte LiPON. *Chem. Mater.* **2015**, 27 (15), 5324–5331.
<https://doi.org/10.1021/acs.chemmater.5b01654>.
- (65) Knohl, S.; Roy, A. K.; Lungwitz, R.; Spange, S.; Mäder, T.; Nestler, D. J.; Wielage, B.;

- Schulze, S.; Hietschold, M.; Wulff, H.; Helm, C. A.; Seidel, F.; Zahn, D. R. T.; Goedel, W. A. Nonaqueous Atomic Layer Deposition of Aluminum Phosphate. *ACS Appl. Mater. Interfaces* **2013**, *5* (13), 6161–6167. <https://doi.org/10.1021/am401092z>.
- (66) Nuwayhid, R. B.; Jarry, A.; Rubloff, G. W.; Gregorczyk, K. E. Atomic Layer Deposition of Sodium Phosphorus Oxynitride: A Conformal Solid-State Sodium-Ion Conductor. *ACS Appl. Mater. Interfaces* **2020**, *12* (19), 21641–21650. <https://doi.org/10.1021/acsami.0c03578>.
- (67) Henderick, L.; Hamed, H.; Hamed, H.; Mattelaer, F.; Minjauw, M.; Meersschaut, J.; Dendooven, J.; Safari, M.; Safari, M.; Safari, M.; Vereecken, P.; Detavernier, C. Atomic Layer Deposition of Nitrogen-Doped Al Phosphate Coatings for Li-Ion Battery Applications. *ACS Appl. Mater. Interfaces* **2020**, *12* (23), 25949–25960. <https://doi.org/10.1021/acsami.0c05585>.
- (68) Shibata, S. Thermal Atomic Layer Deposition of Lithium Phosphorus Oxynitride as a Thin-Film Solid Electrolyte. **2016**. <https://doi.org/10.1149/2.0371613jes>.
- (69) Tsuruoka, T.; Mallik, S.; Tsujita, T.; Inatomi, Y.; Terabe, K. Effects of Plasma Reactants on Atomic Layer Deposition of Lithium Phosphate and Lithium Phosphorus Oxynitride Electrolyte Films. **2024**. <https://doi.org/10.1021/acs.chemmater.4c00960>.
- (70) Werbrouck, A.; Mattelaer, F.; Minjauw, M.; Nisula, M.; Julin, J.; Munnik, F.; Dendooven, J.; Detavernier, C. Reaction Pathways for Atomic Layer Deposition with Lithium Hexamethyl Disilazide, Trimethyl Phosphate, and Oxygen Plasma. *J. Phys. Chem. C* **2020**, *124* (50), 27829–27839. <https://doi.org/10.1021/acs.jpcc.0c09284>.
- (71) Nisula, M.; Shindo, Y.; Koga, H.; Karppinen, M. Atomic Layer Deposition of Lithium Phosphorus Oxynitride. *Chem. Mater.* **2015**, *27* (20), 6987–6993.

<https://doi.org/10.1021/acs.chemmater.5b02199>.

- (72) Dobbelaere, T.; Mattelaer, F.; Roy, A. K.; Vereecken, P.; Detavernier, C. Plasma-Enhanced Atomic Layer Deposition of Titanium Phosphate as an Electrode for Lithium-Ion Batteries. *J. Mater. Chem. A* **2017**, *5* (1), 330–338.
<https://doi.org/10.1039/c6ta04179e>.
- (73) Kuo, C.; Mcleod, A. J.; Lee, P.; Huang, J.; Kashyap, H.; Wang, V.; Yun, S.; Zhang, Z.; Spiegelman, J.; Kanjolia, R.; Moinpour, M.; Kummel, A. C. Low-Resistivity Titanium Nitride Thin Films Fabricated by Atomic Layer Deposition with TiCl₄ and Metal – Organic Precursors in Horizontal Vias. **2023**. <https://doi.org/10.1021/acsaelm.3c00245>.
- (74) Kozen, A. C.; Pearse, A. J.; Lin, C. F.; Noked, M.; Rubloff, G. W. Atomic Layer Deposition of the Solid Electrolyte LiPON. *Chem. Mater.* **2015**, *27* (15), 5324–5331.
<https://doi.org/10.1021/acs.chemmater.5b01654>.
- (75) Pearse, A. J.; Schmitt, T. E.; Fuller, E. J.; El-Gabaly, F.; Lin, C. F.; Gerasopoulos, K.; Kozen, A. C.; Talin, A. A.; Rubloff, G.; Gregorczyk, K. E. Nanoscale Solid State Batteries Enabled by Thermal Atomic Layer Deposition of a Lithium Polyphosphazene Solid State Electrolyte. *Chem. Mater.* **2017**, *29* (8), 3740–3753.
<https://doi.org/10.1021/acs.chemmater.7b00805>.
- (76) Wang, B.; Liu, J.; Sun, Q.; Li, R.; Sham, T.-K.; Sun, X. Atomic Layer Deposition of Lithium Phosphates as Solid-State Electrolytes for All-Solid-State Microbatteries. *Nanotechnology* **2014**, *25* (504007).
- (77) Hornsveld, N.; Kessels, W. M. M.; Creatore, M. Atomic Layer Deposition of Aluminum Phosphate Using AlMe₃, PO(OMe)₃, and O₂ Plasma: Film Growth and Surface Reactions. *J. Phys. Chem. C* **2020**, *124* (9), 5495–5505.

- https://doi.org/10.1021/ACS.JPCC.0C00301/SUPPL_FILE/JP0C00301_SI_001.PDF.
- (78) Holopainen, J.; Munnik, F.; Hatanp, T.; Ritala, M.; Leskel, M. Lithium Phosphate Thin Films Grown by Atomic Layer Deposition " ,. **2012**, *159* (3), 259–263.
<https://doi.org/10.1149/2.052203jes>.
- (79) Werbrouck, A.; Mattelaer, F.; Dhara, A.; Nisula, M.; Minjauw, M.; Munnik, F.; Dendooven, J.; Detavernier, C. Surface Reactions between LiHMDS, TMA and TMP Leading to Deposition of Amorphous Lithium Phosphate. *J. Mater. Chem. A* **2022**.
<https://doi.org/10.1039/D1TA09500E>.
- (80) Mascaraque, N.; Fierro, J. L. G.; Durán, A.; Muñoz, F. An Interpretation for the Increase of Ionic Conductivity by Nitrogen Incorporation in LiPON Oxynitride Glasses. *Solid State Ionics* **2013**, *233*, 73–79. <https://doi.org/10.1016/j.ssi.2012.12.017>.
- (81) Bates, J. B.; Dudney, N. J.; Gruzalski, G. R.; Zuhr, R. A.; Choudhury, A.; Luck, C. F.; Robertson, J. D. *Fabrication and Characterization of Amorphous Lithium Electrolyte Thin Films and Rechargeable Thin-Film Batteries*; 1993.
- (82) Nuwayhid, R. B.; Fontecha, D.; Kozen, A. C.; Jarry, A.; Lee, S. B.; Rubloff, G. W.; Gregorczyk, K. E. Nanoscale Li, Na, and K Ion-Conducting Polyphosphazenes by Atomic Layer Deposition. *Dalt. Trans.* **2022**, *51* (5), 2068–2082.
<https://doi.org/10.1039/d1dt03736f>.
- (83) Nisula, M.; Shindo, Y.; Koga, H.; Karppinen, M. Atomic Layer Deposition of Lithium Phosphorus Oxynitride. *Chem. Mater.* **2015**, *27* (20), 6987–6993.
<https://doi.org/10.1021/acs.chemmater.5b02199>.
- (84) Pearse, A.; Schmitt, T.; Sahadeo, E.; Stewart, D. M.; Kozen, A.; Gerasopoulos, K.; Talin, A. A.; Lee, S. B.; Rubloff, G. W.; Gregorczyk, K. E. Three-Dimensional Solid-State

- Lithium-Ion Batteries Fabricated by Conformal Vapor-Phase Chemistry. *ACS Nano* **2018**, *12* (5), 4286–4294. <https://doi.org/10.1021/acsnano.7b08751>.
- (85) Lacivita, V.; Westover, A. S.; Kercher, A.; Phillip, N. D.; Yang, G.; Veith, G.; Ceder, G.; Dudney, N. J. Resolving the Amorphous Structure of Lithium Phosphorus Oxynitride (Lipon). *J. Am. Chem. Soc.* **2018**, *140* (35), 11029–11038. <https://doi.org/10.1021/jacs.8b05192>.
- (86) Shibata, S. Thermal Atomic Layer Deposition of Lithium Phosphorus Oxynitride as a Thin-Film Solid Electrolyte. *J. Electrochem. Soc.* **2016**, *163* (13), A2555–A2562. <https://doi.org/10.1149/2.0371613jes>.
- (87) Cheng, Q.; Zhao, X.; Yang, G.; Mao, L.; Liao, F.; Chen, L.; He, P.; Pan, D.; Chen, S. Recent Advances of Metal Phosphates-Based Electrodes for High-Performance Metal Ion Batteries. *Energy Storage Materials*. Elsevier B.V. October 1, 2021, pp 842–882. <https://doi.org/10.1016/j.ensm.2021.07.017>.
- (88) Mackus, A. J. M.; Schneider, J. R.; Macisaac, C.; Baker, J. G.; Bent, S. F. Synthesis of Doped, Ternary, and Quaternary Materials by Atomic Layer Deposition: A Review. *Chem. Mater.* **2019**, *31* (4), 1142–1183. <https://doi.org/10.1021/acs.chemmater.8b02878>.
- (89) Xiao, W.; Wang, J.; Fan, L.; Zhang, J.; Li, X. Recent Advances in $\text{Li}_{1+x}\text{Al}_x\text{Ti}_{2-x}(\text{PO}_4)_3$ Solid-State Electrolyte for Safe Lithium Batteries. *Energy Storage Mater.* **2019**, *19* (August 2018), 379–400. <https://doi.org/10.1016/j.ensm.2018.10.012>.
- (90) Liu, Y.; Liu, J.; Sun, Q.; Wang, D.; Adair, K. R.; Liang, J.; Zhang, C.; Zhang, L.; Lu, S.; Huang, H.; Song, X.; Sun, X. Insight into the Microstructure and Ionic Conductivity of Cold Sintered NASICON Solid Electrolyte for Solid-State Batteries. *ACS Appl. Mater. Interfaces* **2019**, *11* (31), 27890–27896. <https://doi.org/10.1021/acsami.9b08132>.

- (91) Chen, H.; Tao, H.; Zhao, X.; Wu, Q. Fabrication and Ionic Conductivity of Amorphous Li-Al-Ti-P-O Thin Film. *J. Non. Cryst. Solids* **2011**, *357* (16–17), 3267–3271.
<https://doi.org/10.1016/j.jnoncrysol.2011.05.023>.
- (92) Siller, V.; Morata, A.; Nunez Eroles, M.; Arenal, P.; Gonzales-Rosillo, J. C.; Lopez del Amo, J. Mi.; Tarancon, A. High Performance LATP Thin Film Electrolytes for All-Solid-State Microbattery Applications. *J. Mater. Chem. A* **2021**, *9* (17760).
- (93) Yang, F.; Brede, J.; Ablat, H.; Abadia, M.; Zhang, L.; Rogero, C.; Elliott, S. D.; Knez, M. Reversible and Irreversible Reactions of Trimethylaluminum with Common Organic Functional Groups as a Model for Molecular Layer Deposition and Vapor Phase Infiltration. **2017**, *1700237*, 1–10. <https://doi.org/10.1002/admi.201700237>.
- (94) Kim, S.; Lee, S. H.; Jo, I. H.; Seo, J.; Yoo, Y. E.; Kim, J. H. Influence of Growth Temperature on Dielectric Strength of - Al₂O₃ Thin Films Prepared via Atomic Layer Deposition at Low Temperature. **2022**, 1–6. <https://doi.org/10.1038/s41598-022-09054-7>.
- (95) Kozen, A. C.; Pearse, A. J.; Lin, C. F.; Schroeder, M. A.; Noked, M.; Lee, S. B.; Rubloff, G. W. Atomic Layer Deposition and in Situ Characterization of Ultraclean Lithium Oxide and Lithium Hydroxide. *J. Phys. Chem. C* **2014**, *118* (48), 27749–27753.
<https://doi.org/10.1021/jp509298r>.
- (96) Aluminum Spectra - LiAlO₂ <https://xpsdatabase.net/aluminum-spectra-lialo2/> (accessed Aug 11, 2025).
- (97) Aluminum Spectra - a-Al₂O₃ <https://xpsdatabase.net/aluminum-spectra-al2o3/> (accessed Aug 11, 2025).
- (98) Appapillai, A. T.; Mansour, A. N.; Cho, J.; Shao-Horn, Y. Microstructure of LiCoO₂ with and without “AlPO₄” Nanoparticle Coating: Combined STEM and XPS Studies.

- Chem. Mater.* **2007**, *19* (23), 5748–5757. <https://doi.org/10.1021/cm0715390>.
- (99) Huggins, R. A. Simple Method to Determine Electronic Conductivity in Mixed A Review and Ionic Components of the Conductors. *300 Ionics* **2002**, *8*, 300–313.
- (100) Ferrari, V. C.; Lee, S. B.; Rubloff, G. W.; Stewart, D. M. Interface Diagnostics Platform for Thin-Film Solid-State Batteries. *Energy Environ. Sci.* **2025**.
<https://doi.org/10.1039/d4ee03915g>.
- (101) Gao, J.; Shi, S.; Xiao, R.; Li, H. Synthesis and Ionic Transport Mechanisms of α -LiAlO₂. **2016**, *286*, 122–134. <https://doi.org/10.1016/j.ssi.2015.12.028>.
- (102) Wohlmuth, D.; Epp, V.; Bottke, P.; Hanzu, I.; Bitschnau, B.; Letofsky-Papst, I.; Kriechbaum, M.; Amenitsch, H.; Hofer, F.; Wilkening, M. Order vs Disorder - Huge Increase in Ionic Conductivity of Nanocrystalline LiAlO₂ Embedded in an Amorphous-like Matrix of Lithium Aluminate. *J. Mater. Chem. A* **2014**, No. 47.
<https://doi.org/10.1039/C4TA02923B>.
- (103) Yagi, E. Electronic Conduction above 4 K of Slightly Reduced Oxygen-Deficient Rutile TiO_{2-x}. **2000**, *54* (11), 7945–7956.
- (104) Pomoni, K.; Sofianou, M. V.; Georgakopoulos, T.; Boukos, N.; Trapalis, C. Electrical Conductivity Studies of Anatase TiO₂ with Dominant Highly Reactive {0 0 1} Facets. *J. Alloys Compd.* **2013**, *548*, 194–200. <https://doi.org/10.1016/j.jallcom.2012.08.136>.
- (105) Aono, H.; Sugimoto, E.; Sadaoka, Y.; Imanaka, N.; Adachi, G. Ionic Conductivity and Sinterability of the Lithium Titanium Phosphate System. *Solid State Ionics* **1990**, *41* (2), 38–42.
- (106) Gamoke, B.; Neff, D.; Simons, J. Nature of PO Bonds in Phosphates. **2009**, 5677–5684.
- (107) Dodd, D. Titanium-Oxygen Bond Length -Bond Valence Relationship Click Here to Let

Us Know How This Document Benefits You . **2013**, 67.

- (108) Zhang, Z.; Ren, J.; Hu, L. Fast Ionic Conducting Glasses in the System $20\text{LiCl}-40\text{Li}_2\text{O}-(80-x)\text{PO}_5/2-x\text{MoO}_3$: The Structural Dependence of Ion Conductivity Studied by Solid-State Nuclear Magnetic Resonance Spectroscopy. *J. Phys. Chem. C* **2020**, 124 (12), 6528–6535. <https://doi.org/10.1021/acs.jpcc.0c00171>.
- (109) Jamnik, J.; Maier, J. Treatment of the Impedance of Mixed Conductors Equivalent Circuit Model and Explicit Approximate Solutions. **1999**, 146 (11), 4183–4188.
- (110) Balachandran, U.; Erer, N. G. Raman Spectra of Titanium Dioxide. *J. Solid State Chem.* **1982**, 42 (3), 276–282. [https://doi.org/10.1016/0022-4596\(82\)90006-8](https://doi.org/10.1016/0022-4596(82)90006-8).
- (111) Tompsett, G. A.; Bowmaker, G. A.; Cooney, R. P.; Metson, J. B.; Rodgers, K. A.; Seakins, J. M. The Raman Spectrum of Brookite, TiO_2 (Pbc₂, Z = 8). *J. Raman Spectrosc.* **1995**, 26 (1), 57–62. <https://doi.org/10.1002/jrs.1250260110>.
- (112) Pérez-Estébanez, M.; Isasi-Marín, J.; Díaz-Guerra, C.; Rivera-Calzada, A.; León, C.; Santamaría, J. Influence of Chromium Content on the Optical and Electrical Properties of $\text{Li}_{1+x}\text{Cr}_x\text{Ti}_2-x(\text{PO}_4)_3$. *Solid State Ionics* **2013**, 241, 36–45. <https://doi.org/10.1016/j.ssi.2013.04.001>.
- (113) Popović, L.; Manoun, B.; De Waal, D.; Nieuwoudt, M. K.; Comins, J. D. Raman Spectroscopic Study of Phase Transitions in Li_3PO_4 . *J. Raman Spectrosc.* **2003**, 34 (1), 77–83. <https://doi.org/10.1002/jrs.954>.
- (114) Petersen, H.; Stegmann, N.; Fischer, M.; Zibrowius, B.; Radev, I.; Philippi, W.; Schmidt, W.; Weidenthaler, C. Crystal Structures of Two Titanium Phosphate-Based Proton Conductors: Ab Initio Structure Solution and Materials Properties. *Inorg. Chem.* **2022**, 61 (5), 2379–2390. <https://doi.org/10.1021/acs.inorgchem.1c02613>.

- (115) Laskova, B.; Frank, O.; Zikalova, M.; Bousa, M.; Dracinsky, M.; Kavan, L. Lithium Insertion into Titanium Dioxide (Anatase): A Raman Study with $^{16}\text{O}/^{18}\text{O}$ and $^6\text{Li}/^7\text{Li}$ Isotope Labeling. *Chem. Mater.* **2013**, *25* (18), 3710–3717.
<https://doi.org/10.1021/cm402056j>.
- (116) Bamberger, C. E.; Macdougall, C. S.; Begun, G. M.; Hatmaker, T. L. Synthesis of Solid Phosphate Compounds of Ti (II) and Ti (IV). **1991**, *41*, 837–841.
- (117) Bamberger, C. E.; Begun, G. M.; Cavin, O. B. Synthesis and Characterization of Sodium-Titanium Phosphates, $\text{Na}_4(\text{TiO})(\text{PO}_4)_2$, $\text{Na}(\text{TiO})\text{PO}_4$, and $\text{NaTi}_2(\text{PO}_4)_3$. *J. Solid State Chem.* **1988**, *73* (2), 317–324. [https://doi.org/10.1016/0022-4596\(88\)90115-6](https://doi.org/10.1016/0022-4596(88)90115-6).
- (118) Schiffmann, N.; Bucharsky, E. C.; Schell, K. G.; Fritsch, C. A.; Knapp, M.; Hoffmann, M. J. Upscaling of LATP Synthesis: Stoichiometric Screening of Phase Purity and Microstructure to Ionic Conductivity Maps. *Ionics (Kiel)*. **2021**, *27* (5), 2017–2025.
<https://doi.org/10.1007/s11581-021-03961-x>.
- (119) Wu, X. M.; Chen, S.; Mai, F. R.; Zhao, J. H.; He, Z. Q. Influence of the Annealing Technique on the Properties of Li Ion-Conductive $\text{Li}_{1.3}\text{Al}_{0.3}\text{Ti}_{1.7}(\text{PO}_4)_3$ Films. *Ionics (Kiel)*. **2013**, *19* (4), 589–593. <https://doi.org/10.1007/s11581-012-0788-7>.
- (120) Aarik, J.; Aidla, A.; Uustare, T.; Ritala, M.; Leskela, M. *Titanium Isopropoxide as a Precursor for Atomic Layer Deposition: Characterization of Titanium Dioxide Growth Process*; 2000; Vol. 161.
- (121) Grey, L. H.; Nie, H. Y.; Biesinger, M. C. Defining the Nature of Adventitious Carbon and Improving Its Merit as a Charge Correction Reference for XPS. *Appl. Surf. Sci.* **2024**, *653* (December 2023), 159319. <https://doi.org/10.1016/j.apsusc.2024.159319>.
- (122) Zhao, Y.; Chen, P.; Zhang, B.; Su, D. S.; Zhang, S.; Tian, L.; Lu, J.; Li, Z.; Cao, X.;

- Wang, B.; Wei, M.; Evans, D. G.; Duan, X. Highly Dispersed TiO₆ Units in a Layered Double Hydroxide for Water Splitting. *Chem. - A Eur. J.* **2012**, *18* (38), 11949–11958. <https://doi.org/10.1002/chem.201201065>.
- (123) Morimoto, H.; Ito, D.; Ogata, Y.; Suzuki, T.; Sakamaki, K.; Tsuji, T.; Hirukawa, M.; Matsumoto, A.; Tobishima, S. I. Charge/Discharge Behavior of Triclinic LiTiPO₄ Anode Materials for Lithium Secondary Batteries. *Electrochemistry* **2016**, *84* (11), 878–881. <https://doi.org/10.5796/electrochemistry.84.878>.
- (124) Hupfer, T.; Bucharsky, E. C.; Schell, K. G.; Hoffmann, M. J. Influence of the Secondary Phase LiTiOPO₄ on the Properties of Li_{1-x}Al_xTi_{2-x}(PO₄)₃ (x = 0; 0.3). *Solid State Ionics* **2017**, *302*, 49–53. <https://doi.org/10.1016/j.ssi.2016.10.008>.
- (125) Chen, J.; Palliotto, A.; Yun, S.; Christensen, D. V.; Esposito, V.; Pryds, N. Post-Lithiation: A Way to Control the Ionic Conductivity of Solid-State Thin Film Electrolyte. *Mater. Adv.* **2023**, *4* (24), 6638–6644. <https://doi.org/10.1039/d3ma00894k>.
- (126) Forsyth, M.; Wong, S.; Nairn, K. M.; Best, A. S.; Newman, P. J.; Macfarlane, D. R. NMR Studies of Modified Nasicon-like, Lithium Conducting Solid. **1999**, *124*, 213–219.
- (127) Huang, S. Y.; Kavan, L.; Exnar, I.; Gratzel, M. Rocking Chair Lithium Battery Based on Nanocrystalline TiO₂ (Anatase). *J. Electrochem. Soc.* **1995**, *142* (9), 142–144.
- (128) Wagemaker, M.; Van de Krol, R.; Kentgens, A. P. M.; Van Well, A. A.; Mulder, F. M. Two Phase Morphology Limits Lithium Diffusion in TiO₂ (Anatase): A ⁷Li MAS NMR Study. *J. Am. Chem. Soc.* **2001**, *123* (46), 11454–11461. <https://doi.org/10.1021/ja0161148>.
- (129) Wang, C.; Xu, B. Bin; Zhang, X.; Sun, W.; Chen, J.; Pan, H.; Yan, M.; Jiang, Y. Ion Hopping : Design Principles for Strategies to Improve Ionic Conductivity for Inorganic

- Solid Electrolytes. **2022**, 2107064, 1–17. <https://doi.org/10.1002/sml.202107064>.
- (130) Wang, B.; Liu, J.; Sun, Q.; Xiao, B.; Li, R.; Sham, T. Titanium Dioxide / Lithium Phosphate Nanocomposite Derived from Atomic Layer Deposition as a High-Performance Anode for Lithium Ion Batteries. **2016**. <https://doi.org/10.1002/admi.201600369>.
- (131) Hu, B. Y.; Kienle, L.; Guo, Y.; Maier, J. High Lithium Electroactivity of Nanometer-Sized Rutile TiO₂. **2006**, 1421–1426. <https://doi.org/10.1002/adma.200502723>.
- (132) Attia, A.; Wang, Q.; Huang, X.; Yang, Y. Titanium Phosphates as Positive Electrode in Lithium-Ion Batteries: Composition, Phase Purity and Electrochemical Performance. *J. Solid State Electrochem.* **2012**, 16 (4), 1461–1471. <https://doi.org/10.1007/s10008-011-1543-0>.
- (133) Roh, H. K.; Kim, H. K.; Roh, K. C.; Kim, K. B. LiTi₂(PO₄)₃/Reduced Graphene Oxide Nanocomposite with Enhanced Electrochemical Performance for Lithium-Ion Batteries. *RSC Adv.* **2014**, 4 (60), 31672–31677. <https://doi.org/10.1039/c4ra04943h>.
- (134) Luo, J. Y.; Xia, Y. Y. Aqueous Lithium-Ion Battery LiTi₂(PO₄)₃/LiMn₂O₄ with High Power and Energy Densities as Well as Superior Cycling Stability. *Adv. Funct. Mater.* **2007**, 17 (18), 3877–3884. <https://doi.org/10.1002/adfm.200700638>.
- (135) Santos, D. A.; Rezaei, S.; Zhang, D.; Luo, Y.; Lin, B.; Balakrishna, A. R.; Xu, B.; Banerjee, S. Chemistry – Mechanics – Geometry Coupling in Positive Electrode Materials : A Scale-Bridging Perspective for Mitigating Degradation in Lithium- Ion Batteries through Materials Design. **2023**, 458–484. <https://doi.org/10.1039/d2sc04157j>.
- (136) Verma, P.; Maire, P.; Novák, P. Review of the Features and Analyses of the Solid Electrolyte Interphase in Li-Ion Batteries. *Electrochim. Acta* **2010**, 55 (22), 6332–6341.

- <https://doi.org/10.1016/j.electacta.2010.05.072>.
- (137) Huggins, R. A. *Advanced Batteries*; Springer Science and Business Media B.V., 2009.
- (138) Famprakis, T.; Galipaud, J.; Clemens, O.; Pecquenard, B.; Le Cras, F. Composition Dependence of Ionic Conductivity in LiSiPO(N) Thin-Film Electrolytes for Solid-State Batteries. *ACS Appl. Energy Mater.* **2019**, *2* (7), 4782–4791.
<https://doi.org/10.1021/acsaem.9b00415>.
- (139) Pearse, A. J.; Schmitt, T. E.; Fuller, E. J.; El-Gabaly, F.; Lin, C.-F.; Gerasopoulos, K.; Kozen, A. C.; Talin, A. A.; Rubloff, G.; Gregorczyk, K. E. *Nanoscale Solid State Batteries Enabled By Thermal Atomic Layer Deposition of a Lithium Polyphosphazene Solid State Electrolyte*.
- (140) Zhou, S.; Tian, R.; Wu, A.; Lin, L.; Huang, H. Fast Li⁺ Migration in LiPON Electrolytes Doped by Multi-Valent Fe Ions. *J. Energy Chem.* **2022**, *75*, 349–359.
<https://doi.org/10.1016/j.jechem.2022.08.044>.
- (141) Wang, B.; Liu, J.; Banis, M. N.; Sun, Q.; Zhao, Y.; Li, R.; Sham, T.; Sun, X. Atomic Layer Deposited Lithium Silicates as Solid-State Electrolytes for All-Solid-State Batteries. **2017**. <https://doi.org/10.1021/acsaami.7b07113>.
- (142) Pergn, Y.-C.; Cho, H.; Sun, S.; Membreno, D.; Cirigliano, N.; Bunn, B.; Chang, J. P. Synthesis of Ion Conducting Li_xAl_ySi_zO Thin Films by Atomic Layer Deposition. *J. Mater. Chem. A* **2014**, *2*, 9566.
- (143) Robertson, A. D.; West, A. R.; Ritchie, A. G. Review of Crystalline Lithium-Ion Conductors Suitable for High Temperature Battery Applications. **1997**, *104*, 1–11.

